eman ta zabal zazu

Universidad del País Vasco
Euskal Herriko Unibertsitatea

Superconductivity in the Presence of Spin-Dependent Fields

Mikel Rouco Martín

Supervised by: Dr. F. Sebastián Bergeret
Dr. Ilya V. Tokatly

Materials Physics Center
Centro de Física de Materiales
Materialen Fisika Zentroa

2021

The whole is distinct from the sum of its parts.

Aristotle

Uno más uno son siete.

Fran Perea

List of Publications resulting from this doctoral thesis

- M. Rouco, T. T. Heikkilä, and F. S. Bergeret, Electron refrigeration in hybrid structures with spin-split superconductors, Phys. Rev. B **97**, 014529 (2018).

- M. Rouco, I. V. Tokatly, and F. S. Bergeret, Spectral properties and quantum phase transitions in superconducting junctions with a ferromagnetic link Phys. Rev. B **99**, 094514 (2019).

- M. Rouco, S. Chakraborty, F. Aikebaier, V. N. Golovach, E. Strambini, J. S. Moodera, F. Giazotto, T. T. Heikkilä, and F. S. Bergeret, Charge transport through spin-polarized tunnel junction between two spin-split superconductors Phys. Rev. B **100**, 184501 (2019).

- M. Rouco, F. S. Bergeret, and I. V. Tokatly, Gap inversion in quasi-one-dimensional Andreev crystals Phys. Rev. B **103**, 064505 (2021).

- M. Rouco, F. S. Bergeret, and I. V. Tokatly, Spectral properties of Andreev crystals, Phys. Rev. B **104**, 064506 (2021).

- A. Hijano, S. Ilić, M. Rouco, C. González-Orellana, M. Ilyn, C. Rogero, P. Virtanen, T. T. Heikkilä, S. Khorshidian, M. Spies, N. Ligato, F. Giazotto, E. Strambini, and F. S. Bergeret, Coexistence of superconductivity and spin-splitting fields in superconductor/ferromagnetic insulator bilayers of arbitrary thickness, Phys. Rev. Reseach **3**, 023131 (2021).

- E. Strambini, M. Spies, N. Ligato, S. Ilić, M. Rouco, C. González-Orellana, M. Ilyn, C. Rogero, F. S. Bergeret, J. S. Moodera, P. Virtanen, T. T. Heikkilä, and F. Giazotto, Rectification in a Eu-chalcogenide-based superconducting diode, arXiv:2109.01061 (2021) *(submitted)*.

- M. Rouco, I. V. Tokatly, and F. S. Bergeret, Geometry optimization of a Josephson phase battery, *(in preparation)*.
- Jon Ortuzar, M. Rouco, S. Trivini, J. I. Pascual, and F. S. Bergeret, Yu-Shiba-Rusinov states in 2D superconductors with a non-circular Fermi contour, *(in preparation)*.

Acknowledgements

Este doctorado habría resultado un camino mucho más árido y pedragoso de no ser por todas aquellas personas que me han ayudado a lo largo de estos cuatro años. Con estas palabras, quiero expresarles mi más sincero agradecimiento.

I am especially grateful to my thesis supervisors, Dr. F. Sebastian Bergeret and Dr. Ilya V. Tokatly, for helping me every time I needed. Gracias, Sebas, por haber estado siempre disponible para mantener una conversación, ya sea científica o no, y por haberme orientado en todo momento. And thank you, Ilya, for your willingness and because every time I was stuck, you could always see the solution and guide me through the fog (which sometimes could have been considered *smog* due to my polluted choices of notation, parameters, etc.).

También quiero dar las gracias a todos/as los/as compañeros/as del CFM, del DIPC y de la universidad con los que he tenido largas conversaciones y pasado ratos inolvidables. A Tomáš, por los *pizzapotes* a base de pizza sin queso, las largas discusiones tomando café y por la subida al Gorbea que aún nos queda por hacer (con avituallamiento a base de mosto). A Carlos, la persona más agradable que he conocido nunca. A Jorge y a Cris, por su inmejorable manera de ser y por todos las pachangas que hemos echado juntos. A Unai, Julen, Joseba, Andrea, Antonella, Francesco, Roberto, Antton, José, Martín, Álvaro, Miguel y Alba por todos los buenos ratos que hemos pasado comiendo, tomando café o de pintxopote. Muchas gracias y os deseo lo mejor.

I am also very thankful to all the people I have collaborated with. Thank you, Stefan, Alberto, Vitaly, Tero, Elia, Pauli, Subrata, Jon, Nacho, Max, Carmen, Celia, Maria, Francesco and Moodera, for all the interesting discussions and the great job that we have done together.

También quiero agradecer a todo el grupo humano del CFM por su amabilidad y profesionalidad; desde el personal de administración, que me han facilitado todos los trámites, hasta el de recepción, que me ha hecho sentirme como en casa.

Por último, y por ello lo más importante, muchas gracias a mi familia por haberme apoyado y aconsejado en todas mis decisiones. Incluso en esta última etapa en la que no hemos convivido día a día, siempre habéis estado pendientes de cada paso que he ido dando. Gracias a mis amigos y amigas de toda la vida, Álvaro “El Sevillano” Sáiz, David “el crack, el mejor, el más guapo” Olmo, Héctor “El Doctorsito” Galindo y Ane “Linguee” Alsasua. Gracias de verdad por todos esos momentos de desconexión que tanto me han ayudado. Gracias también a Mari Carmen, Juanjo y Ainhoa por estar siempre disponibles para echar una mano en el día a día.

Pero especialmente, muchísimas gracias a Maitane por hacerme tan feliz. No puedo más que agradecerte que me hayas intentado ayudar en todo lo que has podido y que siempre seas capaz de alegrarme en esos momentos de agobio y estrés. Ia hamar urte daramagu elkarrekin, eta beste hamaika urte *zure eskutik kilometroak egin* ditzadan espero dut!

List of Symbols

Acronyms

N – normal metal
I – insulator
S – superconductor
SS – spin-split superconductor
F – ferromagnetic metal
FI – ferromagnetic insulator
BCS – Bardeen-Cooper-Schrieffer
BdG – Bogoliubov-de Gennes
DOS – density of states
GF – Green's function
SOC – spin-orbit coupling
AC – *Andreev crystal*

Mathematical operations and markers

$\cdot^*$ – complex conjugation
$\cdot^\dagger$ – Hermitian conjugation
$\cdot^c$ – time-reversal conjugation
$\hat{\cdot}$ – 2×2 matrices
$\check{\cdot}$ – 4×4 matrices
$\breve{\cdot}$ – 8×8 matrices
$\circ$ – convolution
$\otimes$ – direct product

Commonly used symbols

$\boldsymbol{r} = (x, y, z)$ – vector of spatial coordinates
$\boldsymbol{p} = (p_x, p_y, p_z)$ – vector of momentum coordinates
t – time

ε – energy
$\mathbf{x} = (t, \boldsymbol{r})$ – space-time quadrivector
$\mathbf{q} = (\omega, \boldsymbol{p})$ – energy-momentum quadrivector
ω_n – Matsubara frequencies
$\delta_{\alpha\beta}$ – Kronecker delta
$\delta(\boldsymbol{r})$ – Dirac delta function
$\psi(\mathbf{x})$ – creation field operator in the Heisenberg picture
$\psi^\dagger(\mathbf{x})$ – annihilation field operator in the Heisenberg picture
$\hat{\tau}_{\{0,1,2,3\}}$ – Pauli matrices spanning Nambu space
$\hat{\sigma}^{\{0,x,y,z\}}$ – Pauli matrices spanning spin space
$\mathcal{H}(\mathbf{x})$ – Hamiltonian
$\nabla = (\partial_x, \partial_y, \partial_z)$ – *nabla* operator
$\hat{\zeta}(\mathbf{x})$ – quasiparticle energy operator in spin space
μ – Fermi energy
$\phi(\boldsymbol{r})$ – electrostatic potential
$A_j(\boldsymbol{r})$ – j-th spatial component of the magnetic vector potential
$\Delta(\boldsymbol{r})$ – self-consistent superconducting order parameter
$\varphi(\boldsymbol{r})$ – superconducting phase
$\breve{G}(\mathbf{x}_1, \mathbf{x}_2)$ – exact Green's functions
$\breve{g}(\boldsymbol{r}, \boldsymbol{p}, \epsilon, t)$ – quasiclassical Green's functions
$\nu(\epsilon)$ – Local density of states (LDOS)
$\rho(\boldsymbol{r})$ – charge density
$s^a(\boldsymbol{r})$ – spin density along the $a = \{x, y, z\}$ quantization axis
S^a – total spin along the $a = \{x, y, z\}$ quantization axis
$q(\boldsymbol{r})$ – energy density
$j_j(\boldsymbol{r})$ – the j component of the charge current density
$\dot{s}_j^a(\boldsymbol{r})$ – the j component of the charge current density polarized along the a quantization axis
$\dot{q}_j(\boldsymbol{r})$ – the j component of the energy current density
σ_n – normal-state Drude conductivity
Γ – Dynes parameter
$\hat{\Gamma}$ – polarization matrix of a spin filter

Contents

Chapter 1

Introduction

Superconductivity, first discovery by Kamerling Onnes in 1911, is a phase of matter characterized by two macroscopic properties. The first one is the complete lack of electric resistance, as discovered by Onnes in 1911 [1], which gives the name to the phase. The second one is the expulsion of external magnetic fields from the bulk of the material, discovered by Meissner and Ochsenfeld in 1933 [2]. The superconducting phase appears in many materials at temperatures and external magnetic fields below certain critical values. Phenomenological theoretical descriptions were proposed by the brothers F. and H. London in 1935 [3] and by Ginzburg and Landau in 1950 [4]. However, it was not until 1957 that a successful microscopic description of the superconducting phenomena was provided by J. Bardeen, L. N. Cooper and J. R. Schrieffer [5], known as the *BCS theory*. Based on a previous work by Cooper [6], they showed that the free electron gas is unstable under arbitrarily weak attractive interaction between the electrons near the Fermi surface. The attractive interaction between electrons was found to be mediated by lattice vibrations (phonons), as suggested by the previously discovered phenomenon known as the *isotope effect* [7, 8], *i.e.*, that the values of the critical temperature and magnetic field of superconductors with different isotopic composition depends as $T_c \propto M^{-1/2}$ and $B_c \propto M^{-1/2}$, respectively, with the mass of the ions forming the lattice[1], M. This attractive interaction favours electrons with opposite momentum and spin to bind forming pairs: the so-called *Cooper pairs*. The Cooper pairs are boson-like particles and below the critical temperature condensate. Such type of pairing is known as *s-wave* or conventional pairing and materials in which this type of pairing domi-

---

[1] Remarkably, that electrons residing in the crystal lattice are capable of attracting each other was already demonstrated by Frölich [9] and Bardeen [10, 11, 12, 13, 14] independently between 1950 and 1951.

nates are known as *conventional superconductors*, whose typical critical temperature and critical magnetic field values are in the range of $T_c \sim 0.1\text{–}10K$ and $B_c \sim 1\text{–}100mT$, respectively [15]. This is the case of several elements, such as Al or Nb. The currently highest observed T_c in conventional superconductors is that of magnesium diboride with about $39K$ [16]. In this thesis, we focus on conventional superconductors, which are well described by the BCS theory.

More than a century has passed since the experimental discovery of superconductivity, and more than half a century since their first successful microscopic description, yet it remains one of the most prolific research topics in condensed matter physics. The areas of research are as diverse as the finding of superconductors with higher and higher critical temperatures, the study of materials with non-conventional superconducting pairing mechanism or the engineering of heterogeneous structures where coexisting superconducting and non-superconducting parts give rise to emergent effects with various applications. The work that we present in this thesis belongs to this latter research area. In particular, we consider different mesoscopic[2] systems that contain superconducting elements (S) in contact with other non-superconducting parts that may present spin-dependent fields, like normal metals (N), insulators (I), ferromagnetic conductors (F), ferromagnetic insulators (FI), or materials with strong spin-orbit coupling (SOC). Along these lines, constant advancement in the fabrication and miniaturization of high quality superconducting heterostructures has positioned superconductors as the basis for various emerging technology devices, such as high precision magnetometers (the so-called Superconducting Quantum Interference Devices, SQUIDs) [17], quantum simulation frameworks [18], the realization of qubits as building blocks for quantum computation [19, 20, 21, 22, 23, 24], or extremely sensitive and robust GHz/THz detectors for astronomy [25, 26, 27, 28].

All along this thesis, we are specially interested in systems where the superconducting and magnetic element coexist, which has attracted a great attention during the past decades [29, 30, 31, 32]. In principle, these two states of matter are antagonistic: whereas in the ferromagnetic state all the electronic spins try to be aligned, in a conventional BCS superconductor the condensate is formed by Cooper pairs with opposite spins. However, when they coexist in hybrid systems consisting of S and F layers, the two states of matter couple through mutual *proximity effects*, *i.e.*, the fact that the superconducting and ferromagnetic cor-

---

[2] From the Ancient Greek (*mésos*, “between” and *skopeîn*, "to look" or "see") it refers to systems of size between the microscopic (or atomic) and the macroscopic scale. In superconducting systems this scale is determined by the superconducting coherence length, ξ_0, which is the length scale of the superconducting condensate and it typically ranges between some hundreds of nanometers and few micrometers.

relations are not necessarily bound to the S and F region, respectively, and penetrate the adjacent conducting material over a characteristic length scale. Such interplay leads to novel phenomena not present in either of the two phases by their own, such as the appearance of a triplet component of the superconducting condensate[29, 30, 33].

An important consequence of the proximity effect is the *Josephson effect* [34] in hybrid strcutures. The ground state of the superconducting condensate is described by a macroscopic wavefunction with a coherent phase, known as the *superconducting phase*, φ. In 1962, B. D. Josephson predicted that in a weak junction between two superconductors with different values of φ a non-dissipative current (*a.k.a.* a *supercurrent*) can flow without any voltage applied. The supercurrent is carried by the phase coherent Cooper pairs from both superconductors, whose macroscopic wavefunctions overlap due to the proximity effect. These weak links are usually called *Josephson junctions*, which can consist of a thin insulating barrier (SIS) or a short section of a normal metal (SNS), among other possibilities. This effect is known as the dc-Josephson effect and it is a direct proof of the macroscopic character of the superconducting ground state. On the other hand, Josephson predicted that when the Josephson junction is voltage biased, the coherence tunneling of Cooper pairs leads to an alternating supercurrent – the ac-Josephson effect. Both effects were experimentally confirmed shortly after their prediction [35, 36].

Up to this point, we have described only the macroscopic properties of superconductors. However, in order to understand the crucial features of superconductivity it is important to explore the electronic spectrum. Conventional superconductors above T_c are usually metallic, *i.e.*, its electronic spectrum is continuous around the Fermi level and, therefore, any small perturbation is capable of exciting an electron of the Fermi sea. When these materials enter the superconducting phase, however, electrons bound forming the Cooper pairs, which in turn form a condensate. Each electron forming a Cooper pair has a bounding energy Δ, which means that one has to provide at least 2Δ of energy to the system to break a Cooper pair, creating two excited quasiparticles. In other words, a gap of size 2Δ opens in the quasiparticle spectrum, centered around the Fermi surface. The *pairing potential*, Δ, is known as the *superconducting order parameter*. In Fig. 1.1a, we show the typical density of states (DOS) of a BCS superconductor, ν, in terms of the quasiparticle's energy, ϵ, around the Fermi level. The value of the DOS is normalized with its normal-state Fermi-energy value, $\nu(0)$.

An interesting example of proximity takes place in bilayers between superconductors and ferromagnetic materials. In these structures, the interaction of the condensate with the exchange field of the magnetic layer can be described as an effective Zeeman field that leads to finite magnetization and a drastic change of the DOS. Assuming that the superconducting film is thinner than the superconducting coherence length, ξ_0, this magnetic proximity effect may cause an almost homogeneous spin splitting of the DOS, as the one shown in Fig. 1.1b. When the magnetic layer is a metallic ferromagnet (F), it is difficult to achieve such a homogeneous spin splitting because the Cooper pair correlations from S rapidly decay into F, which also leads to a strong pair-breaking mechanism and suppression of the superconducting state.

This suppression can be avoided by using ferromagnetic insulators (FI) instead. The band gap of the FI prevent the penetration of the superconducting condensate and cause electrons to be reflected in the S/FI interface. Because the FI is magnetic, this reflection is spin-dependent and leads to the creation of an effective exchange field in the superconductor [37, 32]. If the effective exchange field is not stronger than Δ, the superconducting phase survives and a spin-split DOS (like the one shown in Fig. 1.1b) can be observed. Such spin splitting will be of central importance in this thesis. Superconductivity in S/FI bilayers with a clear spin-split DOS has been observed on Al films in contact with europium chalcogenides, such as EuO, EuS and EuSe [38, 39, 40]. So far, this turned out to be the best material combination due to the weak spin-orbit coupling of Al that prevents the smearing of the peaks in the DOS, and the optimal interface exchange interaction between the conduction electrons in the Al and the Eu localized magnetic moments. Similar spin splitting effect was observed already in the 70s in experiments where strong in-plane magnetic fields were applied to thin superconducting films [41, 42], because when the magnetic field is applied along the plane of the S film, the orbital diamagnetic effect is weak [43] and the field mainly induces a paramagnetic response. At that time, the spin-split DOS was used to determine the spin polarization of ferromagnets in S/F structures [44, 45, 46, 40]. Only recently it has been realized that spin-split superconductors may find interesting applications in spintronics, thermoelectricity and sensors [31, 32, 47, 48, 49, 50, 51, 52, 53].

In transport experiments, FIs are also used as spin filtering tunnel barriers, due to their highly spin-dependent conductivity. The combination of a spin-split superconducting DOS and the spin filtering breaks the electron-hole symmetry of the spectral current, which makes FI/S structures suitable for several applications, such as efficient thermoelectric elements [48, 54], bolometers [52], thermometers [50], cryogenic RAM memories [53], and different caloritronic devices to access the electronic heat current in nanostructures [55, 56, 49, 57, 58]. Different FI/S strcutures will be studied in chapter 4 of this thesis

Also new phenomena arise when, in addition to the exchange field, the su-

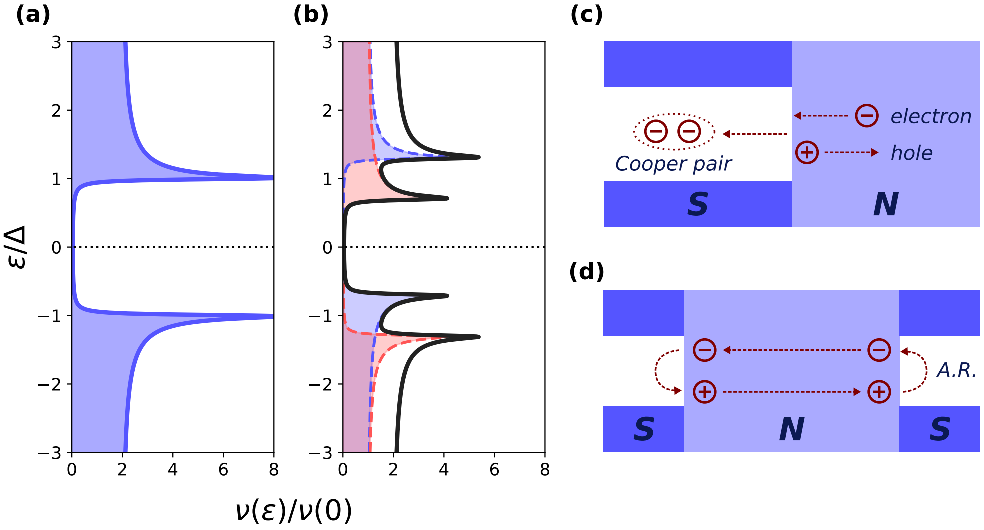

Figure 1.1: Density of states (DOS) of a conventional superconductor $\nu(\epsilon)$ around the Fermi level normalized with its normal-state value at the Fermi level, $\nu(0)$. **(b)** (blue) spin up, (red) spin down and (black) total DOS in a spin-split superconductor. The spin splitting is caused by an effective Zeeman field in the S that stems from the proximity of a magnetic layer. **(c)** Pictorial representation of an *Andreev reflection* process at the interface between a superconductor (S) and a normal metal (N). An incoming electron from the metal with energy within the superconducting gap is back-scattered as a hole and a Cooper pair is formed in the superconductor. **(d)** In a metallic region between two superconductors the Andreev reflection mechanism possibilities the formation of resonant states – the *Andreev bound states.*

perconducting films also show Rashba spin-orbit coupling [59, 60] (SOC). These systems have been proven to be analogous to superconducting films with a non-coplanar texture of exchange field [61, 62, 63, 64], which translates into a precession of the triplet component of the superconducting condensate and a coupling between its singlet and triplet components. The SOC can be either intrinsic to the superconductor[65, 66, 67] or induced at the interface between the S and a heavy-metal doped insulator. The interplay between the SOC and a Zeeman field lead to highly unusual properties, such as the appearance of a inhomogeneous superconducting phase[68, 69], magnetoelectric effects [70, 71, 62] (*e.g.* the spin Hall effect [72, 73], the Edelstein effect [74, 75] or its inverse [76, 77]), and anisotropic magnetic susceptibility [78]. Recently, systems combining superconductivity and spin-dependent fields have attracted a lot of attention because they show topological phases that can host Majorana edge states and non-

Abelian anyons, which make them good candidates for quantum computation [79, 80, 81, 82, 83].

In this thesis we mainly focus on magnetoeletric effects stemming from the SOC. For example, in an infinite SOC/S/FI layered systems, the singlet-triplet coupling generates anomalous charge currents flowing along the plane. When the system is restricted to a finite size, an inhomogeneous superconducting phase, spin accumulation at the edges of the film and/or persistent supercurrent loops flowing along the stripe ends may appear to compensate the anomalous current that would flow in the infinite case [84, 85]. If one now reduces one lateral dimension of the stripe to make it smaller than the superconducting coherence length, ξ_0, the resulting quasi-one-dimensional (quasi-1D) structure can become a useful device. Namely, when the Zeeman field, the symmetry axis of the Rashba SOC and the wire are mutually perpendicular, a non-zero superconducting phase difference, φ_0, may appear between the ends of the wire [63]. Therefore, one expects that plugging this device into a superconducting circuit a supercurrent would flow along the circuit, acting as an analogue to a battery in common electronics – a *Josephson phase battery* [86, 87]. Such a device will be explored in detail in Sec. 4.4 of this thesis

Despite the existence of an energy gap in the excitation spectrum of the superconducting phase, the spectral properties of superconductors differ from those of semiconductors due to the presence of the condensate of Cooper pairs. The interface between a normal metal (N) and a conventional superconductor (S) provides one of the most prominent manifestations of the distinctive effect of the superconducting condensate: the *Andreev reflection* [88] – a scattering process that transfers a charge $2e$ across the interface, where e is the electronic charge. Andreev reflections are the microscopic origin of the proximity effect which underlies almost all the phenomena that we have discussed above. A single conduction electron (hole) from N with energy within the superconducting gap that hits the interface cannot be transferred into S alone. However, it can form a Cooper pair in the superconductor with another electron (hole) of opposite spin and momentum, but the same energy, which leads to the formation of a hole (electron) that gets back-scattered into N, as shown in Fig. 1.1c. In transparent N/S interfaces, the electric transfer mechanism of Andreev reflections adds one extra component to the charge current that would otherwise be given by the quasiparticle current alone. Tunneling junctions, by contrast, prevent Andreev reflections to happen. Note that conventional superconductivity requires electrons with opposite spin orientations for the creation of the Cooper pairs and, therefore, spin-polarization of the media (*i.e.*, an imbalance between the number of particles with opposite spins) is detrimental for the Andreev reflections. Consequently, a fully spin-polarized barrier between the S and N electrodes also inhibits Andreev reflections.

In a ballistic SNS Josephson junction, the Andreev reflection lead to the formation of states bounded to the N region: the so-called *Andreev bound states* [89, 90, 91, 92] (see Fig. 1.1d). The energy of these states depend on the length of the junction and the phase difference between the superconducting electrodes [93, 94]. When one substitutes the N region in the middle with a ferromagnetic one, forming a magnetic Josephson junction (SFS), the spin degeneracy of the Andreev bound states breaks down. These states may cross the Fermi energy at certain strengths of the exchange energy, h. At these crossings the system undergoes a quantum phase transition (QPT), which manifests as a change of the total electronic spin of the system and a change of the ground-state phase difference between the superconductors from 0 to π (or vice-versa) [95, 96, 97, 98, 99, 100, 101, 93, 94]. We study the spectral properties of these SFS junctions in Sec. 3.2.

In a periodic arrangement of these ballistic SFS junctions (forming a chain), the Andreev bound states hybridize and form bands within the superconducting gap. Such bands have been widely studied for the atomic-sized magnetic regions [102, 103, 104, 105, 106, 107, 108, 109, 110], where the width of the F region and its exchange energy is of the order of the Fermi wavelength and energy, respectively. In this limit, the hybridization of the states can lead to topological phases which host Majorana bound states at the ends of the impurity chain. In this thesis we study the analog of such atomic chains in a clean mesoscopic structure, where the size of the F regions is much bigger than the Fermi wavelength and the exchange field is very weak compared to the Fermi energy [111, 112]. We call these structures quasi-1D *Andreev crystals*, which will be studied in Sec.3.3 of this thesis.

The structure of the thesis is the following: Chapter 2 is a brief introduction to the theory of transport in superconducting mesoscopic systems. We summarize basic elements of the BCS theory, the bogoliubov-de Gennes (BdG) formalism and the quasiclassical Green's function formalism, which will be extensively used throughout this thesis. Readers who are not interested in the mathematical details can skip this chapter. The following chapters are self-contained and present original research, thus being the main part of the thesis. Chapter 3 is dedicated to the study of the spectrum in quasi-1D superconducting systems with magnetic impurities. These systems can only change their spin polarization by an integer times the electronic spin after gap closing events. We start by showing a full study of ballistic quasi-1D SFS short junctions in terms of the length of the F region and the exchange field in it, after which we consider infinite and junctions between semi-infinite *Andreev crystals*. Chapter 4 is devoted to the study of different devices based on S/FI bilayers. We start by describing the theoretical model that accurately describes experimental measurements of transport in FI-S-FI-S-FI tunneling junctions, where the FI in the middle is responsible for spin filtering the current and the FIs at the borders cause the spin splitting of the DOS in the adjacent superconductors. After that, we study the heat transport in systems with spin-split superconductors, spin filters and normal metals and discuss their refrigeration capabilities. To close the chapter, we study wires where superconductivity, SOC and ferromagnetism are combined and find suitable geometries in which they can be used as phase batteries. In Chapter 5 we summarize the main results obtained in the previous two chapters and discuss the impact that they may have in future works.

Chapter 2

Quasiclassical Theory of Superconductivity

In this chapter, we introduce the main formalism used in subsequent chapters of the thesis. Readers who are not interested in the mathematical details can skip this chapter. The following chapters of the thesis are self contained and can be followed without having read this one.

This chapter is organized as follows: in Sec. 2.1 we briefly introduce the Bardeen-Cooper-Schrieffer (BCS) theory – the first theory that successfully provided a microscopic description of the superconducting phenomena. Based on the BCS theory, we present two alternative formulations widely used in the study of superconducting heterostructures: the Bogoliubov-de Gennes (BdG) formulation in Sec. 2.2, and the Green's functions (GFs) or Gor'kov formalism in Sec. 2.3. In Sec. 2.4 we present the quasiclassical approximation that yields to the Eilenberger equation (Sec. 2.4.1) and the Usadel equation (Sec. 2.4.2), together with the expressions to compute various observable quantities. Finally, in Sec. 2.5 we show the Matsubara method that we will use in some parts of the thesis to obtain observable's values in thermal equilibrium.

2.1 Bardeen-Cooper-Schrieffer Model

In 1957, Bardeen, Cooper and Schrieffer [5] proposed a model Hamiltonian that successfully explained, for the first time since superconductivity was discovered in 1911, the main properties of the superconducting phase from a microscopic perspective. The Bardeen-Cooper-Schrieffer (BCS) Hamiltonian describes an effective attractive interaction between electrons which form the so-called Cooper pairs [6]. Cooper pairs obey bosonic statistics and, at very low temperatures, they form a Bose-Einstein condensate that provides the superconducting state with its properties.

The BCS theory is based on a phonon mediated interaction that leads to the attraction between electrons [9, 11, 10, 14, 13, 12]. In the original theory it is assumed that such attractive interaction is constant between electrons with energy smaller than a cut-off energy ω_D of the order of the Debye energy. Beyond this energy the attractive interaction vanishes. Because the interaction is typically weak, the characteristic energies of quasiparticles participating in the superconducting phenomena are much smaller that the Fermi energy. It turns out that a point-like constant interaction between the electrons in the form of $V(\boldsymbol{r}_1 - \boldsymbol{r}_2) = \frac{g}{2}\delta(\boldsymbol{r}_1 - \boldsymbol{r}_2)$ is a reasonable approximation, where $\boldsymbol{r}_i$ is the position of the i-th electron and $\delta(\boldsymbol{r})$ stands for the Dirac delta function. An attractive interaction corresponds to $g < 0$ and the limit of small interaction is given by $|g|\nu_F \ll 1$, where ν_F is the density of states at the Fermi level.

With all these assumptions the BCS Hamiltonian in second quantization reads

$$\mathcal{H}_{BCS} = \int d\mathbf{r} \left[\psi^\dagger_\alpha \zeta_{\alpha\beta} \psi_\beta + \frac{g}{2} \psi^\dagger_\beta \psi^\dagger_\alpha \psi_\alpha \psi_\beta \right], \tag{2.1}$$

where the indices α and β label the spin of the particles and $\psi_\alpha(\boldsymbol{r})$ and $\psi^\dagger_\alpha(\boldsymbol{r})$ stand for the annihilation and creation Heisenberg operators, respectively, that fulfill the usual fermionic commutation relations when they are taken at the same instant of time:

$$\left\{ \psi_\alpha(\boldsymbol{r}_1), \psi_\beta(\boldsymbol{r}_2) \right\} = \left\{ \psi^\dagger_\alpha(\boldsymbol{r}_1), \psi^\dagger_\beta(\boldsymbol{r}_2) \right\} = 0, \tag{2.2}$$

$$\left\{ \psi^\dagger_\alpha(\boldsymbol{r}_1), \psi_\beta(\boldsymbol{r}_2) \right\} = \delta_{\alpha\beta}\delta(\boldsymbol{r}_1 - \boldsymbol{r}_2). \tag{2.3}$$

Here $\{\mathcal{A}, \mathcal{B}\} = \mathcal{A}\mathcal{B} + \mathcal{B}\mathcal{A}$ stand for the anti-commutation operation. These commutation relations imply that the attractive interaction term only contributes to the BCS Hamiltonian when $\alpha \neq \beta$. This is an exemplification of Pauli's exclusion principle provided that we considered a point-like interaction.

The first term on the r.h.s. of Eq. (2.1) is the quasiparticle energy operator that in most of this thesis reads,

$$\zeta_{\alpha\beta}(\boldsymbol{r}) = -\frac{1}{2m}\left[\nabla - ieA(\boldsymbol{r})\right]^2 - \mu + V_{\alpha\beta}(\boldsymbol{r}), \tag{2.4}$$

where $V_{\alpha\beta}(\boldsymbol{r})$ is any kind of single-particle potential operator, $A(\boldsymbol{r})$ is the magnetic vector potential and μ labels the Fermi energy. Throughout this chapter we set $\hbar = 1$. Any term in the Hamiltonian (or any other operator) that does not present a pair of spin indices is assumed to be diagonal in the spin-space, *i.e.*, it is multiplied by a $\delta_{\alpha\beta}$ term.

Despite the BCS model proved to be very successful in the understanding of the superconducting phase, its original formulation in the form of Eq. (2.1) is very difficult to solve even in the simplest, homogeneous case. For that reason, in the following sections we present some formalisms typically used to obtain the physical behaviour of inhomogeneous systems where the superconductor does not permeate the whole space or its properties change from one point to another.

2.2 Bogoliubov-de Gennes Equations

It is customary to simplify the two-particle interaction in Eq. (2.1) in a mean field approximation:

$$\mathcal{H}_{BCS}^{\text{eff}} = \int d^3r \left[\psi_\alpha^\dagger \zeta_{\alpha\beta} \psi_\beta + U \psi_\alpha^\dagger \psi_\alpha + \Delta \psi_\uparrow^\dagger \psi_\downarrow^\dagger + \Delta^* \psi_\downarrow \psi_\uparrow \right], \tag{2.5}$$

where,

$$U(\boldsymbol{r}) = g \langle \psi_\uparrow^\dagger \psi_\uparrow \rangle \qquad \text{and} \qquad \Delta(\boldsymbol{r}) = g \langle \psi_\downarrow \psi_\uparrow \rangle , \tag{2.6}$$

are two unknown real and complex effective fields, respectively, calculated from the expectation value of the pairs of operators. The effective field $U(\boldsymbol{r})$ corresponds to the Hartree-Fock potential and, because the properties of conventional superconductors are robust against weak electrostatic potentials [113], one usually does not include this term in the Hamiltonian. In this section we will maintain it in the equations for completeness, but we will drop it in the rest of the thesis. Regarding the complex field $\Delta(\boldsymbol{r})$, we call it the *pairing potential* or the *superconducting order parameter*. In conventional superconductors we may also call it the *superconducting gap*. The value of the effective fields is chosen such that the eigenstates of the effective Hamiltonian correspond to the fundamental state, *i.e.*, that they minimize the free energy. We show their value below in the text (Sec. 2.2.1).

In Eq. (2.5) the U field is accompanied by one creation and one annihilation field operator and, hence, it conserves the number of particles. To simplify the notation, in the following we absorb U into $\zeta_{\alpha\beta}$. By contrast, the complex field Δ creates or annihilates a pair of electrons at once: a Cooper pair. The newly formed pairs form a condensate. We refer to this process as the *condensation* of the Cooper pairs. More precisely, we can rewrite the complex field as $\Delta = |\Delta|e^{i\varphi}$ and identify $|\Delta|$ as the energy needed to break a single Cooper pair and φ as the condensate state's macroscopic phase. Note that the effective Hamiltonian only conserves the number of particles up to modulo two.

Using the effective Hamiltonian, Eq. (2.5), we calculate the time evolution of the creation and annihilation operators[1],

$$\left.\begin{aligned} i\partial_t\psi &= \hat{\zeta}\,\psi - i\Delta\hat{\sigma}^y\psi^* \\ i\partial_t\psi^* &= i\Delta^*\hat{\sigma}^y\psi - \hat{\zeta}^*\psi^* \end{aligned}\right\}, \tag{2.7}$$

where we introduced the spinor operators $\psi \equiv [\psi_\uparrow, \psi_\downarrow]^T$ and $\psi^* \equiv [\psi_\uparrow^\dagger, \psi_\downarrow^\dagger]^T$ and

$$\hat{\sigma}^0 = \begin{pmatrix} 1 & 0 \\ 0 & 1 \end{pmatrix}, \quad \hat{\sigma}^x = \begin{pmatrix} 0 & 1 \\ 1 & 0 \end{pmatrix}, \quad \hat{\sigma}^y = \begin{pmatrix} 0 & -i \\ i & 0 \end{pmatrix}, \quad \hat{\sigma}^z = \begin{pmatrix} 1 & 0 \\ 0 & -1 \end{pmatrix}, \tag{2.8}$$

are the Pauli matrices spanning the spin space. In the preceding equations, and from now on, the *"hat"* symbol, $\hat{\square}$,[2] indicates that the underlying object is a 2×2 matrix.

The quasiparticle energy matrix in spin space that covers most of the scenarios studied in this thesis reads,

$$\hat{\zeta}(\boldsymbol{r}, t) = -\frac{1}{2m}\nabla_j\nabla_j - \mu - h^a(\boldsymbol{r}, t)\hat{\sigma}^a - e\phi(\boldsymbol{r}, t). \tag{2.9}$$

Here the indices $j = \{x, y, z\}$ and $a = \{0, x, y, z\}$ label the spatial and spin coordinates, respectively, and we sum over repeated indices. In Eq. (2.9), μ is the Fermi energy, h^a is an arbitrary attractive exchange field acting on the a component of the spin, and ϕ labels an electrostatic potential. In Sec. 4.4 we will study structures with spin-orbit coupling. In such a case additional terms are required in Eq. (2.9). To simplify the algebra, we do not include those terms here, and at the beginning of Sec. 4.4 we present the equations including SOC [61, 114].

The system of equations in Eq. (2.7) already resembles the Schrödinger equation for a four-element bi-spinor, $[\psi, \psi^*]^T$. For historical reasons, however, instead of ψ and its complex conjugate ψ^*, we consider its time-reversal counterpart, $\bar{\psi} \equiv -i\hat{\sigma}^y\psi^* = [-\psi_\downarrow^\dagger, \psi_\uparrow^\dagger]^T$. For these new set of operators we recast the

---

[1] The time evolution of an operator $\mathcal{O}$ in the Heisenberg representation reads $\partial_t\mathcal{O} = i\left[\mathcal{H}, \mathcal{O}\right]$, where $\mathcal{H}$ is the Hamiltonian of the system.

[2] Here $\square$ acts as a placeholder for the symbol of the matrix.

system of equations in Eq. (2.7) in a compact form:

$$i\hat{\tau}_3\partial_t\Psi = \begin{pmatrix} \hat{\zeta} & \Delta \\ -\Delta^* & \hat{\zeta}^c \end{pmatrix}\Psi \equiv \check{\mathcal{H}}_{BdG}\Psi, \tag{2.10}$$

where $\hat{\zeta}^c \equiv \hat{\sigma}^y\hat{\zeta}^*\hat{\sigma}^y$ is the time-reversal conjugate of the quasiparticles energy and we defined a new four-element bi-spinor $\Psi \equiv [\psi, \bar{\psi}]^T = [\psi_\uparrow, \psi_\downarrow, -\psi_\downarrow^\dagger, \psi_\uparrow^\dagger]^T$. In Eq. (2.10) the 4×4 matrix $\check{\mathcal{H}}_{BdG}$ is known as the *Bogoliubov-de Gennes* (BdG) Hamiltonian. The newly introduced space is the so-called *Nambu* or *electron-hole* space and we label the Pauli matrices spanning Nambu space as $\hat{\tau}_i$ to distinguish them from those spanning spin space, Eq. (2.8). Direct product between Pauli matrices spanning different spaces is implicit and whenever we do not specify any matrix structure of a quantity in spin or Nambu space it is assumed to be proportional to the identity matrix in that space as, for example, $\Delta = \Delta\hat{\sigma}^0$. As in Eq. (2.10), any 4×4 matrix is denoted with an overlying *"check"* symbol, $\check{\square}$.

Equation (2.10) provides the time evolution of the field operators, $\psi_\alpha(\boldsymbol{r})$, in terms of the second-quantization matrix Hamiltonian $\check{\mathcal{H}}_{BdG}$. To obtain the spectral properties of the system, though, we must find the eigenstates of the Hamiltonian. For that purpose we introduce the unitary *Bogoliubov* transformation [115, 116, 117]:

$$\begin{cases} \psi_\uparrow(\boldsymbol{r}) = \sum_n \left(\gamma_{n\uparrow}u_{n\uparrow}(\boldsymbol{r}) - \gamma_{n\downarrow}^\dagger v_{n\downarrow}^*(\boldsymbol{r})\right) \\ \psi_\downarrow(\boldsymbol{r}) = \sum_n \left(\gamma_{n\downarrow}u_{n\downarrow}(\boldsymbol{r}) - \gamma_{n\uparrow}^\dagger v_{n\uparrow}^*(\boldsymbol{r})\right) \end{cases}, \tag{2.11}$$

where $\gamma_{n\alpha}$ and $\gamma_{n\alpha}^\dagger$ are the new quasiparticles annihilation and creation operators, respectively, that still satisfy the fermion commutation relations, Eqs. (2.2) and (2.3). For the new operators to satisfy the commutation rules, it is necessary that $u_{n\alpha}^2 + v_{n\alpha}^2 = 1$. The transformation in Eq. (2.11) must diagonalize the effective Hamiltonian in Eq. (2.5), that is,

$$\mathcal{H}_{BCS}^{\text{eff}} = E_g + \sum_{n,\alpha} \epsilon_n \gamma_{n\alpha}^\dagger \gamma_{n\alpha}. \tag{2.12}$$

Here, E_g is the ground state's energy and ϵ_n is the energy of the excitation n. The commutation of the effective Hamiltonian with the $\gamma_{n\alpha}$ and $\gamma_{n\alpha}^\dagger$ operators provides us conditions to fix the value of the $u_{n\alpha}$ and $v_{n\alpha}$ functions. Combining these relations with the commutation relations between $\mathcal{H}_{BCS}^{\text{eff}}$ and the operators ψ_α we obtain the celebrated *Bogoliubov-de Gennes* equations [118, 119, 120]:

$$\begin{pmatrix} \zeta_{\uparrow\uparrow} & \zeta_{\uparrow\downarrow} & \Delta & 0 \\ \zeta_{\downarrow\uparrow} & \zeta_{\downarrow\downarrow} & 0 & \Delta \\ \Delta^* & 0 & -\zeta_{\downarrow\downarrow}^* & \zeta_{\downarrow\uparrow}^* \\ 0 & \Delta^* & \zeta_{\uparrow\downarrow}^* & -\zeta_{\uparrow\uparrow}^* \end{pmatrix}\begin{pmatrix} u_{n\uparrow} \\ u_{n\downarrow} \\ v_{n\uparrow} \\ v_{n\downarrow} \end{pmatrix} = \epsilon_n \begin{pmatrix} u_{n\uparrow} \\ u_{n\downarrow} \\ v_{n\uparrow} \\ v_{n\downarrow} \end{pmatrix}. \tag{2.13}$$

This equation let us obtain the excitation energies, ϵ_n, and the eigenfunctions, $u_{n\alpha}(\boldsymbol{r})$ and $v_{n\alpha}(\boldsymbol{r})$, of the superconducting system.

2.2.1 Self-consistent potentials: $U(\boldsymbol{r})$ and $\Delta(\boldsymbol{r})$

In the effective Hamiltonian that we present in Eq. (2.5) the mean-field potentials $U(\boldsymbol{r})$ and $\Delta(\boldsymbol{r})$ are some unknown functions to be determined by requiring that the free energy calculated from the states that diagonalize $\mathcal{H}_{BCS}^{\text{eff}}$ is stationary. By definition, the free energy reads $F = \langle \mathcal{H}_{BCS} \rangle - TS$, where T is the temperature, S stands for the entropy and $\langle \mathcal{H}_{BCS} \rangle = \frac{\sum_n e^{-\beta(\epsilon_n - N_n)} \langle n|\mathcal{H}_{BCS}|n\rangle}{\sum_n e^{-\beta(\epsilon_n - N_n)}}$ is the expectation value of the system's energy computed by using the grand-canonical ensemble of statistical mechanics. To calculate the expectation value, $|n\rangle$ represents an eigenstate of the effective Hamiltonian with energy ϵ_n and occupied with N_n particles and $\beta \equiv 1/k_B T$ is the inverse temperature measured in energy units. In thermal equilibrium such a condition is fulfilled by a real potential and a superconducting order parameter that read [118],

$$U(\boldsymbol{r}) = g \langle \psi_\uparrow^\dagger \psi_\uparrow \rangle = g \sum_{n,\alpha} \Big[|u_{n\alpha}(\boldsymbol{r})|^2 f(\epsilon_n) + |v_{n\alpha}(\boldsymbol{r})|^2 \big(1 - f(\epsilon_n)\big) \Big], \tag{2.14}$$

$$\Delta(\boldsymbol{r}) = g \langle \psi_\downarrow \psi_\uparrow \rangle = -g \sum_{n,\alpha} v_{n\alpha}^*(\boldsymbol{r}) u_{n\alpha}(\boldsymbol{r}) \big(1 - 2f(\epsilon_n)\big). \tag{2.15}$$

Here the function $f(\epsilon) = 1/(1 + e^{\beta\epsilon})$ stands for the Fermi-Dirac distribution function. Because Eqs. (2.14) and (2.15) ensure that the potentials U and Δ in the effective Hamiltonian are self-consistent, they are known as the *self-consistent equations* of the potentials.

The potential in Eq. (2.14) corresponds to the standard Hartree-Fock result for a point interaction. In a conventional superconductor, the superconducting properties are robust against weak electrostatic potentials [113]. Moreover, the value of averages like $\langle \psi_\alpha^\dagger \psi_\alpha \rangle$ do not change significantly with temperature because particles from the whole Fermi sphere contribute to them. For these reasons, from now on we treat $U(\boldsymbol{r})$ as a constant potential that can be removed from the effective Hamiltonian by absorbing it into the Fermi energy, μ.

More importantly, the self-consistent expression of the superconducting order parameter, Eq. (2.15), vanishes in absence of any Cooper pair formation mechanism. In this case, only particles near the Fermi energy contribute to the averages like $\langle \psi_\alpha \psi_\beta \rangle$, and therefore $\Delta(\boldsymbol{r})$ depends strongly on temperature.

2.3 Green's Functions formalism. Gor'kov equations.

Bogoliubov-de Gennes equations present a simple method to obtain the physical properties of any superconducting system in a way that would see familiar to anyone who has studied quantum mechanics. However, they become rather complicated if one considers disorder or systems driven out of equilibrium. . Also the calculation of observables from the wave-functions sometimes becomes lengthy and difficult. For these reason we present here a formalism that manage to overcome some of these problems and that it is widely used in the theory of superconductivity: The Green's functions method.

The starting point is the definition of the 4×4 *causal* Green's function (GF) in the Nambu×spin space:

$$\begin{aligned}\check{G}(\mathbf{x}_1,\mathbf{x}_2) &\equiv -i\hat{\tau}_3\,\langle\, T\left[\Psi(\mathbf{x}_1)\otimes\Psi^\dagger(\mathbf{x}_2)\right]\rangle\\ &= -i\hat{\tau}_3\Big[\,\langle\Psi(\mathbf{x}_1)\otimes\Psi^\dagger(\mathbf{x}_2)\rangle\,\theta(t_1-t_2)-\langle\Psi^\dagger(\mathbf{x}_2)\otimes\Psi(\mathbf{x}_1)\rangle\,\theta(t_2-t_1)\Big],\end{aligned} \tag{2.16}$$

where $\mathbf{x}_i$ labels a space-time quadrivector, T is the time-ordering operator, whose effect we explicitly write in the second line of the equation, and $\theta(t)$ is the step function. The symbol ⊗ stands for the outer product between the spinors,

$$\begin{cases}\Psi(\mathbf{x}_1)\otimes\Psi^\dagger(\mathbf{x}_2)=\Psi(\mathbf{x}_1)\Psi^\dagger(\mathbf{x}_2)\\[2ex] \Psi^\dagger(\mathbf{x}_1)\otimes\Psi(\mathbf{x}_2)=\left[\Psi^*(\mathbf{x}_1)\Psi^T(\mathbf{x}_2)\right]^T\end{cases}, \tag{2.17}$$

and $\Psi=[\psi_\uparrow,\psi_\downarrow,-\psi_\downarrow^\dagger,\psi_\uparrow^\dagger]^T$ is the field operator bi-spinor defined below Eq. (2.10). A useful parametrization of the GF defined in Eq. (2.16) is

$$\check{G}=\begin{pmatrix}\hat{G} & \hat{F}\\ -\hat{F}^c & \hat{G}^c\end{pmatrix}, \tag{2.18}$$

where we know $\hat{G}$ and $\hat{F}$ as the *normal* and *anomalous* GFs, respectively. Note that they are 2×2 matrices in spin space that we can write, *e.g.*, as $\hat{G}=G_s+G_t^a\hat{\sigma}^a$, where G_s and G_t^a are the single and triplet components of the normal GF (the same parametrization holds for the anomalous GF, $\hat{F}$). As defined below Eq. (2.10), $\hat{\mathcal{O}}^c\equiv\hat{\sigma}^y\hat{\mathcal{O}}^*\hat{\sigma}^y$ stands for the time-reversal conjugate of the operator $\hat{\mathcal{O}}$.

The causal GFs in Eq. (2.18) satisfy the following equation which can be derived using the expressions for the time evolution of the field operators, Eq. (2.7),

$$\left[i\hat{\tau}_3 \partial_{t_1} - \check{\mathcal{H}}_{BdG}(\mathbf{x}_1) - \check{\Sigma}(\mathbf{x}_1) \right] \check{G}(\mathbf{x}_1, \mathbf{x}_2) = \delta(\mathbf{x}_1 - \mathbf{x}_2). \tag{2.19}$$

Here, $\check{\Sigma}$ is a self-energy that can account for the disorder caused by the presence of impurities, the effect of applied external fields, electron-phonon coupling, *etc.* We will write it explicitly in different cases in subsequent sections. The expression in Eq. (2.19) is equivalent to the Dyson equation generalized to the Nambu×spin space and it is often known as *Gor'kov equations* or as the *equations of motion* of the GF.

A more careful analysis of the different components of the matrix defined in Eq. (2.16) can shed light on the physical meaning of the GFs. In the case of the normal GF, when $t_1 > t_2$ the component $G_{\alpha\beta}(\mathbf{x}_1, \mathbf{x}_2)$ gives the probability of finding at $\mathbf{x}_1$ a particle with spin α given that we included a particle with spin β at the space-time point $\mathbf{x}_2$. Otherwise it provides the probability of finding a hole with spin β at $\mathbf{x}_2$ given that we extracted a particle of spin α at $\mathbf{x}_1$ from the Fermi sea. For anomalous GF, when $t_1 > t_2$ ($t_2 > t_1$) the element $F_{\alpha\beta}(\mathbf{x}_1, \mathbf{x}_2)$ gives the probability of finding a hole (particle) of spin α at $\mathbf{x}_1$ given that a particle of spin β was extracted (included) at $\mathbf{x}_2$. Or in other words, the anomalous GFs, $F_{\alpha\beta}(\mathbf{x}_1, \mathbf{x}_2)$, describe the superconducting condensate.

2.3.1 Keldysh space

The Keldysh Green's functions formalism [121] allows describing many-body systems outside equilibrium. Even in the cases where we study systems in thermal equilibrium, this formalism also provides an unified well-defined framework that still makes it attractive to use. Following the established formalism [121, 122, 123, 119], we define the following three types of functions:

$$\check{G}^R(\mathbf{x}_1, \mathbf{x}_2) \equiv -i\hat{\tau}_3 \left\langle \left\{ \Psi(\mathbf{x}_1) \overset{\otimes}{,} \Psi^\dagger(\mathbf{x}_2) \right\} \right\rangle \theta(t_1 - t_2), \tag{2.20}$$

$$\check{G}^A(\mathbf{x}_1, \mathbf{x}_2) \equiv i\hat{\tau}_3 \left\langle \left\{ \Psi(\mathbf{x}_1) \overset{\otimes}{,} \Psi^\dagger(\mathbf{x}_2) \right\} \right\rangle \theta(t_2 - t_1), \tag{2.21}$$

$$\check{G}^K(\mathbf{x}_1, \mathbf{x}_2) \equiv -i\hat{\tau}_3 \left\langle \left[\Psi(\mathbf{x}_1) \overset{\otimes}{,} \Psi^\dagger(\mathbf{x}_2) \right] \right\rangle . \tag{2.22}$$

where $[\cdot \overset{\otimes}{,} \cdot]$ stands for an outer-product commutator and $\{\cdot \overset{\otimes}{,} \cdot\}$ for an outer-product anti-commutator. The quantities $\check{G}^R$, $\check{G}^A$ and $\check{G}^K$ in the expressions above are

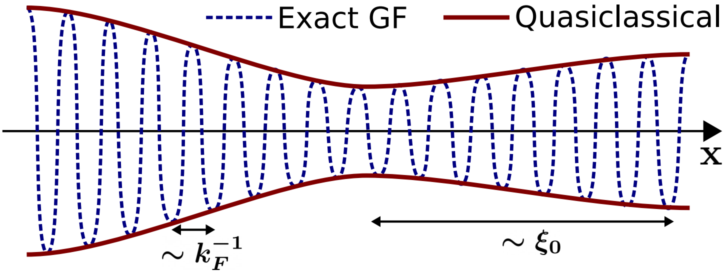

Figure 2.1: Illustration of the quasiclassical approximation. The exact GFs contain fast oscillations on the length of the inverse Fermi momentum, k_F^{-1}, that the quasiclassical approximation obviates to focus on their spatial dependence on a larger scale. In superconducting systems this scale is given by the superconducting coherence length, ξ_0. The ratio $k_F\xi_0$ is typically much larger than the one that we show in the illustration, but we underestimated it for visualization purposes.

known ans the *retarded*, *advanced* and *Keldysh* GFs, respectively, and from direct comparison with Eq. (2.16) it is easy to check that $\check{G} = \frac{1}{2}(\check{G}^K + \check{G}^R + \check{G}^A)$. In the frequency domain $\check{G}^R$ is analytic for $\mathrm{Im}(\omega) > 0$, whereas $\check{G}^A$ is analytic for $\mathrm{Im}(\omega) < 0$. This is a consequence of the identity $\check{G}^A = -\hat{\tau}_3(\check{G}^R)^\dagger\hat{\tau}_3$ that directly follows from the definitions in Eqs. (2.20) and (2.21). The retarded, advanced and Keldysh GFs defined above are collected into an 8×8 matrix in Keldysh×Nambu×spin space [124],

$$\check{G} \equiv \begin{pmatrix} \check{G}^R & \check{G}^K \\ 0 & \check{G}^A \end{pmatrix}, \tag{2.23}$$

that still fulfills Eq. (2.19). From now on we mark 8×8 matrices with the $\check{\square}$ symbol. As we will see later, the retarded and advanced components contain the spectral information (e.g. the density of states) of the system, whereas the Keldysh components contains information on the occupation of the spectrum.

2.4 Quasiclassical approximation

In the previous section, we showed that we can obtain the exact GFs, $\check{G}$, from the Gor'kov equations, Eq. (2.19). The GFs obtained in this way would contain all the information about the system but, in practice, they are extremely difficult to find for all but the simplest physical systems. For that reason we usually rely on what is known as the *quasiclassical approximation* [125, 124, 126].

The quasiclasscial approximation works on systems where the physical parameters involved in the problem varies on length and time scales much larger than the Fermi scale, $\mathbf{q}_F^{-1}$. The phenomenon of superconductivity is a perfect candidate to apply the quasiclassical approximation on because it adds an scale (in addition to the already existing Fermi or atomic scale that characterize every solid) that fulfills the quasiclassical assumption. The superconducting scale is given by a characteristic time, Δ^{-1}, and a characteristic length, $\xi_0 \sim \Delta/v_F$ (known as the *superconducting coherence length*, where v_F is the Fermi velocity), that in conventional superconductors is around three or four orders of magnitude larger than the inverse Fermi energy, μ^{-1}, and the Fermi wavelength, k_F^{-1}, respectively. As a consequence, the exact GFs contain a fast oscillatory $\mathbf{x}_i$ dependence on the atomic scale that describes the physics of the electrons in the solid and a slow $\mathbf{x}_i$ dependence on the superconducting scale that accounts for the condensate. The quasiclassical approximation consists on getting rid off the fast oscillations of $\breve{G}$ to focus on the physics of the superconducting condensate (see Fig. 2.1). Reciprocally, it means that we only care about processes involving quasiparticles close to the Fermi surface. This is a very good approximation to study mesoscopic devices where all the constituents are characterized by energies much smaller than $\mu \sim 1 - 10eV$ and lengths much larger than $k_F^{-1} \sim 0.1 - 1nm$.

2.4.1 The Eilenberger Equation

Within the quasiclassical approximation one transforms the Gor'kov equation into a transport (Boltzmann like) equation, that describes the dynamics of what is known as the *quasiclassical Green's function*. In this section, we make the connection between the *exact* GFs and the *quasiclassical Green's function* that fulfills a transport like equation: the so-called *Eilenberger equation*. This transport-like equation is written in the phase-space that stems from the *Wigner transformation*, which we discuss below. The Eilenberger equation is widely used to study *ballistic* systems of superconductors, *i.e.*, systems with few or none impurities.

To obtain the Eilenberger equation from Gor'kov equations, we start by extracting to the Gor'kov equations [Eq. (2.19)] its conjugate:

$$\begin{aligned}\left[i\hat{\tau}_3\partial_{t_1} - \check{\mathcal{H}}_{BdG}(\mathbf{x}_1) - \check{\Sigma}(\mathbf{x}_1)\right]\check{G}(\mathbf{x}_1,\mathbf{x}_2)&\\ - \check{G}(\mathbf{x}_1,\mathbf{x}_2)\left[i\hat{\tau}_3\partial_{t_2} - \check{\mathcal{H}}_{BdG}(\mathbf{x}_2) - \check{\Sigma}(\mathbf{x}_2)\right] &= 0. \qquad (2.24)\end{aligned}$$

In this way we get rid of the source term on the right-hand side (r.h.s.) of Eq. (2.19). After this, we perform the *Wigner transformation* of Eq. (2.24), which consist on first rewriting the equation that depends on two space-time points, $\mathbf{x}_1$ and $\mathbf{x}_2$, in terms of center-of-mass and relative coordinates, $\mathbf{x} \equiv \frac{\mathbf{x}_1+\mathbf{x}_2}{2}$ and $\delta\mathbf{x} \equiv \mathbf{x}_1 - \mathbf{x}_2$, respectively. The relative coordinate, $\delta\mathbf{x}$, is then Fourier transformed, yielding a description of Eq. (2.24) in terms of $\mathbf{x}$ and the energy-momentum coordinate, $\mathbf{q}$, namely,

$$\frac{i}{2}\Big\{\hat{\tau}_3, \partial_t \breve{G}(\mathbf{x},\mathbf{q})\Big\} + \Big[\varepsilon\hat{\tau}_3, \breve{G}(\mathbf{x},\mathbf{q})\Big] - \Big[\check{\mathcal{H}}_{BdG} \overset{\circ}{,} \breve{G}\Big]_{\mathbf{x},\mathbf{q}} = \Big[\breve{\Sigma} \overset{\circ}{,} \breve{G}\Big]_{\mathbf{x},\mathbf{q}}. \tag{2.25}$$

Here, $\circ$ stands for convolution between the functions[3] and $[A \overset{\circ}{,} B]_{\mathbf{x},\mathbf{q}} = (A \circ B)_{\mathbf{x},\mathbf{q}} - (B \circ A)_{\mathbf{x},\mathbf{q}}$ is a commutation of convolutions due to the Fourier transform of $\delta\mathbf{x}$, where we are using the shorthand notation $(A \circ B)_{\mathbf{x},\mathbf{q}} \equiv A(\mathbf{x},\mathbf{q}) \circ B(\mathbf{x},\mathbf{q})$. In the Fourier transform we used that $\mathbf{q} \cdot \delta\mathbf{x} = -\varepsilon\delta t + \mathbf{k} \cdot \delta \boldsymbol{r}$, where ε and $\mathbf{k}$ are energy and momentum coordinates, respectively. Up to this point everything remains exact and Eq. (2.25) is equivalent to the Gor'kov equations in another representation.

The Wigner transform of the convolution between those functions can be written as [127]:

$$\Big(A \circ B\Big)_{\mathbf{x},\mathbf{q}} \equiv A(\mathbf{x},\mathbf{q}) \circ B(\mathbf{x},\mathbf{q}) = e^{-\frac{i}{2}(\partial^A_{\mathbf{q}}\partial^B_{\mathbf{x}} - \partial^A_{\mathbf{x}}\partial^B_{\mathbf{q}})} A(\mathbf{x},\mathbf{q}) B(\mathbf{x},\mathbf{q}), \tag{2.26}$$

where the exponential is meant to be substituted by its power series. The A (B) superscript on the partial derivative symbol indicates that it only operates on the function A (B). The substitution of the convolutions by the series expansion of the exponential on the r.h.s. of Eq. (2.26) is known as the *gradient expansion* of the Wigner transformed operators.

When all the elements in Eq. (2.25) are slow varying functions of $\mathbf{x}$ compared to the Fermi scale, and involve processes where the energy/momentum transfer is much smaller than their Fermi values, it is a reasonable approximation to maintain only the elements up to first order in $\partial_{\mathbf{x}}$ and $\partial_{\mathbf{q}}$, and drop all the term with higher order derivatives. To this effect we first substitute the convolutions in Eq. (2.25) by its gradient expansion, Eq. (2.26), and then we dismiss any higher order spatial derivatives. For this, we consider the quasiparticle energy matrix in spin space, $\hat{\zeta}$, described in Eq. (2.9). After some algebra, this process results in a transport-like equation that reads:

$$\frac{i}{2}\Big\{\hat{\tau}_3, \partial_t \breve{G}\Big\} + \frac{ik_j}{m}\nabla_j \breve{G} + \Big[\varepsilon\hat{\tau}_3 + e\phi\hat{\tau}_3 + h^a\hat{\sigma}^a\hat{\tau}_3 + \check{\Delta}, \breve{G}\Big] = \check{\boldsymbol{I}}. \tag{2.27}$$

In conventional superconductors $\check{\Delta}(\mathbf{x}) = i\mathrm{Re}[\Delta]\hat{\tau}_2 + i\mathrm{Im}[\Delta]\hat{\tau}_1 = i|\Delta|e^{i\varphi\hat{\tau}_3}\hat{\tau}_2$ labels the singlet superconducting order parameter, where $\varphi(\mathbf{x})$ is the superconducting

---

[3] The convolution happens in the $\mathbf{q}$ coordinate, *i.e.*, `WT`$[AB] = (A \circ B)_{\mathbf{x},\mathbf{q}} = A(\mathbf{x},\mathbf{q}) \circ B(\mathbf{x},\mathbf{q}) = \int \frac{d\mathbf{q}'}{(2\pi)^4} A(\mathbf{x},\mathbf{q}')B(\mathbf{x},\mathbf{q}-\mathbf{q}')$, where `WT`$[\ldots]$ indicates that we Wigner transform the content between the square brakets.

phase. The term at the r.h.s. of Eq. (2.27) is the *collision integral* and it accounts for the impurities in the system, external magnetic fields, or other effects like electron-phonon coupling. Up to first order in the gradient expansion, it reads

$$\check{\mathcal{I}} = \left[\check{\Sigma}, \check{G}\right] - \frac{i}{2}\left\{\partial_{\mathbf{q}}\check{\Sigma}, \partial_{\mathbf{x}}\check{G}\right\} + \frac{i}{2}\left\{\partial_{\mathbf{x}}\check{\Sigma}, \partial_{\mathbf{q}}\check{G}\right\}, \tag{2.28}$$

which in most of the cases can be further simplified by taking only the first term on the r.h.s. of the equation. This simplification accounts for situations where either $\check{\Sigma}$ does not depend on $\mathbf{x}$ and $\mathbf{q}$, or its dependence is very slow. In other words, when all the processes described in $\check{\Sigma}$ involve creation of quasiparticles with energy and momentum much smaller than the Fermi scale, μ and $\mathbf{k}_F$, respectively. In this case the calculation of the *local* GF (*i.e.* the GF for $\delta\boldsymbol{r} = 0$ and $\delta t = 0^-$, where 0^- stands for an arbitrary small negative number) involve an integral over the energy-momentum space that can be simplified as follows:

$$\check{G}(\mathbf{x}, 0^-) = \int \frac{d\varepsilon}{2\pi} \int \frac{d\mathbf{k}}{(2\pi)^3} \check{G}(\mathbf{x}, \mathbf{p}) \approx \oint \frac{dS_F}{4\pi} \nu_0 \int \frac{d\varepsilon}{2\pi} \int d\zeta\, \check{G}(\mathbf{x}, \mathbf{p}). \tag{2.29}$$

Here $\zeta \approx \mathbf{v}_F \cdot (\mathbf{k} - \mathbf{k}_F)$ is the linearized quasiparticle energy around the Fermi energy, $\mathbf{v}_F \equiv \partial_{\mathbf{k}}\zeta\big|_{\mathbf{k}=\mathbf{k}_F}$ is the Fermi velocity, S_F is the solid angle coordinate on the Fermi surface and ν_0 is the DOS at the Fermi level (that can depend on S_F). In Eq. (2.29) the approximations are twofold: first to extract the DOS from the ζ integration assuming that it is constant on the small energy window around the Fermi surface where the GF is finite, and second to extend the lower bound of the integration in ζ from $-\mu$ to $-\infty$. The GF calculated this way accounts for local properties of the system, like the local density of states (LDOS) or density currents.

Motivated by the last form of Eq. (2.29) we define the *quasiclassical GF* as the ζ-integrated GF,

$$\check{g}(\mathbf{x}, \mathbf{n}, \varepsilon) \equiv \frac{i}{\pi} \int d\zeta\, \check{G}(\mathbf{x}, \mathbf{p}), \tag{2.30}$$

that now only depends on the Fermi momentum direction, $\mathbf{n} \equiv \frac{\mathbf{v}_F}{|\mathbf{v}_F|}$, the frequency, ε, and the center-of-mass coordinates. The prefactor is chosen for convenience in future calculations of observable quantities.

The equation of motion for the quasiclassical GF is the celebrated *Eilenberger equation* [128, 125],

$$\frac{i}{2}\left\{\hat{\tau}_3, \partial_t \check{g}\right\} + i v_F n_j \nabla_j \check{g} + \left[\varepsilon\hat{\tau}_3 + e\phi\hat{\tau}_3 + h^a\hat{\sigma}^a\hat{\tau}_3 + \check{\Delta}, \check{g}\right] = \check{\mathfrak{I}}, \tag{2.31}$$

which is directly obtained by integrating Eq. (2.27) along the quasiparticle energy, ζ. The collision integral at the r.h.s. of the equation, is the ζ-integration of Eq. (2.28), $\check{\mathfrak{J}} \equiv \frac{i}{\pi} \int d\zeta \check{\boldsymbol{I}}$.

Because the source term of Gor'kov equations, Eq. (2.19), has been lost in the substraction performed to obtain Eq. (2.25), the Eilenberger equation is arbitrary about the amplitude og $\check{g}$. This ambiguity is removed by imposing Eilenberger's *normalization* condition,

$$\check{g}^2(\mathbf{x}, \mathbf{n}, \varepsilon) = 1. \tag{2.32}$$

It is easy to check that when $\check{g}$ fulfills Eq. (2.31) then $\nabla \check{g}^2 = 0$ and, consequently, if the quasiclassical GF is normalized at one point in the space then $\check{g}^2 = 1$ everywhere in the system. Moreover, given the triangular structure of $\check{g}$ in Keldysh space [Eq. (2.23)], the normalization condition indicates that $(\check{g}^R)^2 = (\check{g}^A)^2$ and allows for writing the Keldysh component of the GF in terms of the retarded and advanced ones as follows,

$$\check{g}^K = \check{g}^R \check{f} - \check{f} \check{g}^A, \tag{2.33}$$

where the matrix $\check{f}(\mathbf{x}, \mathbf{n}, \varepsilon)$ contains information about the occupation of the states in the solid, *i.e.*, it is related to the *distribution function*. In the most general case the 4 × 4 matrix distribution function can be written as [32]

$$\check{f} = f_0 + f_3 \hat{\tau}_3 + f_0^a \hat{\sigma}^a + f_3^a \hat{\sigma}^a \hat{\sigma}_3, \tag{2.34}$$

where $f_{0/3}^a$ are real-valued functions. The different components of $\check{f}$ carry specific information of the nonequilibrium state of the system. For instance, in homogeneous systems at thermal equilibrium without any electric nor spin bias the distribution function reads $\check{f} = \tanh \frac{\epsilon}{2T}$, where T is the temperature in energy units.

2.4.1.1 Calculation of observables

One of the advantage of Green's functions technique in comparison with the BdG formalism is that GFs already contain the integration over the grand-canonical ensemble and, therefore, calculation of observables becomes straight-forward. We are interested in three particular types of observables: densities, currents and the self-consistent potentials. From the definition of the exact GFs in Eqs. (2.20-2.22) and the relation between the local equal-time GF [Eq. (2.29)] and its quasiclassical counterpart, Eq. (2.30), it follows that the charge, spinand energy density of the system read [31, 32],

$$\rho(\mathbf{x}) = -\frac{e}{16}\oint \frac{dS_F}{4\pi}\nu_0 \int d\varepsilon \mathrm{Tr}\left[\hat{\tau}_3 \check{g}^K(\mathbf{x},\mathbf{n},\varepsilon)\right], \tag{2.35}$$

$$s^a(\mathbf{x}) = \frac{1}{16}\oint \frac{dS_F}{4\pi}\nu_0 \int d\varepsilon \mathrm{Tr}\left[\hat{\sigma}^a \check{g}^K(\mathbf{x},\mathbf{n},\varepsilon)\right], \tag{2.36}$$

$$q(\mathbf{x}) = \frac{1}{16}\oint \frac{dS_F}{4\pi}\nu_0 \int d\varepsilon\ \varepsilon\ \mathrm{Tr}\left[\check{g}^K(\mathbf{x},\mathbf{n},\varepsilon)\right], \tag{2.37}$$

respectively, where the trace runs over the Nambu×spin space and direct product between Pauli matrices spanning Nambu and spin spaces is implicit. As usual, the respective identity matrices of Nambu and spin spaces, $\hat{\tau}_0$ and $\hat{\sigma}^0$, are obviated to simplify the notation. One can identify (up to a constant $\frac{\nu_0}{16}$ prefactor) the term inside the ε integral in Eq. (2.35) as the local density of states (LDOS) of quasiparticles at $\mathbf{x}$ with energy ε and velocity v_F along the $\mathbf{n}$ direction.

Similarly, the the self-consistent fields of the effective BCS Hamiltonian [Eqs. (2.14) and (2.15)] read

$$\Delta(\mathbf{x}) = \frac{g}{16i}\oint \frac{dS_F}{4\pi}\nu_0 \int d\varepsilon \mathrm{Tr}\left[\left(\hat{\tau}_2 + i\hat{\tau}_1\right)\check{g}^K(\mathbf{x},\mathbf{n},\varepsilon)\right], \tag{2.38}$$

and $U(\mathbf{x}) = -\frac{g}{e}\rho(\mathbf{x})$ in terms of the Keldysh component of the GF. Equation (2.38) is often called the *self-consistent equation* of Δ and the term with $\hat{\tau}_1$ ($\hat{\tau}_2$) provides the real (imaginary) part of the complex Δ field.

Finally, the expression for the charge, spin and energy currents read

$$\mathbf{j}(\mathbf{x}) = -\frac{e}{16}\oint \frac{dS_F}{4\pi}\nu_0\mathbf{v}_F \int d\varepsilon \mathrm{Tr}\left[\hat{\tau}_3 \check{g}^K(\mathbf{x},\mathbf{n},\varepsilon)\right], \tag{2.39}$$

$$\dot{\mathbf{s}}^a(\mathbf{x}) = \frac{1}{16}\oint \frac{dS_F}{4\pi}\nu_0\mathbf{v}_F \int d\varepsilon \mathrm{Tr}\left[\hat{\sigma}^a \check{g}^K(\mathbf{x},\mathbf{n},\varepsilon)\right], \tag{2.40}$$

$$\dot{\mathbf{q}}(\mathbf{x}) = \frac{1}{16}\oint \frac{dS_F}{4\pi}\nu_0\mathbf{v}_F \int d\varepsilon\ \varepsilon\ \mathrm{Tr}\left[\check{g}^K(\mathbf{x},\mathbf{n},\varepsilon)\right], \tag{2.41}$$

respectively. Comparing Eqs. (2.35) and (2.36) with Eqs. (2.39) and (2.40), respectively, one can see that the currents are calculated by multiplying the densities with the $\mathbf{v}_F$ at each point of the Fermi surface and then integration over S_F. Because in general Fermi surfaces are not spherical the value of $|\mathbf{v}_F|$ may change between different points on the Fermi surface.

2.4.2 The Usadel equation

The Eilenberger equation that we obtained in the previous section, Eq. (2.31), is very successful in calculating the quasiclassical GFs of pristine superconducting systems, where $\breve{\mathfrak{I}} = 0$. It is also useful to calculate the properties of systems with one or few impurities, in which case we could calculate the collision integral explicitly. Note that to do that we must know the exact distribution of the impurities. As soon as the concentration of impurities increases, $\breve{g}(\mathbf{x}, \mathbf{n}, \varepsilon)$ becomes extremely position and propagation direction dependent and obtaining it from Eilenberger equation turns into a cumbersome job.

If we continue increasing the concentration of impurities, the calculation of the quasiclassical GFs simplifies again, though. This is the so-called *dirty* or *diffusive limit*, and it is characterized by the fact that there are so many impurities in the system that from any position the media seems homogeneous (*i.e.*, independent of the propagation direction $\mathbf{n}$). Thus, the quasiclasscial GF can be expanded up to first order in the propagation direction,

$$\breve{g}(\mathbf{x}, \mathbf{n}, \varepsilon) \approx \breve{g}_0(\mathbf{x}, \varepsilon) + n_k \breve{g}_k(\mathbf{x}, \varepsilon), \tag{2.42}$$

where $\breve{g}_0 = \langle \breve{g} \rangle_{\mathbf{n}}$ is the s-wave and $\breve{g}_k$ is the p-wave part of the GF, and $\langle \ldots \rangle_{\mathbf{n}}$ stands for the average over S_F. Because the dirty media is nearly homogeneous, then $\breve{g}_k \ll \breve{g}_0$. Consequently, from the normalization condition the two parts of the GF anticommute, $\breve{g}_0 \breve{g}_k + \breve{g}_k \breve{g}_0 = 0$.

We consider a self-energy term in the collision integral that reads $\breve{\Sigma} = i\big(\breve{\Sigma}_0 + \breve{\Sigma}_{so} + \breve{\Sigma}_{sf} + \breve{\Sigma}_{orb}\big)$, where Σ_0 describe non-magnetic impurities and Σ_{so} and Σ_{sf} account for spin-orbit and spin-flip effects caused by magnetic impurities. The Σ_{orb} term can be used to describe the orbital depairing effect of (Meissner) screening currents induced by an in-plane magnetic field in a thin film, leading to the suppression of superconductivity [129]. Within Born approximation, the self-energies for these elastic processes have the form [32]:

$$\breve{\Sigma}_0 = \frac{\breve{g}_0}{2\tau_0}, \qquad \breve{\Sigma}_{so} = \frac{\hat{\sigma}^a \breve{g}_0 \hat{\sigma}^a}{8\tau_{so}}, \tag{2.43}$$

$$\breve{\Sigma}_{sf} = \frac{\hat{\sigma}^a \hat{\tau}_3 \breve{g}_0 \hat{\tau}_3 \hat{\sigma}^a}{8\tau_{sf}}, \qquad \breve{\Sigma}_{orb} = \frac{\hat{\tau}_3 \breve{g}_0 \hat{\tau}_3}{\tau_{orb}}. \tag{2.44}$$

Here τ_0, τ_{so} and τ_{sf} are the scattering times due to impurities and their magnitude strongly depends on the experimental procedures used to grow the sample. The dirty limit that we discussed qualitatively in previous lines corresponds to the case where τ_0^{-1} is much bigger than any other characteristic energy scale in the system (including Δ and the remaining elastic self-energy terms). The orbital depairing relaxation time, by contrast, can be estimated in thin superconducting films as [130, 131]:

$$\frac{1}{\tau_{orb}} = \left(\frac{\pi d \xi_0 B}{\sqrt{6}\Phi_0}\right)^2 \Delta, \tag{2.45}$$

where d is the width of the superconducting film, B is the applied magnetic field and $\Phi_0 \equiv \frac{\pi}{e}$ is the magnetic flux quantum[4].

We start from the Eilenberger equation in equilibrium,

$$v_F n_j \nabla_j \breve{g} - i\left[\varepsilon\hat{\tau}_3 + e\phi\hat{\tau}_3 + h^a\hat{\sigma}^a\hat{\tau}_3 + \check{\Delta}, \breve{g}\right] = -\left[\breve{\Sigma}_0 + \breve{\Sigma}', \breve{g}\right], \tag{2.46}$$

where $\breve{\Sigma}' = \breve{\Sigma}_{so} + \breve{\Sigma}_{sf} + \breve{\Sigma}_{orb}$. We assume a spherical Fermi surface where v_F does not depend on the propagation direction, $\mathbf{n}$. On the one hand, we calculate the angular average of Eq. (2.46) to obtain

$$\frac{v_F}{3}\nabla_j \breve{g}_j - i\left[\varepsilon\hat{\tau}_3 + e\phi\hat{\tau}_3 + h^a\hat{\sigma}^a\hat{\tau}_3 + \check{\Delta}, \breve{g}_0\right] = -\left[\breve{\Sigma}', \breve{g}_0\right], \tag{2.47}$$

in terms of the s-wave and p-wave parts of the GF, Eq. (2.42). On the other hand, the angular average of Eq. (2.46) multiplied by n_j reads

$$v_F \nabla_j \breve{g}_0 - i\left[\varepsilon\hat{\tau}_3 + e\phi\hat{\tau}_3 + h^a\hat{\sigma}^a\hat{\tau}_3 + \check{\Delta}, \breve{g}_j\right] = -\left[\breve{\Sigma}_0 + \breve{\Sigma}', \breve{g}_j\right]. \tag{2.48}$$

From Eq. (2.48) we can express the anisotropic part of the GF, $\breve{g}_j$, in terms of the isotropic one, $\breve{g}_0$, to find that:

$$\breve{g}_j = -\tau_0 v_F \breve{g}_0 \tilde{\nabla}_j g_0. \tag{2.49}$$

Inserting this result into Eq. (2.47) we obtain the Usadel equation [132] in presence of random localized magnetic impurities,

$$D\nabla_j\left(\breve{g}_0\nabla_j\breve{g}_0\right) + i\left[\varepsilon\hat{\tau}_3 + e\phi\hat{\tau}_3 + h^a\hat{\sigma}^a\hat{\tau}_3 + \check{\Delta} + i\breve{\Sigma}', \breve{g}_0\right] = 0\ , \tag{2.50}$$

where $D \equiv \frac{v_F^2\tau_0}{3}$ is the *diffusion coefficient.* The *three* in the denominator of D comes from the dimensionality of the system under consideration.

Note that the Usadel equation provides a description of the dirty media in terms of uniquely the angle averaged GF, $\breve{g}_0$ and, hence, the 0 index is usually dropped from the notation. This will be the case in subsequent chapters of the thesis. When the overall dependence of the GF is not explicitly indicated one should be able to distinguish between the quasiclassical GF in Eilenberger equation, $\breve{g}(\mathbf{x}, \mathbf{n}, \varepsilon)$, and the isotropic one in Usadel equation, $\breve{g}_0(\mathbf{x}, \varepsilon)$, from the context.

---

[4] Note that we are working in $\hbar = 1$ units. Otherwise $\Phi_0 = \frac{h}{2e}$.

2.4.2.1 Calculation of observables

The expressions for the observable quantities in the diffusive limit directly follow from Eqs. (2.35)–(2.40) and the expansion of the quasiclassical GF in terms of an isotropic and an anisotropic part, Eq. (2.42). We list them here, though, to serve as a reference in the subsequent chapters. These are the explicit expressions for *(a)* the charge density:

$$\rho(\mathbf{x}) = -\frac{e}{16}\nu_0 \int d\varepsilon \mathrm{Tr}\left[\hat{\tau}_3 \check{g}_0^K(\mathbf{x},\varepsilon)\right], \tag{2.51}$$

(b) the spin density along the a quantization axis:

$$s^a(\mathbf{x}) = \frac{1}{16}\nu_0 \int d\varepsilon \mathrm{Tr}\left[\hat{\sigma}^a \check{g}_0^K(\mathbf{x},\varepsilon)\right], \tag{2.52}$$

(c) the energy density:

$$q(\mathbf{x}) = \frac{1}{16}\nu_0 \int d\varepsilon\ \varepsilon\ \mathrm{Tr}\left[\check{g}_0^K(\mathbf{x},\varepsilon)\right], \tag{2.53}$$

(d) the self-consistent superconducting gap:

$$\Delta(\mathbf{x}) = \frac{g}{16i}\nu_0 \int d\varepsilon \mathrm{Tr}\left[\left(\hat{\tau}_2 + i\hat{\tau}_1\right)\check{g}_0^K(\mathbf{x},\varepsilon)\right], \tag{2.54}$$

(e) the j component of the charge current density:

$$j_j(\mathbf{x}) = -\frac{\sigma_n}{16e} \int d\varepsilon \mathrm{Tr}\left[\hat{\tau}_3 \left(\check{g}\nabla_j\check{g}\right)^K(\mathbf{x},\varepsilon)\right], \tag{2.55}$$

(f) the j component of the spin current density polarized along the a quantization axis:

$$\dot{s}_j^a(\mathbf{x}) = -\frac{\sigma_n}{16e^2} \int d\varepsilon \mathrm{Tr}\left[\hat{\sigma}^a \left(\check{g}\nabla_j\check{g}\right)^K(\mathbf{x},\varepsilon)\right], \tag{2.56}$$

and *(g)* the j component of the energy current density:

$$\dot{q}_j(\mathbf{x}) = -\frac{\sigma_n}{16e^2} \int d\varepsilon\ \varepsilon\ \mathrm{Tr}\left[\left(\check{g}\nabla_j\check{g}\right)^K(\mathbf{x},\varepsilon)\right], \tag{2.57}$$

Here $\sigma_n = e^2 D\nu_0$ is the normal-state Drude conductivity.

2.4.3 Boundary conditions

Throughout Sec. 2.4 we have discussed how the quasiclassical approximation helps describing system where spatial changes happen at length scales much larger than the Fermi characteristic length, k_F^{-1}, and energies much smaller than the Fermi level, μ. This is indeed the case for bulk superconductors. However, we are interested in combining different materials to form complex structures. Interfaces between materials pose a special problem because they represent a strong perturbation that varies along atomic length scales, which cannot be treated quasiclassically. In this section we discuss how to match the quasiclassical GFs across interfaces between materials with the help of appropriate boundary conditions (BCs), which can be either derived heuristically, or from microscopic models for the interface.

For the non-quasiclassical objects, like the spinors that solve the BdG equations in Sec. 2.2, $\Psi(\mathbf{x})$, or the exact GFs obtained from the Gor'kov equations in Sec. 2.3, $\check{G}(\mathbf{x}_1, \mathbf{x}_2)$, the boundary conditions at the interfaces are familiar to anyone that has studied basic quantum mechanics: both the object and its spatial derivatives must be continuous everywhere in the space. In the case of quasiclassical propagators this is not generally the case. In Fig. 2.2 we show a pictorial representation of the spatial dependence of the exact (dashed blue line) and quasiclassical GFs (solid red line) across the interface between two materials, represented by the green and grey shaded areas. The exact GF shows fast oscillations at the k_F^{-1} scale, whereas $\check{g}$ only collects the overall spatial evolution of $\check{G}$ over much larger length scales. As a consequence, when the changes of physical properties across the interface happen in an atomic scale (Fig. 2.2b) the quasiclassical propagator cannot follow the exact one and shows a discontinuity. From a scattering perspective, part of an incident wave gets back-scattered after hitting the interface and part of it gets transferred across it. As usual, the scattering information is encoded on the form of phase shifts in the fast oscillations of $\check{G}$. Scattering processes like these ones couple quasiparticles with different momentum, $\boldsymbol{p}$, and goes against the quasiclassical assumption. By contrast, if the properties of the medium across the interface changes in a scale much larger than k_F^{-1} (Fig. 2.2a) the quasiclassical propagator is able to follow the overall evolution of the exact GF and thus $\check{g}$ remains continuous across the boundary. In such type of interfaces incident waves are not back-scattered, in accordance with the quasiclassical assumption. For this reason we usually refer to these sort of boundaries as *transparent interfaces.*

The calculation of the proper boundary conditions that bridge the quasiclassical GFs across different interfaces is a difficult topic that has attracted consid-

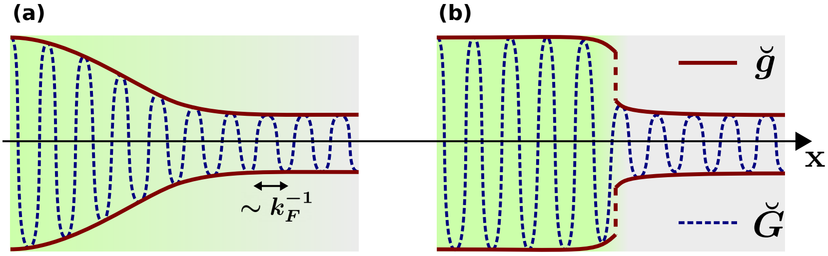

Figure 2.2: Pictorial representation of the spatial dependence of the exact (dashed blue line) and quasiclassical (solid red line) GFs, $\breve{G}$ and $\breve{g}$, respectively, at the boundary between two different media. Green and grey shaded areas represent the two media with different physical properties. When the physical properties at the boundary change (a) in a length scale much larger than k_F^{-1}, then $\breve{g}$ is continuous. Otherwise (a) the quasiclassical GF presents a discontinuity at the boundary. By contrast, both the exact GF and its derivative remain continuous.

erable attention over more than thirty years. In this section we only present the BCs that will be used in the rest of the thesis. Those readers interested in the topic can read Refs. [133, 134] and Refs. [135, 136, 137, 138] for a derivation of BCs for ballistic and diffusive systems, respectively, near an interface. Whereas in Refs.[133, 135] the interfaces considered do not have spin-dependent fields, in Refs.[134, 136, 137, 138] the authors study spin active interfaces. Moreover, in Refs.[139, 140] BCs are given for junctions between two electrodes with a spin-dependent layer in-between. Such layer rewards the transfer of one spin-direction across the junction over the other one, which results into an spin-filtering effect. In all the cases the interfaces are assumed to be (quasi-)homogeneous along the interface plane, *i.e.*, that the quasiclassical limit is only broken along the direction perpendicular to the surface.

In the works presented in this thesis we focus on two types of interfaces. On the one hand, we consider transparent interfaces (*c.f.* Fig. 2.2a) in ballistic systems that are described by the continuity of the quasiclassical GFs:

$$\breve{g}^L(\boldsymbol{r}_I) = \breve{g}^R(\boldsymbol{r}_I). \tag{2.58}$$

Here $\boldsymbol{r}_I$ is the position of the interface and $\breve{g}^L$ and $\breve{g}^R$ stand for the quasiclassical GFs that fulfill the Eilenberger equation, Eq. (2.31), of the system at the left and right sides of the interface, respectively.

On the other hand we study diffusive hetersotructures with high-resistance interfaces between the different constituents (Fig. 2.2b). High-resistance junctions like these ones are often known as *weak links*. In these cases it is not the quasiclassical GF that is continuous across the junction, but the current. The connection between the diffusive-limit GFs at opposite sides of an interface with a spin-dependent value of the conductivity (*a.k.a.* spin active interface) reads [139, 140],

$$n_j \breve{g} \partial_j \breve{g}\Big|_{r=r_I} = \frac{G_\square}{\sigma_n} \left[\hat{\Gamma} \breve{g}_0^L \hat{\Gamma},\ \breve{g}_0^R \right]_{r=r_I}, \tag{2.59}$$

where n_j is the unit vector normal to the interface, $G_\square$ is the conductance per unit area of the interface and σ_n is the normal-state conductivity. The precise theoretical definition of $G_\square$ is given in Refs. [140, 138], but in experiments it is usually used as a fitting parameter. The quasiclassical GFs, $\breve{g}_0^L$ and $\breve{g}_0^R$, fulfill the Usadel equation, Eq. (2.50), at the left and right sides of the interface, respectively. In Eq. (2.59), the matrix $\hat{\Gamma}$ describes the spin-filtering effects of the layer and it reads,

$$\hat{\Gamma} = u + v \hat{\sigma}^z \hat{\tau}_3, \tag{2.60}$$

where the parameters u and v depend on the polarization of the barrier, P, as follows:

$$u = \sqrt{\frac{1 + \sqrt{1 + P^2}}{2}}, \qquad v = \sqrt{\frac{1 - \sqrt{1 - P^2}}{2}} \tag{2.61}$$

and we assumed that the polarization happen along the z axis. One can easliy check from the expressions in Eq. (2.61) that $u^2 + v^2 = 1$, that $2uv = P$ and that $u^2 - v^2 = \sqrt{1 - P^2}$.

In Eq. (2.61) the polarization parameter ranges between the values $-1 < P < 1$ and it indicates how favorable is the transmission through the interface of quasiparticles with one spin orientation along the z axis over quasiparticles with the opposite spin. A value of $P = 1$ ($P = -1$) means that means that only spin-up (-down) quasiparticles can travel through the barrier, whereas spin-independent transport is given by $P = 0$.

From Eq. (2.59) it directly follows that at the boundaries of a finite diffusive system $n_k J_k = 0$, *i.e.*, that there is no current flowing out to the vacuum. This relation is very useful to describe mesoscopic diffusive systems with reduced lateral dimensions and we will use it in this thesis to study quasi-1D and quasi-2D hybrid structures with superconductors.

2.5 Matsubara method and analytic continuation of the Green's functions

In several part of this thesis, we compute observable in systems at thermal equilibrium, for which we sometimes use the *Matsubara method* [141]. Within this method one transforms the energy integrals into infinite sums that often converge fast enough, thus leading to an advantage from the computational perspective. In this section we present a brief survey on the Matsubara technique. For a more complete study of the Matsubara method one can go to textbooks on Green's functions in solid state physics, like Refs. [142, 143, 144, 116, 119].

Matsubara method exploits the formal similarity between the Boltzmann occupation probability term, $e^{-\beta\mathcal{H}}$, and the time-evolution operator, $e^{i\mathcal{H}t}$, in the calculation of expectation values in the grand-canonical ensemble for the imaginary times, $t = i\beta$. One can, hence, construct a full formalism for the so-called *"temperature"* or *"imaginary time Green's functions"*, which, unlike *"ordinary"* GFs, Eq. (2.16), do not depend on time t_j, but rather on a fictitious *imaginary time*, $\tau_j = it_j$. When the Hamiltonian is time independent, it is sufficient to restrict the "time" variables to the range $0 < \tau_j < \beta$ so that its difference satisfies the condition $-\beta < \tau_1 - \tau_2 < \beta$. In this limited domain, the temperature GF displays the symmetry[116] $\check{G}(\tau_1 - \tau_2) = -\check{G}(\tau_1 - \tau_2 + \beta)$ (we drop the dependence of $\check{G}$ on the spatial coordinates to simplify notation). Because of this periodicity, the Fourier components of the temperature GFs are nonzero only for an infinite set of discrete (imaginary) frequency values, ω_n. These are called *Matsubara frequencies* and they equal $\omega_n = (2n + 1)\pi T$ in systems of Fermi particles.

In the frequency-space, the *temperature* GFs are defined only at the imaginary Matsubara energies, $i\omega_n$, whereas the *retarded* and *advanced* GFs are defined at the real-energy axis, ϵ. Thus, *analytic continuation* of these GFs provides us a Green's function, $\check{G}(\epsilon)$, that is defined in the entire complex plane. Because the retarded (advanced) GFs are not analytic in the lower (upper) half-imaginary plane, they are related to the analytic continued GF as follows: $\check{G}^R(\epsilon) = \lim_{\Gamma\to 0} \check{G}(\epsilon + i\Gamma)$ ($\check{G}^A(\epsilon) = \lim_{\Gamma\to 0} \check{G}(\epsilon - i\Gamma)$), where ϵ is in the real-energy axis and Γ is an arbitrarily small positive number. In the context of superconductivity, Γ is typically known as the *Dynes parameter*[5] [145, 146] and a finite positive value of it provides a phenomenological way to describe inelastic processes by softening the sharp features in the spectrum. At those real-energy values where $\check{G}^R(\epsilon) \neq \check{G}^A(\epsilon)$, the analytic continued GF presents a branch cut across which $\check{G}$

---

[5] Note that we use the same symbol sith a hat, $\hat{\Gamma}$, for the matrix describing spin-filtering barriers in Eq. (2.60).

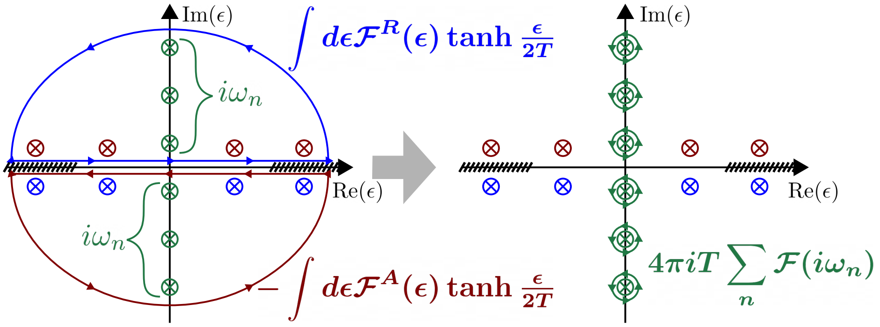

Figure 2.3: Deformation of the integration contours that yields the summation over Matsubara frequencies, ω_n. We indicate in blue, red and green some (arbitrary) poles of $\mathcal{F}^R$ and $\mathcal{F}^A$ and the poles of hyperbolic tangent, respectively. The slashed parts in the real axis indicate places where $\mathcal{F}(\epsilon)$ may be discontinuous (*i.e.* branch cuts of the complex function). The blue (red) contours on the left panel indicates the contour along the function $\mathcal{F}^R$ ($\mathcal{F}^A$) is integrated. Because $\mathcal{F}^R$ ($\mathcal{F}^A$) is analytic in the (lower-) upper-half imaginary plane, as long as $\mathcal{F}$ decays faster than ϵ^{-1} at the infinities, we can always transform the contours in the left panel to the sum over Matsubara frequencies, ω_n, shown in the right panel.

is discontinuous (slashed parts of the real axis in Fig. 2.3).

We can take advantage of the properties of the analytic continuation of the GF describe above to calculate observable quantities. In thermal equilibirum the computation of an observable from the quasiclassical GFs typically involves integrals of the form:

$$\int d\epsilon \left[\mathcal{F}^R(\epsilon) - \mathcal{F}^A(\epsilon)\right] \tanh \frac{\epsilon}{2T}. \tag{2.62}$$

Here, T is the temperature of the system, the hyperbolic tangent is the distribution function, Eq. (2.34), and $\mathcal{F}^R$ and $\mathcal{F}^A$ stand for an arbitrary functional only including retarded and advanced quasiclassical GFs, respectively. The analytical continuation of $\check{G}$ also provides a way to define $\mathcal{F}(\epsilon)$ all across the complex energy plane, which inherits the analytic properties of the GF, notably the branch cuts in the real energy axis.

Having the analytic continuation of $\mathcal{F}(\epsilon)$ all across the complex plane we can evaluate the integral in Eq. (2.62) using the *residue Theorem*, as long as the function under the integration sign converges fast enough. In the left part of Fig. 2.3 we show the way to close the contours. The contour for the integral of the retarded (advanced) term in Eq. (2.62) is represented in blue (red), whereas the

"⊗" symbols in blue, red and green point the (possible) positions of the poles of $\mathcal{F}^R(\epsilon)$, $\mathcal{F}^A(\epsilon)$ and the hyperbolic tangent, respectively. Note that the hyperbolic tangent has poles at the Matsubara frequencies, $\epsilon = i\omega_n \equiv (2n+1)i\pi T$. One can, then, deform the contours on the left side if Fig. 2.3 into the ones shown in the right side of the same figure, relating the integral in Eq. (2.62) to an infinite sum of the function $\mathcal{F}(\epsilon)$ over the Matsubara frequencies, as follows:

$$\int_{-\infty}^{\infty} d\epsilon \left[\mathcal{F}^R(\epsilon) - \mathcal{F}^A(\epsilon)\right] \tanh\frac{\epsilon}{2T} = 4\pi i T \sum_{n=-\infty}^{\infty} \mathcal{F}(i\omega_n). \tag{2.63}$$

This recipe holds for any calculation of observable quantities at thermal equilibrium and it is particularly beneficial for numerical evaluation. Close to the real-energy axis the $\mathcal{F}(\epsilon)$ function typically present tricky analytical properties and, when superconductivity is involved in the problem, it usually present sharp features that hinders numerical evaluation of the integrals. Along the imaginary axis, though, $\mathcal{F}(\epsilon)$ varies slowly. The sum converges faster with increasing value of the temperature, T. We can also take advantage of a mathematical technique known as the *Gaussian quadrature* [147] to reach a faster convergence of the sum. By contrast, when $T \longrightarrow 0$ the sum can be converted again into an integral according to Riemann's definition of an integral,

$$\lim_{T\longrightarrow 0} 4\pi i T \sum_{n=-\infty}^{\infty} \mathcal{F}(i\omega_n) = 2i \int_{-\infty}^{\infty} d\omega \mathcal{F}(i\omega). \tag{2.64}$$

Unlike in the integral of Eq. (2.62), here the integrand does not present the sharp features typical of the superconducting state.

Chapter 3

Magnetic impurities and chains in superconductors

According to Anderson's theorem [113], non-magnetic impurities[1] in a conventional superconductor do not modify substantially its spectrum. On the other extreme, a small concentration of magnetic impurities can destroy superconductivity [148, 149, 95, 96]. When such magnetic defects are isolated, though, they lead to bound states localized around them [90, 91, 92, 89, 95, 150, 96, 151, 152, 153, 154, 94]. The study of these bound states around magnetic impurities and Josephson magnetic junctions has attracted a great deal of attention in the past years. In this context, it is essential to understand the spectral properties around the magnetic region. In a quasi one-dimensional (quasi-1D) setup[2], this is equivalent to study the spectrum of a superconductor-ferromagnet-superconductor (SFS) junction. The features of such bound states depend on the size of the magnetic impurity and the strength of the exchange interaction [94].

Ballistic SFS junctions have been widely explored in the past, mainly in two limiting cases. One of them is the quasiclassical limit [155, 29, 30, 156, 157], in which the Fermi energy, μ, is assummed to be much larger than any other energy involved in the system, including the superconducting gap, Δ, and the Zeeman splitting, h. In this limit, one can directly apply the Bohr-Sommerfeld semiclassical quantization condition [158] and demonstrate that, in the absence of interface barriers, the spectrum consists of two double-degenerate Andreev bound states with opposite energies. This degeneracy of the bound states reflects the degeneracy of the $\pm k_F$ Fermi momentum valleys, which remain uncoupled

---

[1] regions of much smaller size than the superconducting coherence length, ξ_0.

[2] a wire which lateral dimensions are much smaller than ξ_0.

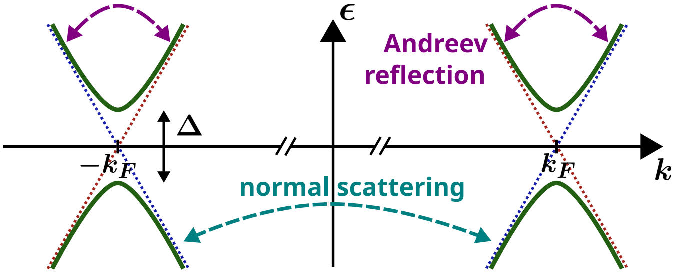

Figure 3.1: Schematic representation of the specturm of a quasi-1D s-wave superconductor. The electron- (dashed blue line) and hole-branches (dashed red line) couple forming valleys (solid green line) and opening a gap equal to Δ at the Fermi surface. As sketched by the dashed arrows, Andreev reflections couple electron- and hole-branches within each valley, whereas normal back-scattering events couple quasiparticles at different valleys.

in the absence of normal reflection, as it is schematically shown in Fig. 3.1.

The second widely studied limiting case corresponds to the situation where the spin-splitting field is very large, $h \gg \mu$, and concentrated in a region much smaller than k_F^{-1} [90, 91, 92, 150, 93]. This has been described as δ-like magnetic impurity that strongly couples both propagation directions to form two non-degenerate bound states within the gap with opposite energies. These states, known as the Yu-Shiba-Rusinov (YSR) states, may cross the Fermi level at a certain strength of the exchange energy. At this crossing, the system undergoes a quantum phase transition (QPT) [95, 96] that has been widely studied within the δ-like impurity model. This QPT is characterized by the change of the total spin of the system at zero temperature by one unit of electronic spin, $\hbar/2$. The discussion of whether such a QPT may take place beyond the impurity model was an open question. To address it, one needs to understand how these two known limiting cases are connected. This is what we do in Secs. 3.1.1 and 3.2, based on the work presented in Ref. [94].

In a periodic arrangement of magnetic impurities, as for example a chain, the single-impurity bound states hybridize and form bands within the superconducting gap. Such bands have been widely studied for atomic-sized magnetic impurities [102, 103, 104, 105, 106, 107, 108, 109, 110]. The hybridization of YSR states can lead to topological phases which host Majorana bound states at the ends of the impurity chain. In Refs. [111, 112] we proposed the analog of such atomic chains in a mesoscopic structure with lateral dimensions smaller than the superconducting coherence length, ξ_0. The magnetic impurities are replaced by semiclassical magnetic regions realized, for example, by the contact to magnetic materials. Mesoscopic structures involving superconductors and ferromagnetic materials have been extensively studied, mainly in the diffusive limit, in the context of superconducting spintronics [29, 30, 159, 160, 161, 162, 163, 164]. Our focus is from a very different perspective. We consider clean superconducting wires with a periodic array of magnetic regions as a mesoscopic realization of crystals, which we call *Andreev crystals* (ACs). Specifically, in Sec. 3.3 we present the general theory of ACs, including non-collinear magnetization orientation and arbitrary separation between the magnetic impurities.

This chapter is organized as follows: in Sec. 3.1, we discuss some general results on the spin polarization in gapped systems with colinear spin fields. We show two different methods to calculate it in terms of a generalized phase shift and in terms of the spectral asymmetry of the Hamiltonian. In Sec. 3.2, we study the spectral properties of ballistic quasi-1D SFS short junctions. In such a system the ferromagnetic region acts as a magnetic impurity, which let us explore the problem of a single magnetic impurity in a superconductor beyond the limits where it had been previously studied. Finally, in Sec. 3.3, we introduce the concept of quasi-1D *Andreev crystals* and fully discuss their spectral properties. We restrict our study to single and junctions between two helical ACs[3] and, in particular, we obtain full analytical results for systems involving ferromagnetic and antiferromagnetic ACs.

3.1 Spin polarization in gapped systems with colinear spin fields

In this section we show that the spin polarization of a gapped system can only change its value by an integer times the electronic spin unit, $\hbar/2$, after gap closing events. We present two alternative demonstrations based on our previous works [94, 111]. The first demonstration (Sec. 3.1.1) relates the total ground-state spin of the gapped system to a generalized phase shift, in a similar way to the well-known Friedel sum rule. The second approach (Sec. 3.1.2) relates the spin polarization to the *spectral asymmetry index*, a quantity used in topology [165, 166, 167], quantum field theory and condensed matter physics[168, 169, 170, 171, 172].

In both cases, we consider a superconducting system in the presence of a potential with a spin-dependent part parallel to the z-axis (*i.e.* it commutes with

---

[3] *i.e.* ACs where the magnetization of the impurities forming the chain rotates by a constant angle between subsequent impurities, forming a helix.

$\hat{\sigma}^z$). The BdG Hamiltonian [see Eq. (2.10)] describing such a system is block diagonal in spin with

$$\hat{\mathcal{H}}_\sigma(\boldsymbol{r}) = \hat{\mathcal{H}}_0 + \hat{V}_\sigma(\boldsymbol{r}). \tag{3.1}$$

Here,

$$\hat{\mathcal{H}}_0 = \zeta \hat{\tau}_3 + \Delta \hat{\tau}_1, \tag{3.2}$$

is the unperturbed BdG Hamiltonian of the system and

$$\hat{V}_\sigma(\boldsymbol{r}) = V_0(\boldsymbol{r})\hat{\tau}_3 - \sigma h(\boldsymbol{r}), \tag{3.3}$$

is the perturbation potential, consisting on an electrostatic field-like part, $V_0(\boldsymbol{r})$, and an exchange field-like part, $h(\boldsymbol{r})$. In Eqs. (3.1), (3.2) and (3.3), ζ stands for the quasiparticle energy operator, Δ is the superconducting order parameter and σ is the spin index, which throughout this chapter is substituted by $\sigma =\uparrow (\downarrow)$ when it appears as a subscript and by $\sigma = +(-)$ when it is part of an equation to label spin up (down) quasiparticles.

The results obtained in this section are fundamental for the rest of the chapter.

3.1.1 Phase shift approach

We start by considering the σ-spin component of the retarded exact GF obtained from the Gor'kov equations [see Eq. (2.19)] in energy space,

$$\hat{G}^R_\sigma(\epsilon) = \left(\epsilon - \hat{\mathcal{H}}_\sigma + i0^+\right)^{-1}, \tag{3.4}$$

where $\hat{\mathcal{H}}_\sigma$ is the BdG Hamiltonian for the spin component σ given in Eq. (3.1). The total electronic spin polarization along the z can be expressed in terms of the GF,

$$S^z = -\frac{\hbar}{4\pi}\int_{-\infty}^{\infty} d\epsilon \; \mathrm{Im}\left[\mathrm{Tr}\Big(\hat{G}^R_\uparrow(\epsilon) - \hat{G}^R_\downarrow(\epsilon)\Big)\right] f_F(\epsilon). \tag{3.5}$$

Here, $f_F(\epsilon) = (e^{\epsilon/k_B T} + 1)^{-1}$ is the Fermi distribution function and the trace runs over the whole coordinate ⊗ Nambu space.

The exact GF in Eq (3.5) can be also written in terms of the unperturbed GF, $\hat{G}_0$, and the potential, $\hat{V}_\sigma$, via Dyson's equation, $\hat{G}^R = \check{G}^R_0 + \hat{G}^R_0 \hat{V}_\sigma \hat{G}^R_\sigma$. Solving it for $\hat{G}^R_\sigma$ and substituting it back into the right hand side, we obtain the following expression determining the exact $\hat{G}^R_\sigma$:

$$\hat{G}^R_\sigma = \hat{G}^R_0 + \hat{G}^R_0 \hat{V}_\sigma (I - \hat{G}^R_0 \hat{V}_\sigma)^{-1} \hat{G}^R_0. \tag{3.6}$$

As the total spin of the unperturbed system is zero, only the second term on the right-hand side (r.h.s) of Eq (3.6) contributes to the trace in Eq (3.5).

Let us now assume that $\check{V}$ is an energy independent local perturbation. Noticing that $\left(\check{G}_0^R\right)^2 = -\frac{d\check{G}_0^R}{d\epsilon}$, one can use the cyclic property of the trace to obtain from Eq (3.5) the z-component of the total spin:

$$S^z = \frac{\hbar}{2}\int_{-\infty}^{\infty}\frac{d\epsilon}{2\pi}f_F(\epsilon)\frac{d}{d\epsilon}\left[\delta_\downarrow(\epsilon) - \delta_\uparrow(\epsilon)\right] , \tag{3.7}$$

where

$$\delta_\sigma(\epsilon) \equiv \mathrm{Im}\Big\{ \ln\left[\det(I - \hat{G}_0^R(\epsilon)\hat{V}_\sigma)\right]\Big\}, \tag{3.8}$$

is a generalized phase shift. Note that $\hat{V}_\sigma$ can have any spatial distribution and that the determinant inside the logarithm is the quantization condition coming from the Lippmann-Schwinger equation. In particular, zeros of this determinant determine the spectrum of the bound states. At zero temperature ($T = 0$), Eq (3.7) becomes especially simple,

$$2S^z/\hbar = \frac{1}{2\pi}\left[\delta_\downarrow(0) - \delta_\uparrow(0)\right]. \tag{3.9}$$

This result is analogous to the well-known Friedel sum rule that relates the charge/spin induced by a local perturbation to the phase shifts at the Fermi level.

The important feature of the superconducting state is its gap at the Fermi level ($\epsilon = 0$), where the unperturbed Green's function is real and, therefore, $\det(I - \sigma\hat{G}_0^R(0)\hat{V}_\sigma)$ is real too. Thus, $\delta_\sigma(0)/\pi$ can only take integer values, which will only change discontinuously by ±1 when a spin polarized bound state crosses the middle of the gap, as the determinant changes its sign. The electron-hole symmetry requires that the spin-up/down polarized states cross zero simultaneously while moving in opposite directions. As a result, at every crossing event the normalized spin $2S/\hbar$ jumps by one. The stepwise process of the spin polarization that follows from our phase-shift arguments agrees with the picture of Ref. [96] based on the analysis of the spin structure of the many-body BCS wavefunction in the δ-like impurity case. However, it should be noted that the result of this section is valid for any energy independent local perturbation potential $\check{V}$ acting on a system with a gap at the Fermi energy and Green's function $\check{G}_0$, as long as $\check{V}$ commutes both with $\check{G}_0$ and $\hat{\sigma}_z$.

In the above derivation we have only assumed that the perturbation $\hat{V}_\sigma$ is localized in space and has a collinear magnetic structure. Therefore our sum rule relating the total induced spin to the in-gap spectrum applies to any dimension and any size and shape of a finite magnetic region. For example, it can be directly used to analyze the behavior of the total spin in a magnetic chain on top of a superconductor, as the one studied in Ref. [173].

3.1.2 Spectral asymmetry index approach

In this section, we present an alternative way to calculate the total spin polarization in systems with collinear magnetization. We consider an s-wave superconductor in the presence of a spin dependent field described by the BdG Hamiltonian in Eq. (3.1). From the corresponding imaginary-frequency Green's functions (GFs), $\hat{G}_{\uparrow(\downarrow)}(\epsilon) = [i\epsilon - \hat{H}_{\uparrow(\downarrow)}]^{-1}$, one can compute the total spin polarization along the z axis of the system at zero temperature:

$$S^z = \frac{\hbar}{4}\lim_{\tau\to 0}\mathrm{Tr}\int\frac{d\epsilon}{2\pi}\left[\hat{G}_{\uparrow}(\epsilon) - \hat{G}_{\downarrow}(\epsilon)\right]e^{i\epsilon\tau}, \tag{3.10}$$

where the trace runs over the coordinate ⊗ Nambu space. Since the spin-up and -down components of the Hamiltonian are related by the transformation $\hat{H}_{\downarrow} = -\hat{\tau}_2\hat{H}_{\uparrow}\hat{\tau}_2$, then the GFs also fulfill that $\hat{G}_{\downarrow}(\epsilon) = -\hat{\tau}_2\hat{G}_{\uparrow}(-\epsilon)\hat{\tau}_2$. Substituting this relation into Eq. (3.10) and using the cyclic property of the trace we obtain:

$$\frac{2S^z}{\hbar} = \frac{1}{2}\lim_{\tau\to 0}\mathrm{Tr}\int\frac{d\epsilon}{2\pi}\left[\frac{1}{i\epsilon - \hat{H}_{\uparrow}} + \frac{1}{-i\epsilon - \hat{H}_{\uparrow}}\right]e^{i\epsilon\tau} = -\frac{1}{2}\lim_{\tau\to 0}\sum_n \mathrm{sgn}(E_{n\uparrow})e^{-|E_{n\uparrow}|\tau}, \tag{3.11}$$

where $E_{n\uparrow}$ stands for the energy of the n-the eigenstate of the spin-up Hamiltonian. The expression in the last line corresponds to the difference between the number of states below and above the Fermi energy for a given spin projection, and it is known as the spectral asymmetry index, widely used in topology [165, 166, 167], quantum field theory and condensed matter physics[168, 169, 170, 171, 172]. In a gapped system, an adiabatic deformation of the Hamiltonian can only change the value of this index by closing and reopening the gap. The need to close the gap to change the spin polarization of the system is in full agreement with the result that we presented in Sec. 3.1.1. In the following sections we will use either of these two arguments to describe the evolution of the spin polarization, depending on the context.

3.2 Spectral properties of ballistic SFS junctions

A ballistic quasi-1D superconductor-ferromagnet-superconductor (SFS) junction constitutes a good example of a gapped system with collinear spin fields. In this section, we study the spectral properties of such systems beyond the commonly studied limits that give rise to the well-known Andreev and Yu-Shiba-Rusinov (YSR) bound states. Among other things, we use the results presented in Sec. 3.1 to discuss the dependence of the polarization of the junction with the strength of the magnetic link.

The results of this section have been originally presented in Ref. [94]. The goals are twofold. On the one hand, we derive a general expression, Eq (3.18), that determines the subgap spectrum of a one-dimensional junction in terms of the normal-state transfer matrix for an arbitrary spin-dependent potential describing the F region, assuming that $\Delta = 0$ within F. For the particular case of a collinear (unidirectional) magnetization in the F region, the generalized Friedel sum rule adapted for the superconducting state that we obtained in the previous section, Eq. (3.9), states that every time a bound state crosses the Fermi energy, the total electronic spin changes by the amount of $\hbar/2$. On the other hand, we use these findings to provide a complete analysis of the subgap spectrum of a ballistic one-dimensional SFS junction for and arbitrary homogenoeus exchange field h. We focus on the short junction regime, where the ferromagnetic region is shorter than the superconducting coherence length, ξ_0. In this case, the presence of a superconducting gap in the ferromagnet due to the proximity effect has no effect on the subgap spectral properties of the junction, so we set $\Delta = 0$ in F. For this system we obtain the normal-state transfer matrix and, from it, we determine all spectral properties of the system from the central expression, Eq (3.18). We recover the well-established limiting cases, i.e. delta-like and semiclassical magnetic region, but also the subgap spectrum for all intermediate situations. We identify the values of the exchange field h and width of the magnetic regions, d, at which zero-energy crossings of bound states occur. As in the YSR case, these crossings are associated with a QPT, which manifests as a change of the total electronic spin of the system, in accordance with the sum rule derived in section 3.1.1. We finally demonstrate that this change of the total spin at the QPT is associated with the change of sign of the supercurrent in the SFS junction or, equivalently, to a change of the ground state phase difference between the superconductors from 0 to π.

3.2.1 The model

We consider a one-dimensional geometry consisting of a superconducting wire interrupted by a ferromagnetic region, as sketched in Fig. 3.2. The BdG Hamil-

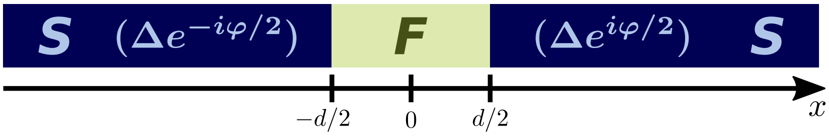

Figure 3.2: Sketch of the ballistic SFS junction under consideration. Two semi-infinite quasi-1D superconducting electrodes, with a superconducting phase difference φ, are separated by a ferromagnetic region of width d and a constant exchange field h pointing along the z axis.

tonian of the system reads

$$\check{\mathcal{H}}(x) = \begin{pmatrix} -\frac{\hbar^2\partial_x^2}{2m} - \mu - \hat{V}(x) & \Delta(x) \\ \Delta^*(x) & \frac{\hbar^2\partial_x^2}{2m} + \mu + \hat{V}^c(x) \end{pmatrix} . \tag{3.12}$$

Here μ is the chemical potential, $\Delta(x)$ is the superconducting gap that is only finite on the S electrodes, $\Delta(|x| > d/2) = |\Delta|e^{\pm i\varphi/2}$, the length of the F region is labeled by d and $\pm\varphi/2$ is the superconducting phase, where the plus (minus) sign stands for the right (left) superconductor. The potential $\hat{V}(x) = V_0(x) + \boldsymbol{h}(x)\cdot\hat{\boldsymbol{\sigma}}$ is only finite, but arbitrary, within the region $|x| < d/2$ and it consists of an scalar component V_0 and a spin-dependent one $\boldsymbol{h}(x)\cdot\hat{\boldsymbol{\sigma}} = h^a(x)\hat{\sigma}^a$, where we sum over repeated indices. The c superscript denotes time-reverse conjugation, $\hat{V}^c = \hat{\sigma}^y\hat{V}^*\hat{\sigma}^y$.

We focus on the subgap spectra, $\epsilon < |\Delta|$, which determines the main transport features at zero voltage and low temperatures. For such energies, the decaying wavefunctions into the left (L) and right (R) superconducting leads for each spin component read

$$\Psi_L^\sigma(x < \tfrac{-d}{2}) = e^{x/\xi}\left[\begin{pmatrix} A_L^\sigma \\ A_L^\sigma e^{i\alpha}e^{-i\varphi/2} \end{pmatrix} e^{ik_Fx} + \begin{pmatrix} B_L^\sigma \\ B_L^\sigma e^{-i\alpha}e^{-i\varphi/2} \end{pmatrix} e^{-ik_Fx}\right], \tag{3.13}$$

$$\Psi_R^\sigma(x > \tfrac{d}{2}) = e^{-x/\xi}\left[\begin{pmatrix} A_R^\sigma \\ A_R^\sigma e^{-i\alpha}e^{i\varphi/2} \end{pmatrix} e^{ik_Fx} + \begin{pmatrix} B_R^\sigma \\ B_R^\sigma e^{i\alpha}e^{i\varphi/2} \end{pmatrix} e^{-ik_Fx}\right], \tag{3.14}$$

where the upper (lower) element of the Nambu spinors stand for electrons (holes), the index σ labels the spin components, $\xi = \hbar v_F/\sqrt{\Delta^2 - \epsilon^2}$ is the decaying length of the wavefunction into the superconductor and k_F and v_F stand for the Fermi wavenumber and the Fermi velocity respectively. The quantity α is the phase associated with each Andreev reflection at the S/F interface and it is given by $\cos\alpha = \frac{\epsilon}{\Delta}$. The coefficients $A_{L(R)}^\sigma$ and $B_{L(R)}^\sigma$ in Eqs (3.13) and (3.14) are the constants of integration at the left (right) superconductor for the quasiparticles consisting

Figure 3.3: Andreev loop. The dark areas correspond to the superconducting electrodes, whereas the light area in between is the ferromagnetic region. Electrons and holes are represented with “e” and “h” symbols, respectively, and the solid (dashed) lines indicate propagation between (Andreev reflections at) the S/F interfaces.

of right moving (those multiplied by $e^{ik_F x}$) and left moving (those multiplied by $e^{-ik_F x}$) electrons, respectively.

At this stage it is convenient to define the four-element vectors,

$$\mathbf{C}_{L(R)} \equiv (A^+_{L(R)}, B^+_{L(R)}, A^-_{L(R)}, B^-_{L(R)})^T, \tag{3.15}$$

for the left (right) superconductor. The wave functions on opposite sides of the F region are connected via the normal state electronic T-matrix, $\check{T}$

$$\mathbf{C}_R = \check{T}\mathbf{C}_L \tag{3.16}$$

for the electrons and

$$\mathbf{C}_R = e^{-i\varphi} e^{i\check{\alpha}} \check{T}^c e^{i\check{\alpha}} \mathbf{C}_L \tag{3.17}$$

for the holes. In Eqs (3.16) and (3.17), $e^{i\check{\alpha}}$ is a short-hand notation for a matrix with the elements $[e^{i\alpha}, e^{i\alpha}, e^{-i\alpha}, e^{-i\alpha}]$ in the diagonal and zeros elsewhere. Notice that time conjugation also implies to change the sign of the quasiparticle energy ($\epsilon \longrightarrow -\epsilon$), so that $\check{T}^c(\epsilon) = \hat{\sigma}_y \check{T}^*(-\epsilon)\hat{\sigma}_y$.

After substitution of $\mathbf{C}_R$ from Eq (3.16) into Eq (3.17) and multiplication by $\check{T}^{-1}$ from the left one obtains a homogeneous equation for $\mathbf{C}_L$ that leads to the condition determining the bound states:

$$\det\left(e^{i\varphi} - \check{T}^{-1} e^{i\hat{\alpha}} \check{T}^c e^{i\hat{\alpha}} \right) = 0\ . \tag{3.18}$$

This expression is a generalization of Beenakker’s equation for the Andreev spectrum of a SNS junctions derived from the scattering matrix [174]. The second term inside the determinant describes an *Andreev loop*, whose geometrical interpretation we show in Fig. 3.3. Namely, from right to left, first an electron from F is Andreev reflected as a hole at one F/S interface (dashed line on the right of Fig. 3.3). The hole propagates to the opposite interface (lower solid line of Fig. 3.3) and it is converted again into an electron via the Andreev reflection (left dashed line of Fig. 3.3). The electron is finally transferred back to the origin (solid line on the top of Fig. 3.3). After this cycle, the wavefunction accumulates a phase equal to φ.

3.2.2 The quasi-1D SFS junction

We now apply the results obtained in the previous section, Sec. 3.2.1, to compute the spectral properties of a quasi one-dimensional SFS junction. We assume that the scattering F region is described by the potential $\hat{V}(x) = h\hat{\sigma}^z$ in spin space for $|x| < d/2$, and $V = 0$ elsewhere. I such a case, the T-matrix in Eq (3.18) has a block-diagonal structure,

$$\check{T} = \begin{pmatrix} \hat{T}^{\uparrow} & 0 \\ 0 & \hat{T}^{\downarrow} \end{pmatrix} = \begin{pmatrix} T^{\uparrow}_{++} & T^{\uparrow}_{+-} & 0 & 0 \\ T^{\uparrow}_{-+} & T^{\uparrow}_{--} & 0 & 0 \\ 0 & 0 & T^{\downarrow}_{++} & T^{\downarrow}_{+-} \\ 0 & 0 & T^{\downarrow}_{+-} & T^{\downarrow}_{--} \end{pmatrix} . \tag{3.19}$$

This considerably simplifies the problem, since we only need to calculate the normal state transfer for each spin orientation, $\sigma = \{\uparrow, \downarrow\}$, separately. Because in the normal state electrons and holes are decoupled, we can focus only on the electrons. The wavefunction reads

$$\psi(x) = \begin{cases} A^{\sigma}_{L} e^{iq_0 x} + B^{\sigma}_{L} e^{-iq_0 x} & \text{if} \quad x < -d/2 \\ C^{\sigma} e^{iq_\sigma x} + D^{\sigma} e^{-iq_\sigma x} & \text{if} \quad -d/2 < x < d/2 \\ A^{\sigma}_{R} e^{iq_0 x} + B^{\sigma}_{R} e^{-iq_0 x} & \text{if} \quad x > d/2 \end{cases} , \tag{3.20}$$

where $q_\sigma = k_F\sqrt{1 + \frac{\epsilon + \sigma h}{\mu}}$ and $q_0 = k_F\sqrt{1 + \frac{\epsilon}{\mu}}$ are the wavenumbers at the ferromagnet and the normal metal, and μ and k_F are the Fermi energy and wavenumber, respectively. From the continuity of the wavefunction in Eq (3.20) and its first derivative, we obtain a set of four equations that we have to solve. First writing C^{σ} and D^{σ} in terms of A^{σ}_{L} and B^{σ}_{L}, and substituting them into the expressions for A_R and B_R, we get a connection between the wavefunction at the left and right superconductor,

$$\begin{pmatrix} A^{\sigma}_{R} \\ B^{\sigma}_{R} \end{pmatrix} = \begin{pmatrix} T^{\sigma}_{++} & T^{\sigma}_{+-} \\ T^{\sigma}_{-+} & T^{\sigma}_{--} \end{pmatrix} \begin{pmatrix} A^{\sigma}_{L} \\ B^{\sigma}_{L} \end{pmatrix} , \tag{3.21}$$

where the elements of the T-matrix, Eq. (3.19), read

$$\begin{cases} T^{\sigma}_{++} = \left[\cos\left(q_\sigma d\right) + \frac{i}{2}\frac{{q_\sigma}^2+{q_0}^2}{q_\sigma q_0}\sin\left(q_\sigma d\right)\right]e^{-iq_0 d} \\ T^{\sigma}_{+-} = \frac{i}{2}\frac{{q_\sigma}^2-{q_0}^2}{q_\sigma q_0}\sin\left(q_\sigma d\right) \end{cases}, \tag{3.22}$$

and the remaining two components are related to these ones by complex conjugation, $T^{\sigma}_{--} = (T^{\sigma}_{++})^*$ and $T^{\sigma}_{-+} = (T^{\sigma}_{+-})^*$. The diagonal terms, T^{σ}_{jj}, describe a direct transmission (forward scattering) within one electron-hole valley, whereas the off-diagonal terms represent backscattering events that couple the opposite valleys at $\pm k_F$ (see Fig. 3.1).

The solution of Eq. (3.18), after substitution of Eq. (3.22), determines the full subgap spectrum of the SFS junction. For analytic results, we focus on the semiclassical limit where μ is the largest energy, so that $\epsilon, \Delta, h \ll \mu$. In this case the quassiparticle momenta in the F and S regions are approximated by $q_\sigma(\epsilon) \approx k_F + \frac{\epsilon+\sigma h}{\hbar v_F}$ and $q_0(\epsilon) \approx k_F + \frac{\epsilon}{\hbar v_F}$, respectively. To the leading order in the semiclassical approximation, the off-diagonal elements of the T-matrix in Eq. (3.22) are negligible and the diagonal terms are given by $T^{\sigma}_{++} \approx e^{\sigma i\Phi}$, where $\Phi \equiv \frac{hd}{\hbar v_F}$ is referred to as the *magnetic phase*. This expression for the T-matrix has a simple physical interpretation: within the semiclassical approach the incoming electrons have an energy of the order of μ, much larger than the scattering potential height, h. Hence, incoming particles have a unit probability to be transmitted through the F region. Propagation through the F region results only in the additional phase, Φ. Clearly, the spectrum obtained from Eq. (3.18) in this limit coincides with the result of the Bohr-Sommerfeld quantization condition for the spectrum:

$$\frac{\epsilon d}{\hbar v_F} + \sigma\Phi - \arccos\frac{\epsilon}{\Delta} \pm \frac{\varphi}{2} = \pi n, \tag{3.23}$$

where n is an integer. Eq. (3.23) determines the spectrum of Andreev bound states (ABS) [157, 156]. In a short junction, $d \ll \xi_0$, where $\xi_0 \equiv \hbar v_F/\Delta$ is the superconducting coherence length, one obtains $\epsilon_\sigma = \pm\Delta\cos\left(\sigma\Phi + \frac{\varphi}{2}\right)$. It follows that by changing the magnetic phase, the energy of the ABS can be tuned between ±Δ. In particular, zero energy single states can be created by proper choice of Φ and φ.

The other widely studied limiting case is the YSR limit in which the F region is described by a δ-like potential, i.e. its length tends to zero, $d \longrightarrow 0$, while Φ is kept finite. One can read directly from Eqs (3.22) that, within this limit, $T^{\sigma}_{++} \approx 1 + \sigma i\Phi$ and the off-diagonal elements are non-zero, $T^{\sigma}_{+-} \approx \sigma i\Phi$. This means that, in the presence of a δ-like potential, the backscattering probability is finite. The latter leads to a coupling between the $\pm k_F$ valleys (see sketch in Fig. 3.2). Such coupling lifts the degeneracy at $\varphi = 0$ and "pushes" one of the states to energies closer to the continuum. By solving Eq (3.18) in this limit for a general value of φ, one obtains four bound states [93]:

$$\epsilon = \pm\frac{\Delta}{\Phi^2+1}\left[\Phi^4 + \frac{1-\cos\varphi}{2}\Phi^2 + \frac{1+\cos\varphi}{2} \pm \Phi\sqrt{2\Phi^2(1+\cos\varphi)+\sin^2\varphi}\right]^{1/2} . \quad (3.24)$$

Here, the ± signs are mutually independent and the bound states have to appear inside the gap, $|\epsilon| \leq \Delta$. For a zero phase-difference, $\varphi = 0$, there are only two states inside the gap, which correspond to the well-known YSR solution:

$$\epsilon = \pm\Delta\frac{1-\Phi^2}{1+\Phi^2} . \quad (3.25)$$

The other two states remain at the gap edges, $\epsilon = \pm\Delta$, independently of the value of Φ. Whereas the YSR are nondegenerate, ABS states, Eq (3.23), are double degenerate. Moreover, with increasing Φ the ABS cross zero energy every time $\Phi = (2n+1)\pi/2$. In contrast, YSR states cross the zero only once at $\Phi = 1$, where, as explained below, a quantum phase transition takes place [95, 96, 151].

3.2.3 Spectrum in an intermediate range of parameters

We address now the question about the spectrum in an intermediate case, between the semiclassical and the YSR limits. This may correspond to a cluster of magnetic atoms or a small ferromagnetic island with a large but finite exchange field. The expression determining the bound states can be obtained from Eqs. (3.18) and (3.22). After some algebra and exploiting the relations between the elements of the transfer matrix, we get a rather simple equation

$$\cos\varphi - \mathrm{Re}\left[T^{\sigma}_{+-}(T^{\sigma}_{+-})^c + e^{2i\alpha}(T^{\sigma}_{++})^* \, (T^{\sigma}_{++})^c\right] = 0, \quad (3.26)$$

from which, after substitution of the expressions for the elements of the T-matrix in Eq. (3.22), we obtain the following secular equation:

$$\begin{aligned} &2\cos\varphi - 2\cos(2\alpha)\cos(q_\sigma d)\cos(q^c_\sigma d) \\ &- \frac{k_F^2}{q_\sigma q^c_\sigma}\left[2cos(2\alpha) + \left(\frac{\epsilon+\sigma h}{\mu}\right)^2\sin^2\alpha\right]\sin(q_\sigma d)\sin(q^c_\sigma d) \\ &- \frac{q_\sigma^2+k_F^2}{q_\sigma k_F}\sin(2\alpha)\sin(q_\sigma d)\cos(q^c_\sigma d) + \frac{(q^c_\sigma)^2+k_F^2}{q^c_\sigma k_F}\sin(2\alpha)\cos(q_\sigma d)\sin(q^c_\sigma d) = 0. \end{aligned} \quad (3.27)$$

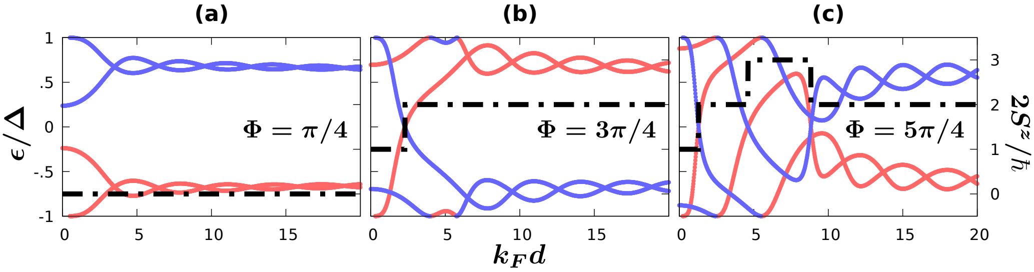

Figure 3.4: Energy of the bound states (solid lines) and the total spin $2S/\hbar$ (dashed line) of a SFS junction as a function of d for three different values of Φ, and $\mu/\Delta = 100$. Red and blue colors correspond to spin projections of the electronic states.

Here, $q_\sigma^c = k_F\sqrt{1 - \frac{\epsilon+\sigma h}{\mu}}$ is the time conjugate of the electron wavenumber in F and we have approximated $q_0 \approx k_F$, which is totally justified by the fact that $\Delta \ll \mu$ is fulfilled in any superconductor and that q_0 did not appear in any trigonometric function (where the accumulated phases along long distances would eventually be non-negligible, $\epsilon/\mu \cdot k_F d \sim 2\pi$).

In Fig. 3.4, we show with solid lines the subgap spectrum of the SFS structure as a function of the normalized length of the magnetic region, $k_F d$, for $\varphi = 0$. Different panels correspond to different values of the magnetic phase Φ. For small $k_F d \lesssim 1$ there are only two nondegenerate states within the gap. These are the YSR states. Figures 3.4(a) and 3.4(b) correspond, respectively, to the situations before and after the YSR states cross at zero energy. Further increase of Φ pushes the states towards the gap edges. In contrast, for longer junctions, $k_F d \gg 1$, two pairs of bound states can be found within the gap. These pairs of states are non-degenerate (except at certain values of $k_F d$) and their energy oscillates with a period $2\pi/k_F$ around the semiclassical value determined by Eq. (3.23). The oscillations stem from interference effects that are ignored in the semiclassical limit. Further increase of the junction length towards $d \sim \xi_0$ will bring additional bound states into the gap, which are not considered here.

It is worth noticing that Figs. 3.4(b-c) show zero-energy crossings for finite length junctions at $\varphi = 0$. At each crossing the total spin of the system change by one, as calculated from Eq. (3.7) and shown by dashed black lines in Fig. 3.4. In other words, Fig. 3.4 demonstrates that a QPT also takes place beyond the YSR limit. Moreover, a sequence of QPTs with a stepwise change of the total spin may exist in a finite length junction.

The number of zero-energy crossings as a function of d grows with increasing Φ. As it follows from Eq. (3.23), in a short junction within the semiclassical limit,

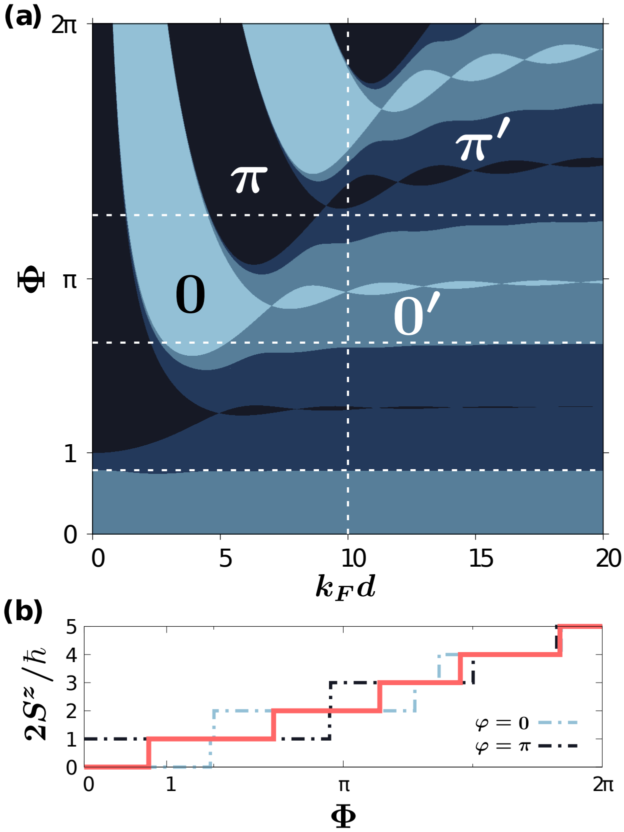

Figure 3.5: (a) Phase diagram of the SFS Josephson junction in terms of the length of the junction d and the magnetic phase Φ. The horizontal white dashed lines indicate the values of Φ chosen in Fig. 3.4. (b) Total electronic spin of a SFS junction of length $k_F d = 10$ (white dashed line in panel a) when one imposes 0-phase (dashed light) or π-phase (dashed dark). The red solid line shows the total spin when the junction stays in its ground state. Calculations have been done for $\mu/\Delta = 100$.

$k_F^{-1} \ll d \ll \xi_0$, the ABS cross zero periodically at values of the magnetic phase $\Phi = (2n+1)\pi/2$. Each of these "asymptotic" crossings should be accompanied with, at least, two additional zero-energy crossings at intermediate values of $k_F d$ [Fig. 3.4(b-c)]. Fast oscillations of the bound state energies as a function of d may increase further the number of zero-energy crossings by an even number of them [see Fig. 3.4(c)].

3.2.4 Josephson current

The subgap spectrum can be measured by means of tunneling spectroscopy [150, 175, 176, 177, 153]. In addition, measurements of the Josephson current in SFS junctions can also shed light on the spectral properties [178, 179], in particular on the ground state of the junction. In conventional SNS junctions the Josephson energy is minimized when the phase difference vanishes, $\varphi = 0$. However, it is known that, in SFS junctions, this minimum can also be found at $\varphi = \pi$ by tuning the exchange field or the length of the F region [97, 98, 99, 100, 101]. In the context of a delta-like magnetic impurity the connection between the zero energy YSR state and the 0-π transition has been recently discussed in Ref. [93]. As we discuss next, the transition between the 0- and π-junction behaviour is closely related to the QPTs described above for arbitrary junctions.

For this sake, we compute the ground state energy of the junction as a function of the phase difference φ. If the energy has a unique minimum at $\varphi = 0$ or $\varphi = \pi$, one says that the junction is in the 0- or π- phase respectively. If the Josephson energy has minima both at $\varphi = 0$ and at $\varphi = \pi$, then the ground state is denoted as $0'$ or π' depending on the location of the global minimum [180, 181, 182].

In Fig. 3.5(a), we show the phase diagram in the d-Φ plane. This diagram provides an interesting connection: the QPTs associated with the zero-energy crossings shown in Figs. 3.4(b-c) [horizontal dashed lines in Fig. 3.5(a)], correspond to transitions between the $(0, 0', \pi')$ states and the π state.

Finally, in Fig. 3.5(b) we show the dependence of the total spin of the system on Φ for a junction with $k_F d = 10$. The dashed light line (dashed dark line) shows the spin if the junction is forced to stay in the $0(\pi)$-state. The solid red line shows the spin of the system if the junctions always stays in the true ground state, i.e., if it follows the global energy minimum when the parameters are changed. Notice that, whenever the ground state corresponds to $\varphi = 0$ ($\varphi = \pi$), the total electronic spin of the system is even (odd).

3.3 Spectral properties of *Andreev crystals*

In the previous section, Sec. 3.2, we studied the spectral properties of states bounded to magnetic impurities in a superconductor. When putting several of these impurities together forming a chain, the single-impurity bound states hybridize and form bands within the superconducting gap. Those bands have been widely studied for atomic-sized magnetic impurities [102, 103, 104, 105, 106, 107,

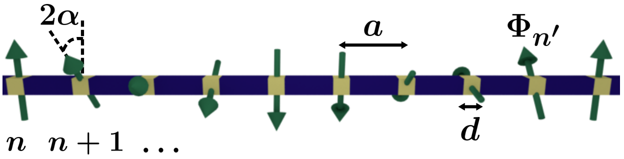

Figure 3.6: Sketch of a quasi-1D helical Andreev crystal formed by a superconducting wire interrupted by magnetic regions of width d separated by a constant distance a. It is assumed that where $k_F^{-1} \ll d \ll \xi_0$. The magnetization of the impurities rotates an angle 2α around the x axis between subsequent impurities.

108, 109, 110]. The hybridization of YSR states can lead to topological phases, which host Majorana bound states at the ends of the impurity chain. In this section we consider the analog of such atomic chains in a mesoscopic structure with lateral dimensions smaller than the superconducting coherence length, $\xi_0 \equiv \hbar v_F/\Delta$ (here, v_F is the Fermi velocity and Δ the superconducting order parameter) and replaced the magnetic impurities by semiclassical magnetic regions (see the sketch in Fig. 3.6). We use the quasiclassical method to determine the local spectral properties of such semiclassical crystals, which we call *Andreev crystals* (ACs) [111, 112]. Mesoscopic structures involving superconductors and ferromagnetic materials have been extensively studied in both the diffusive [29, 30, 159, 160, 161, 162, 163, 164] and ballistic limit [183, 184, 185, 186]. Our focus here is from a different perspective, more in line with those works on Shiba chains.

3.3.1 Model and main equations for the *Andreev crystal*

We consider a quasi-1D superconducting wire of lateral dimensions much smaller than the superconducting coherence length, ξ_0. The wire contains magnetic regions located at the points $X_n = na$, where a is the separation between the impurities and n is the impurity index. We assume that the width of the magnetic regions, d, is larger than k_F^{-1} and hence they can be considered within the semiclassical approach [94]. In addition, we also assume that $d \ll \xi_0$, such that we can treat the magnetic regions as point-like impurities in the semiclassical scale, with a polarization strength and direction proportional to the corresponding SU(2) magnetic phase [157, 156],

$$\hat{\boldsymbol{\sigma}} \cdot \boldsymbol{\Phi}_n \equiv \frac{1}{\hbar v_F} \int dx\ \hat{\boldsymbol{\sigma}} \cdot \boldsymbol{h}_n(x). \tag{3.28}$$

Here, v_F is the Fermi velocity, and $\boldsymbol{h}_n(x)$ is the exchange field vector induced by the n-th impurity, which is assumed to be parallel to the local magnetization of the magnetic region. The Bogoliubov-de Gennes (BdG) Hamiltonian [118] within the semiclassical approximation describing the AC in the Andreev limit reads,

$$\check{H}^{\eta}_{BdG}(x) = -i\eta\hbar v_F \hat{\tau}_3 \partial_x + \hat{\tau}_1 \Delta - \hbar v_F \sum_n \hat{\boldsymbol{\sigma}} \cdot \boldsymbol{\Phi}_n \delta(x - X_n), \tag{3.29}$$

where $\hat{\tau}_i$ are the Pauli matrices spanning the Nambu space (*i.e.*, the electron-hole space), $\hat{\boldsymbol{\sigma}} \equiv (\hat{\sigma}^x, \hat{\sigma}^y, \hat{\sigma}^z)$ stands for the vector of Pauli matrices that span the spin space and $\eta = \pm$ refers to the two electron-hole valleys at $\pm k_F$ (see Fig. 3.1). A distinctive feature of semiclassical impurities is that they do not trigger backscattering processes. This allows us to treat the two Fermi valleys separately and to drop the η index. In the Andreev equations [88], Eq. (3.29), the delta functions describe the boundary conditions within the semiclassical approach. Namely, they describe the phase gained by a quasiparticle when it traverses the magnetic region [see Eq. (3.33) below].

The solution of the BdG equations provides all the spectral information about the crystal. As it will be shown in Sec. 3.3.1.1, one can solve this problem analytically under the assumption that magnetic impurities are weakly coupled to each other, $e^{-a/\xi_0} \ll 1$. In this limit, the system can be described by an effective tight-binding model that provides the spectrum of this system. A drawback of this approach is that to compute observable quantities, such as the local density of states or the local spin density, one has to perform explicit summation over the Bloch momentum. Indeed, for calculation of observables it is more convenient to use the quasiclassical Eilenberger equation [128]. This formalism is presented in Sec. 3.3.1.2. Specifically, we show how to obtain exact analytical expressions for the quasiclassical Green's functions (GFs) of periodic ACs, and how to access to observables in a rather simple way. Thus, both formalism presented in Secs. 3.3.1.1 and 3.3.1.2 are complementary and provides a full description of ACs. Note that the quasiclassical approach requires the distance between the impurities to be larger than the Fermi wave length, $k_F a \gg 1$. Moreover, in the ferromagnetic alignment, in order to avoid the self-consistent computation of the superconducting gap, we assume that a is larger than (or of the same order of) ξ_0. In the antiferromagnetic case this restriction is relaxed due to the smaller effective exchange field.

3.3.1.1 Tight-binding equations

To obtain the spectral properties of an AC one needs to solve the Andreev equations,

$$\check{H}_{BdG}(x)\Psi(x) = \epsilon\Psi(x), \tag{3.30}$$

where $\check{H}_{BdG}(x)$ is the Hamiltonian, Eq. (3.29), and $\Psi(x)$ is a four-component bi-spinor in the Nambu⊗spin space. The general solution of Eq. (3.30) in the region between two neighboring impurities, $X_n < x < X_{n+1}$, reads

$$\Psi(x) = B^+_{n+1} e^{\frac{x-X_{n+1}}{\xi}} \left|+\right\rangle + B^-_n e^{-\frac{x-X_n}{\xi}} \left|-\right\rangle. \tag{3.31}$$

Here $\xi \equiv \frac{\hbar v_F}{\sqrt{\Delta^2-\epsilon^2}}$ is the energy-dependent superconducting coherence length, $B^{+(-)}_n$ is a two-component spinor (covering the spin space) that contains the amplitudes of the contributions to the wavefunction that decays from the n-th impurity into the left (right), and

$$\left|\pm\right\rangle \equiv \frac{e^{\pm i\theta/2}}{\sqrt{2\cos\theta}} \begin{pmatrix} 1 \\ \pm i e^{\mp i\theta} \end{pmatrix}, \tag{3.32}$$

are two-component spinors in the Nambu space, where $e^{i\theta} \equiv \frac{\sqrt{\Delta^2-\epsilon^2}+i\epsilon}{\Delta}$ is the Andreev factor. Direct product is assumed between the spinors in Nambu and spin spaces.

Within the semiclassical limit, quasiparticles traveling through the n-th semiclassical impurity do not back-scatter, but pick up a phase according to:

$$\Psi(X^R_n) = e^{i\hat{\tau}_3\hat{\boldsymbol{\sigma}}\cdot\boldsymbol{\Phi}_n}\Psi(X^L_n). \tag{3.33}$$

because of $\hat{\tau}_3$ and $\hat{\boldsymbol{\sigma}}\cdot\boldsymbol{\Phi}_n$, the sign of the accumulated phase is different for electron/holes and spin up/down quasiparticles along the exchange field direction, respectively. Applying these boundary conditions to the general wavefunction in Eq. (3.31) we obtain the equations for the $B^\pm$ coefficients, which can be recast into an effective tight-binding model by keeping terms up to first order in $e^{-a/\xi}$. In particular, in the limit where $e^{-a/\xi} \ll 1$, coefficients B^-_n at each site n can be related to their counterparts, B^+_n, as follows:

$$B^-_n = i\hat{\boldsymbol{\sigma}}_n \frac{\Delta\sin\Phi_n}{\sqrt{\Delta^2-\epsilon^2}} B^+_n, \tag{3.34}$$

where $\Phi_n = |\boldsymbol{\Phi}_n|$ is the strength of the magnetic phase vector, and we define $\hat{\boldsymbol{\sigma}}_n \equiv \frac{\hat{\boldsymbol{\sigma}}\cdot\boldsymbol{\Phi}_n}{\Phi_n}$. It is convenient to introduce the re-scaled coefficients, $b'_n \equiv \hat{\boldsymbol{\sigma}}_n \sin\Phi_n B^+_n$, which satisfy a tight-binding-like equation

$$\left(\omega - \hat{\boldsymbol{\sigma}}_n\omega_{0n}\right) b'_n = \hat{\boldsymbol{\sigma}}_{n+1} t_{n+1} b'_{n+1} + \hat{\boldsymbol{\sigma}}_n t_n b'_{n-1}. \tag{3.35}$$

Here $\omega \equiv \frac{\epsilon}{\sqrt{\Delta^2-\epsilon^2}}$, $\hat{t}_n \equiv -\frac{e^{-a/\xi}}{\sin\Phi_n}$ is the hopping amplitude, and $\omega_{0n} = \frac{\cos\Phi_n}{\sin\Phi_n}$ is the value of the function ω evaluated at the bound state energy in the n-th impurity, $\epsilon_{0n} = \frac{|\sin\Phi_n|}{\tan\Phi_n}$. In principle, Eq. (3.35) describes an arbitrary AC with lattice constant a. In Sec. 3.3.2 we analyze helical ACs composed by identical magnetic impurities with an spatially rotating magnetization, forming a helix in the y-z plane.

3.3.1.2 Eilenberger equation

Because of its simplicity, the tight-binding formulation, Eq. (3.35), is very useful for describing the spectral properties of ACs. However, one should bear in mind that it has been derived within first-neighbor approximation, and therefore it is valid as long as $e^{a/\xi} \ll 1$. To go beyond this approximation we introduce here the Eilenberger equation[128] from which we can determine the quasiclassical Green's functions.

We focus again on point like semiclassical magnetic impurities. The Eilenberger equation in the regions between the impurities has a simple form:

$$\hbar v_F \partial_x \check{g}(x) - \left[i\epsilon\hat{\tau}_3 + \Delta\hat{\tau}_2,\ \check{g}(x)\right] = 0. \tag{3.36}$$

Here $\check{g}(x)$ is the quasiclassical Green's function (GF), which is a 4×4 matrix in the Nambu×spin space that satisfies the normalization condition, $\check{g}^2 = 1$. The square brackets stand for the commutation operation, and Δ is the superconducting gap, which is assumed to be constant along the superconducting wire. Solving Eq. (3.36), we obtain the propagation of the GF along the superconducting region,

$$\check{g}(x) = \hat{u}(x - x_0)\check{g}(x_0)\hat{u}(x_0 - x), \tag{3.37}$$

where the propagator reads,

$$\hat{u}(x - x_0) = \hat{P}_+ e^{(x-x_0)/\xi} + \hat{P}_- e^{-(x-x_0)/\xi}. \tag{3.38}$$

Here $\hat{P}_\pm \equiv |\pm\rangle\langle\tilde{\pm}| = \frac{e^{\pm i\hat{\tau}_3\theta} \pm \hat{\tau}_2}{2\cos\theta}$ are two orthogonal projectors that span the Nambu space, $|\pm\rangle$ are the basis column vectors of Eq. (3.32) and

$$\langle\tilde{\pm}| \equiv \frac{e^{\pm i\theta/2}}{\sqrt{2\cos\theta}}\begin{pmatrix}1 & \mp ie^{\mp\theta}\end{pmatrix}, \tag{3.39}$$

are the co-basis row vectors orthonormal to $|\pm\rangle$. The inverse of the propagator in Eq (3.38) fulfills the relation $[\hat{u}(\tilde{x})]^{-1} = \hat{u}(-\tilde{x})$.

Additionally, the quasiclassical GF at the right and left sides of the n-th semiclassical impurity (X_n^R and X_n^L, respectively) are connected by a propagation-like boundary conditions,

$$\check{g}(X_n^R) = e^{i\hat{\tau}_3\hat{\sigma}\cdot\Phi_n}\check{g}(X_n^L)e^{-i\hat{\tau}_3\hat{\sigma}\cdot\Phi_n}. \tag{3.40}$$

This expression, together with Eq. (3.38), determines the GF at any space point provided its value at a given point, $\check{g}(x_0)$.

In an infinite periodic ACs we need to match the value of the GF at equivalent points of different unit cells. For this sake, it is useful to introduce the *chain propagator*, $\check{S}$, that describes the propagation of the quasiclassical GF from a given position inside a unit cell to the equivalent position in the subsequent unit cell, $\check{g}(x_0 + l) = \check{S}\check{g}(x_0)\check{S}^{-1}$ (here l denotes the length of the unit cell). The exact form of $\check{S}$ depends on the arrange of impurities and the choice of the initial point inside the unit cell, x_0. Here we choose for x_0 the left interface of one of the magnetic impurities. Thus the *chain propagator* reads

$$\check{S} \equiv \prod_{j=1}^{J} \hat{u}(a)e^{i\hat{\tau}_3\hat{\sigma}\cdot\Phi_j}, \tag{3.41}$$

where J is the number of impurities forming the unit cell. The value of the quasiclassical GF at x_0 is obtained from the periodicity along the unit cell, $\check{g}(x_0) = \check{S}\check{g}(x_0)\check{S}^{-1}$, together with the normalization condition, $[\check{g}(x_0)]^2 = 1$. Once $\check{g}(x_0)$ is determined the full quasiclassical GF, $\check{g}(x)$, is obtained after propagation using Eqs. (3.38) and (3.40).

From the knowledge of the GF, we can obtain the local density of states (LDOS),

$$\nu(x,\epsilon) = \mathrm{Re}\left\{\frac{1}{4}\mathrm{Tr}\left[\hat{\tau}_3\check{g}(x,\epsilon)\right]\right\}, \tag{3.42}$$

and the local spin density along the z axis,

$$s^z(x,\epsilon) = \frac{\hbar}{2}\mathrm{Re}\left\{\frac{1}{4}\mathrm{Tr}\left[\hat{\sigma}^z\hat{\tau}_3\check{g}(x,\epsilon)\right]\right\}, \tag{3.43}$$

where the traces run over the Nambu×spin space. In Sec. 3.3.3 we use this approach to obtain the quasiclassical GFs of ferromagnetic and antiferromagnetic ACs and we generalized this method to study junctions between different (anti-) ferromagnetic ACs.

3.3.2 *Dilute* helical Andreev Crystals

In this section, we study the spectral properties of ACs with a periodic rotation of the magnetization of the magnetic impurities, when the separation between the impurities is bigger than ξ_0 (thus the term *dilute*). For this sake, we use the tight-binding approach introduced in Sec. 3.3.1.1. In particular, we focus on an AC consisting of identical magnetic impurities whose magnetization is in the y-z plane and rotates by a constant angle, 2α around the x axis[4] (see Fig. 3.6). The SU(2) magnetic phase describing this situation is given by

$$\hat{\boldsymbol{\sigma}}_n \cdot \boldsymbol{\Phi}_n = \Phi e^{-i\hat{\sigma}^x \alpha n} \hat{\sigma}^z e^{i\hat{\sigma}^x \alpha n}, \tag{3.44}$$

where Φ is the strength of the magnetic phase. Its strength is the same in all the impurities. Substituting this expression into Eq. (3.35) we obtain that

$$\left[\omega - e^{i\hat{\sigma}^x \alpha} \hat{\sigma}^z \omega_0\right] b_n = \hat{\sigma}^z t\Big(b_{n+1} + b_{n-1}\Big), \tag{3.45}$$

where we have defined the coefficients $b_n \equiv e^{i\hat{\sigma}^x \alpha(n+\frac{1}{2})} b'_n$. Here, $\omega_0 = \frac{\cos\Phi}{\sin\Phi}$ stands for the energy of the single-impurity levels and $t = -\frac{e^{-a/\xi}}{\sin\Phi}$ is the hopping amplitude. Note that the hopping amplitude is energy dependent through the energy-dependent superconducting coherence length, ξ, defined below Eq. (3.31). After this redefinition of the coefficients, Eq. (3.45) reduces to the typical tight-binding system of identical equations, whose solution reads $b_n = be^{ikna}$ and $\omega = \pm\sqrt{\omega_0^2 \sin^2\alpha + (\omega_0 \cos\alpha + 2t\cos ka)^2}$. Here k is the Bloch momentum, and the spinors b, are obtained from Eq. (3.45). The Andreev bands are defined by

$$\frac{\epsilon}{\Delta} = \pm\sqrt{\frac{\omega_0^2 \sin^2\alpha + (\omega_0\cos\alpha + 2t\cos ka)^2}{1 + \omega_0^2\sin^2\alpha + (\omega_0\cos\alpha + 2t\cos ka)^2}}, \tag{3.46}$$

where t has to be evaluated at the energy of the single-impurity level ω_0. In Fig. 3.7b and 3.7c we show the subgap spectrum of ACs with different values of Φ and α. At $\Phi = 0$, no bound states appear, and hence there are no Andreev bands. Increasing Φ, a pair of bands emerge from the coherent peaks and start moving towards the Fermi level, up to a point around $\Phi = \pi/2$ where they touch each other, forming a gapless phase. Further increase of Φ leads to a gap reopening with inverted Andreev bands. The latter merge with the continuum spectrum at $\Phi = \pi$. Interestingly, the bands' inversion also happens when they merge into the continuum and reenter the superconducting gap at $\Phi = l\pi$, where l is an integer. Consequently, the spectrum of these ACs is π periodic in Φ.

---

[4] Because we do not include any spin-orbit interaction in our analysis any other planar rotation choice will give equivalent results.

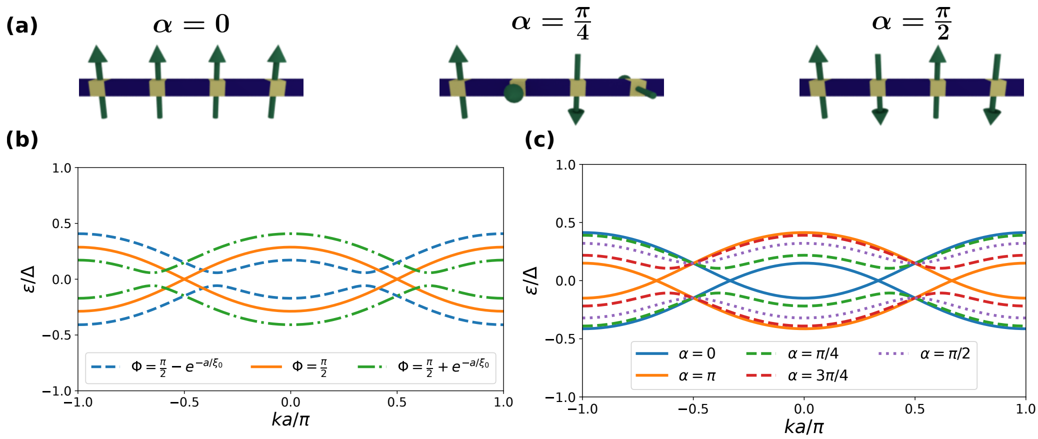

Figure 3.7: (a) Sketches of magnetic configurations in ACs for different values of α. (b) Andreev bands for $\alpha = \frac{\pi}{4}$ and different values of Φ. (c) Andreev bands for $\Phi = \frac{\pi}{2} - e^{-a/\xi_0}$ and different values of α. In both panels, we assumed a separation between impurities of $a = 2\xi_0$.

As can be seen from the energy spectrum of the bands, Eq. (3.46), the gap closes only at half-integer values of $\Phi/2$ forming a Dirac point at $ka = \pi/2$ in ACs with any value of α except in those where $\sin\alpha = 0$. This situation corresponds to ferromagnetic ACs, where each of the Andreev bands corresponds to opposite spin species, and hence they do not interact while crossing. To study what happens in the gap closing events in more detail, one can linearize the eigenvalue problem, Eq. (3.45), around the Dirac point in the k-space in the vicinity of the critical values, $\Phi = (l + \frac{1}{2})\pi$, where l is an integer, which after a $-\pi/4$ rotation around the x-spin-axis[5] reads

$$\begin{pmatrix} \omega + \omega_0 \sin\alpha & i\omega_0 \cos\alpha + 2itka \\ -i\omega_0 \cos\alpha - 2itka & \omega - \omega_0 \sin\alpha \end{pmatrix} \begin{pmatrix} \tilde{b}_\uparrow \\ \tilde{b}_\downarrow \end{pmatrix} = 0. \tag{3.47}$$

For $\cos\alpha = 0$ (*i.e.*, antiferromagnetic ordering of the magnetic impurities) equation (3.47) has the form of a Dirac Hamiltonian with ω_0 playing the role of the mass [111]. For any other value of α, the role of the mass is played by $\omega_0 \sin\alpha$ and the term $\omega_0 \cos\alpha$ in Eq. (3.47) is a gauge field that arises from the local transformation of the b_n coefficients described below Eq. (3.45). The closing and reopening of the gap is associated with a sign change of the mass term (gap inversion). Interestingly, the gap can also get inverted without closing: at values of $\Phi = l\pi$ the Andreev bands merge into the continuum of the spectrum and

---

[5] A matrix $\hat{M}$ in spin space is rotated an angle γ around an axis given by the unit vector $\mathbf{n}$ by the transformation $\hat{\hat{M}} = e^{-i\gamma n^a \hat{\sigma}^a} \hat{M} e^{i\gamma n^a \hat{\sigma}^a}$

reenter in the superconducting gap in inverted order [94].

Various realizations of an inhomogeneous Dirac model with the mass inversion have been widely studied in quantum field theory and condensed matter physics [187, 188, 189, 190, 191, 171, 192]. The most striking features of this model are the presence of bound states at the interface where the mass-inversion takes place and the fractionalization of the interface charge. It becomes interesting, then, to study if those bound states exist in junctions between different ACs with inverted gaps for arbitrary values of α. To do so, we consider a junction between two different chains where the rotation parameter between the impurities remains constant, α, but their magnetic phases change from the AC on the left, Φ_L, to the one on the right Φ_R. The tight-binding equations of such a system read

$$\left[\omega - e^{i\hat{\sigma}_1\alpha}\hat{\sigma}_3\omega_{0n}\right] b_n = \hat{\sigma}_3 t_{n+1} b_{n+1} + \hat{\sigma}_3 t_n b_{n-1}, \tag{3.48}$$

where ω_{0n} and t_n are defined below Eq. (3.35). The magnetic phase is Φ_L for $n < 0$ and Φ_R for $n \geq 0$. We can write for the left and right ACs, $b_n = b_{L+}e^{-iq_{L+}n} + b_{L-}e^{-i\mu_L q_{L-}n}$ and $b_n = b_{R+}e^{i\mu_R q_{R+}n} + b_{R-}e^{i\mu_R q_{R-}n}$, respectively, where $q_{L(R)\pm}$ is determined by the solution of the eigenvalue equation, Eq. (3.48), with positive imaginary part:

$$\cos q_{L(R)\pm} = \frac{-\omega_{0L(R)}\cos\alpha \pm i\sqrt{\omega_{0L(R)}^2 \sin^2\alpha - \omega^2}}{2t_{L(R)}}. \tag{3.49}$$

According to this expression, bound states can only appear at energies with $\omega^2 < \omega_{0L(R)}^2 \sin^2\alpha$, *i.e.*, at energies within the gap formed by the Andreev bands of both ACs [*c.f* Eq. (3.46)]. The corresponding eigenvectors are given by

$$b_{L(R)\pm} = \begin{pmatrix} 1 \\ ie^{\pm i\gamma_{L(R)}} \end{pmatrix}, \tag{3.50}$$

where

$$e^{\pm i\gamma_{L(R)}} = \frac{-\omega \pm i\sqrt{\omega_{0L(R)}^2 \sin^2\alpha - \omega^2}}{\omega_{0L(R)}\sin\alpha}. \tag{3.51}$$

From the above results we find that bound states exist for those energies satisfying following determinant equation:

$$\begin{vmatrix} t_L & t_L & t_R & t_R \\ t_L e^{i\gamma_L} & t_L e^{-i\gamma_L} & t_R e^{i\gamma_R} & t_R e^{-i\gamma_R} \\ e^{iq_{L+}} & e^{iq_{L-}} & e^{-iq_{R+}} & e^{-iq_{R-}} \\ e^{iq_{L+}}e^{i\gamma_L} & e^{iq_{L-}}e^{-i\gamma_L} & e^{-iq_{R+}}e^{i\gamma_R} & e^{-iq_{R-}}e^{-i\gamma_R} \end{vmatrix} = 0. \tag{3.52}$$

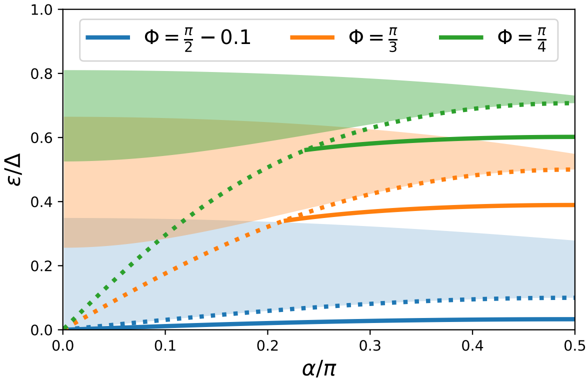

Figure 3.8: Energy of the (solid line) positive-energy interfacial state in terms of α in anti-symmetric junctions between helical ACs with $\Phi \equiv \Phi_R = -\Phi_L$. Different colors correspond to different strengths of the impurities, Φ, whereas their separation all along the junction is fixed to $a = 2\xi_0$. The shaded areas indicate the position of the (positive-energy) Andreev band in the respective infinite chains [Eq. (3.46)] and the dotted lines show the energy values with $\omega^2 = \omega_0^2 \sin^2 \alpha$. This value determines the maximum possible energy of the bound state [Eq. (3.51)].

One can check that this equation has solutions only when $sign(\omega_{0L}) = -sign(\omega_{0R})$. Therefore, the bound states can only appear in junctions between ACs with inverted gaps. This is a necessary but not sufficient condition. Namely, the presence of the interfacial state in inverted junctions depends on the magnetic rotation along the crystal described by α: whereas for antiferromagnetic alignment of the impurities ($\cos \alpha = 0$) the interfacial state appears in any inverted junction, for ferromagnetic ACs ($\sin \alpha = 0$) it never does. For any other value of α, the existence of the bound state depends on Φ_L and Φ_R as explained below.

The determinant equation, Eq. (3.52), can be reduced to a compact equation in the *anti-symmetric* configuration with $\Phi_R = -\Phi_L$. In this situation we can define $\gamma \equiv \gamma_L = \gamma_R$ and $q_{L\pm} = q_{R\mp} \equiv \pm\kappa + i\lambda$, where κ and λ are real numbers determined by Eq.(3.49). For $\lambda > 0$, the condition for the existence of the bound state reads

$$\sin^2 \gamma \cosh^2 \lambda - \sin^2 \kappa = 0. \tag{3.53}$$

In Fig. 3.8, we show the dependence of the positive energy bound states with α in anti-symmetric inverted junctions of ACs with fixed value of $a = 2\xi_0$ and different strengths of the magnetic impurities, $\Phi \equiv \Phi_R = -\Phi_L$. With shaded areas, we show the energies within the positive-energy Andreev band is situated in the infinite AC [Eq. (3.46)]. The dotted lines correspond to energy values for which

$\omega^2 = \omega_0^2 \sin^2 \alpha$ and they indicate the maximum possible energy of a bound state [Eq. (3.51)]. Close to the gap-closing point, $\cos \Phi \ll 1$, the interfacial states are present at any value of α, excluding ferromagnetic ordering of the impurities, $\sin \alpha = 0$. As the size of the gap between the Andreev bands increases, the range of α values for which the pair of bound states exist shrinks around those values corresponding to an antiferromagnetic ordering of the magnetic impurities, $\cos \alpha = 0$.

The existence or not of the bound state in anti-symmetric junctions of ACs can be understood from the relative position of the maximum-energy condition for the bound state (the dotted lines in Fig. 3.8) and the positive-energy solution of Eq. (3.53). When $\cos \alpha \approx 0$, the maximum-energy condition locates very close to the bottom of the Andreev band and, consequently, the ω value that solves Eq. (3.53) almost always fulfills that $\omega^2 < \omega_0^2 \sin^2 \alpha$. When $\sin \alpha \approx 0$, by contrast, the dotted lines in Fig. 3.8 approach the center of the gap, $\omega = 0$. Thus, the solution to Eq. (3.53) only meets the bound state existence condition, $\omega^2 < \omega_0^2 \sin^2 \alpha$, when the borders of the gap are also very close to the Fermi energy, *i.e.*, when $\cos \Phi \approx 0$. These considerations are also applicable in general junctions between helical ACs, in which case the energy of the bound state solves Eq. (3.52) and its existence condition is given by $\omega^2 < \min(\omega_{0L}^2, \omega_{0R}^2) \sin^2 \alpha$.

To summarize, for a given value of the rotation angle α we can classify ACs in two groups depending on whether an interfacial state appears upon the formation of a junction between two chains with inverted gaps. These two groups are best exemplified by (anti-)ferromagnetic ACs inverted junctions in which interfacial bound states (always) never appear. In subsequent sections we will focus on these two type of junctions and study in more detail their spatial properties.

3.3.2.1 Fractionalization of the surface spin polarization in junctions between antiferromagnetic ACs

Previous works on one dimensional inhomogeneous Dirac systems with spatial mass inversion showed fractionalization of the charge bounded to the interface where the inversion takes place [187, 188, 189, 190, 191, 171, 192]. In this section, we show that such effect has its analogy in inverted junctions between ACs with collinear magnetization of the impurities (such that the spin along that axis is conserved) in the form of a fractionalization of the surface spin polarization. In particular, we focus on junctions between antiferromagnetic ACs because they are the simplest study case that shows states bounded to the interface.

To calculate the spin induced at the contact between the two semi-infinite an-

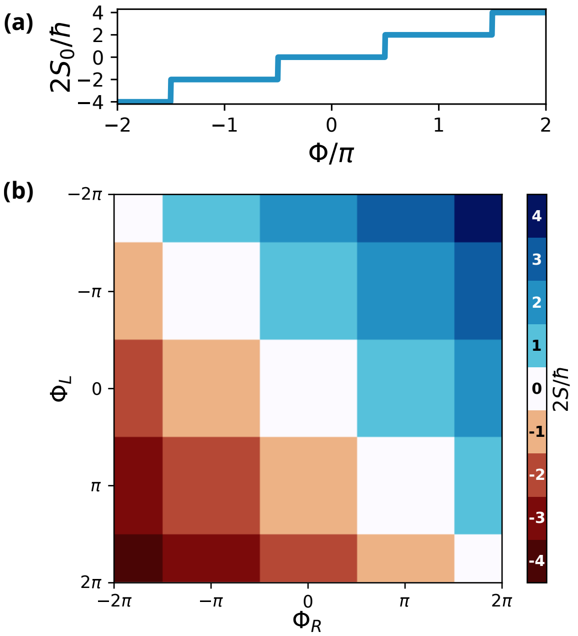

Figure 3.9: (a) Total spin polarization of the single-impurity system in terms of Φ. (b) Spin polarization of the junction between two antiferromagnetic Andreev chains as a function of Φ_L and Φ_R. It is calculated from Eq. (3.54), with $S_0(\Phi_{L(R)})$ from panel (a).

tiferromagnetic ACs, S^z, we average over all possible terminations of the chains. This is equivalent to the the so-called *sliding window average* method (see for example section 4.5 of Ref. [193]), used to compute the surface charge density by averaging over all possible unit cell choices. The calculation is specially simple in the limit when the single-impurity Andreev states are decoupled from each other, $e^{-a/\xi} \ll 1$. In Sec. 3.2, we showed that the spin polarization of a single semiclassical magnetic impurity of magnetic phase Φ in a quasi-1D superconducting wire is $2S_0^z(\Phi)/\hbar = 2\left[\left(\Phi+\frac{\pi}{2}\right) \bmod \pi\right]$, where "mod" stands for the modulo operation and accounts for a jump by two electronic spins every time the single-impurity levels cross the Fermi energy [94]. In Fig. 3.9a we show the staircase shape of $S_0^z(\Phi)$ in terms of the magnetic phase for a single semiclassical impurity. We now consider the junction between the two antiferromagnetic ACs. It has four possible ending configurations: whether both chains have the same number of up and down magnetic impurities, the right (left) Andreev chain has an extra up (down) magnetic region or both chains are unbalanced. Consequently, the total spin polarization of the junction, calculated from the average over the four possible configurations, reads

$$S^z = \frac{S_0^z(\Phi_R) - S_0^z(\Phi_L)}{2}. \tag{3.54}$$

Starting from the uncoupled impurities, if one adiabatically switches on the coupling, the Andreev bands start widening. However, in the considered configuration the gap never closes and, as we discussed after Eq. (3.11), the spin cannot change and is hence given by Eq. (3.54). In Fig. 3.9b, we show the total spin of the junction in terms of Φ_L and Φ_R. Interestingly, the spin polarization can now be equal to and odd integer times the electronic unit, in contrast to the always even value of $S_0(\Phi)$. By construction, the half-integer spin (per Fermi valley) is localized at the junction between ACs. In other words, there is a fractionalization of the interface spin. Such fractionalization is a local effect. In a finite system, the contribution from the edges will always lead to a total integer spin per Fermi valley. Notice that changes on the spin polarization of ACs is determined by the change of the spectral asymmetry index, Eq. (3.11), and hence Eq. (3.54) is valid beyond the nearest neighbors tight-binding approximation. This is indeed confirmed by the exact numerical solution of Eq. (3.29) that we explore in Sec. 3.3.3 [112].

3.3.3 Collinear Andreev Crystals

In this section we extend the study of (anti-)ferromagnetic ACs beyond the first-neighbor tight-binding approximation used in previous sections. To do so, we solve the Eilenberger equation to obtain the quasiclassical GFs, $\check{g}(x)$, following the procedure discussed in Sec. 3.3.1.2. From the knowledge of $\check{g}(x)$ we can obtain the local density of states and magnetization of ACs and junctions.

Specifically, we consider chains of magnetic impurities located at $X_n = na$, with an arbitrary separation between the impurities a. Here n is an integer. We assume that all magnetizations, and hence the exchange fields, are aligned along the z axis. Because of the collinear alignment of the exchange field we can treat the two spin degrees of freedom separately, $\sigma = \pm$, thus reducing the size of the GFs involved from 4 × 4 (in Nambu×spin space) to 2 × 2 matrices in Nambu space. It follows from Eq. (3.37) and the normalization condition, $[\check{g}(x)]^2 = 1$, that within the region between two subsequent impurities, $X_n < x < X_{n+1}$, the quasiclassical GF for a single spin projection, σ, can be written in terms of two independent constants, $b_{\sigma n}$ and $c_{\sigma n}$:

$$\hat{g}_\sigma(x) = \sqrt{1 - e^{-2a/\xi} b_{\sigma n} c_{\sigma n}}\, \hat{g}^0 + b_{\sigma n} e^{2(x-X_{n+1})/\xi} \left|+\right\rangle \left\langle \tilde{-}\right| + c_{\sigma n} e^{-2(x-X_n)/\xi} \left|-\right\rangle \left\langle \tilde{+}\right| . \tag{3.55}$$

Here $\hat{g}^0 \equiv \hat{P}_+ - \hat{P}_- = \frac{\Delta\hat{\tau}_2 + i\epsilon\hat{\tau}_3}{\sqrt{\Delta^2-\epsilon^2}}$ is the GF of an homogeneous BCS superconductor. Equation (3.55) is the representation of the GF in the basis where the BCS propagator, Eq. (3.38), is diagonal.

According to Eq. (3.40), the GFs at the left and right side of the n-th impurity are connected by the boundary condition

$$\hat{g}_\sigma(X_n^R) = e^{i\sigma\hat{\tau}_3\Phi_n}\hat{g}_\sigma(X_n^L)e^{-i\sigma\hat{\tau}_3\Phi_n}, \tag{3.56}$$

where the direction to which the exchange field is pointing along the quantization axis is determined by the sign of the magnetic phase, Φ_n. Ferromagnetic ACs are described by a sequence of identical magnetic impurities with associated magnetic phases of $\Phi_n = \Phi$, whereas in antiferromagnetic ACs $\Phi_n = (-1)^n\Phi$. In the next sections we study these two types of ACs and junctions between them.

3.3.3.1 Ferromagnetic ACs

In a ferromagnetic AC the unit cell contains a single magnetic impurity, so the σ-spin projection of the *chain propagator*, Eq (3.41), reads

$$\hat{S}_{F\sigma} \equiv \hat{u}(a)e^{i\sigma\hat{\tau}_3\Phi}\ . \tag{3.57}$$

Here $\hat{u}(a)$ is the BCS propagator given in Eq. (3.38). The operator $\hat{S}_{F\sigma}$ describes the propagation of the quasiclassical GF from the left side of impurity n to the left side of impurity $n+1$, $\hat{g}_\sigma(X_{n+1}^L) = \hat{S}_{F\sigma}g_\sigma(X_n^L)\hat{S}_{F\sigma}^{-1}$.

To determine the quasiclassical GF, we need to obtain the parameters b and c in Eq. (3.55). The periodicity of $\hat{g}_\sigma$ over the unit cell, leads to $b_{\sigma n} = b_\sigma$ and $c_{\sigma n} = c_\sigma$. These expressions together with $\hat{S}_{F\sigma}\hat{g}(X_n^L)\hat{S}_{F\sigma}^{-1} = \hat{g}(X_n^L)$ result in

$$b_\sigma = c_\sigma = \frac{2e^{\frac{a}{\xi}}\,\langle\tilde{+}|\,e^{i\sigma\hat{\tau}_3\Phi}\,|-\rangle}{\sqrt{\left(e^{\frac{a}{\xi}}\,\langle\tilde{+}|\,e^{i\sigma\hat{\tau}_3\Phi}\,|+\rangle + e^{-\frac{a}{\xi}}\,\langle\tilde{-}|\,e^{i\sigma\hat{\tau}_3\Phi}\,|-\rangle\right)^2 - 4}}\ . \tag{3.58}$$

After substitution of these values in Eq. (3.55) one obtains the quasiclassical GF in the magnetic regions all along the chain and, with it, the local density of states (LDOS) and the local spin density [Eqs. (3.42) and (3.43), respectively].

In Fig. 3.10, we show the LDOS for a single spin species of different ferromagnetic ACs, $\nu_\uparrow(\epsilon)$. The LDOS for the opposite spin projection can be obtained from the relation $\nu_\downarrow(\epsilon) = \nu_\uparrow(-\epsilon)$. The different panels in Fig. 3.10 correspond to different values of separation and strength of the magnetic impurities, a and Φ, respectively. Within the superconducting gap, $|\epsilon| < |\Delta|$, the position of the Andreev band depends on Φ and its width increases by decreasing a. For energies

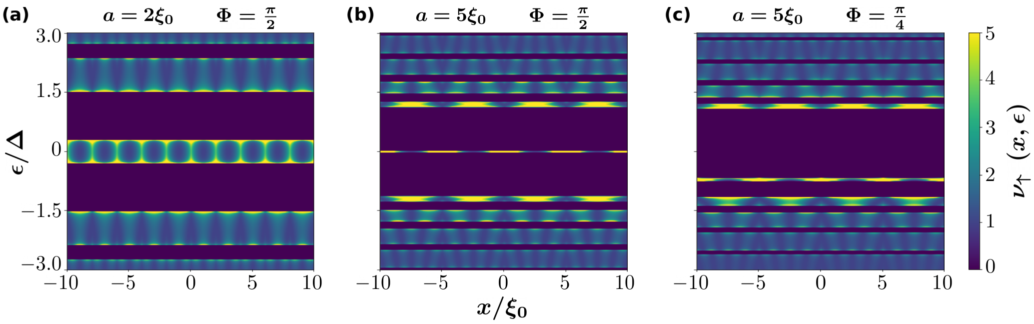

Figure 3.10: Local density of states, $\nu_\uparrow$, of spin-up electrons in ferromagnetic ACs with different separation between and strengths of the magnetic impurities, a and Φ, respectively (see the title above each panel). A spin-polarized Andreev band, whose width increases with decreasing a, moves from the lower edge of the superconducting gap to the top one with increasing value of Φ, crossing zero energy around $\sin\Phi = 0$ values. The LDOS of spin-down quasiparticles fulfills the relation $\nu_\downarrow(\epsilon) = \nu_\uparrow(-\epsilon)$.

larger than Δ the continuum gets split by small gaps whose widths depend on Φ, a and the energy at which they lay. The origin of the gaps lay on the lifting of degeneracies between electronic states that differ by the reciprocal lattice vector in periodic crystals, studied in many textbooks [194, 117, 15]. At integer values of Φ/π, the small gaps at the continuum close, whereas their width is maximum for half-integer values of Φ/π. In the same way as it happens with the Andreev band, the width of these small gaps increases with decreasing a. The size of the gaps reduces by increasing the energy with respect to the Fermi level.

3.3.3.2 Antiferromagnetic ACs

In antiferromagnetic ACs the unit cell contains two identical magnetic impurities pointing in opposite directions. The *chain propagator* [Eq. (3.41)] that describes the evolution of the GF from the left interface of one magnetic impurity to the left interface of the equivalent impurity in the next unit cell reads,

$$\hat{S}_{A\sigma} \equiv \hat{u}(a)e^{-i\sigma\hat{\tau}_3\Phi}\hat{u}(a)e^{i\sigma\hat{\tau}_3\Phi}. \tag{3.59}$$

The unit cell consists now of two superconducting regions with two different sets of independent parameters, namely, $b_{\sigma 0} = b_{\sigma(2n)}$, $c_{\sigma 0} = c_{\sigma(2n)}$ and $b_{\sigma 1} = b_{\sigma(2n+1)}$, $c_{\sigma 1} = c_{\sigma(2n+1)}$. Here n is the impurity index. The boundary condition for the impurity located between these two superconducting sections, Eq. (3.56),

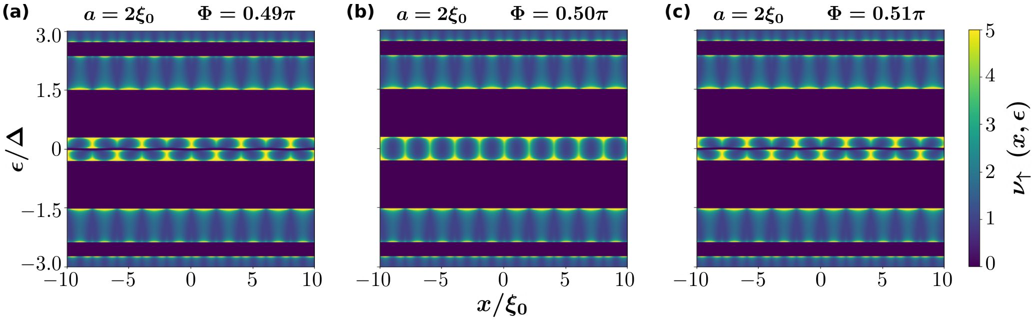

Figure 3.11: Local density of states, $\nu_\uparrow$, of spin-up electrons in an antiferromagnetic AC close to the gap closing event, $\cos\Phi \ll 1$. The separation between impurities is $a = 2\xi_0$. Different panels correspond to different values of Φ. The gap between the Andreev bands closes only at values of $\cos\Phi = 0$.

leads to the following relation between the set of parameters:

$$b_{\sigma 1} = c_{\sigma 0}, \tag{3.60}$$

$$c_{\sigma 1} = b_{\sigma 0}. \tag{3.61}$$

Additionally, from the periodicity of the GF, $\hat{S}_{A\sigma}\hat{g}_\sigma(X^L_{2n})\hat{S}^{-1}_{A\sigma} = \hat{g}_\sigma(X^L_{2n})$, we obtain the expressions for

$$b_{\sigma 0} = \langle \tilde{-}|\, e^{i\sigma\hat{\tau}_3\Phi}\, |-\rangle\, \mathcal{D}_\sigma, \tag{3.62}$$

$$c_{\sigma 0} = -\langle \tilde{+}|\, e^{i\sigma\hat{\tau}_3\Phi}\, |+\rangle\, \mathcal{D}_\sigma, \tag{3.63}$$

where

$$\mathcal{D}_\sigma \equiv \frac{e^{\frac{a}{\xi}} \langle \tilde{+}|\, e^{i\sigma\hat{\tau}_3\Phi}\, |-\rangle}{\sqrt{\langle \tilde{+}|\, e^{i\sigma\hat{\tau}_3\Phi}\, |+\rangle \langle \tilde{-}|\, e^{i\sigma\hat{\tau}_3\Phi}\, |-\rangle + \left(\langle \tilde{+}|\, e^{i\sigma\hat{\tau}_3\Phi}\, |+\rangle \langle \tilde{-}|\, e^{i\sigma\hat{\tau}_3\Phi}\, |-\rangle \sinh\frac{a}{\xi}\right)^2}}. \tag{3.64}$$

Substitution of these expressions into Eq. (3.55) determines the quasiclassical GF. From it we obtain the LDOS for a single spin specie shown in Fig. 3.11 for different values of Φ around the gap closing point, $\Phi = \pi/2$. The separation between impurities is set to $a = 2\xi_0$. For energies within the superconducting gap a pair of Andreev bands appear at symmetric energy ranges with respect to the Fermi level. As it was predicted in previous calculations under the first-neighbor tight-binding approximation (Ref. [111] and Sec. 3.3.2), these two bands touch each other only at half-integer values of Φ/π closing the gap around the Fermi level (see Fig. 3.11). Moreover, the Andreev bands touch the continuum only when Φ/π is an integer: situations where the LDOS of the antiferromagnetic AC coincides with that of a pristine superconductor because the phase difference obtained by electrons and holes after propagation across an impurity is a multiple of 2π. Within the Andreev bands, the LDOS is larger around the position of the magnetic impurities and around the energies of the single-impurity level. For energies larger than the superconducting gap, $|\epsilon| > |\Delta|$, we observe an interference pattern and the splitting of the continuum due to the opening of small gaps. The dependence of the width of the small gaps on Φ, a, and ϵ is the same as the one observed in ferromagnetic ACs (see the last paragraph of Sec. 3.3.3.1).

3.3.3.3 Junctions of collinear ACs

As discussed in Sec. 3.3.2, inverted junctions of antiferromagnetic ACs host a pair of states bounded to the interface. Moreover, inverted junctions of antiferromagnetic ACs may present fractionalization of the surface spin polarization per Fermi valley[111]. In this section we show that this result holds beyond the tight-binding approximation used above, by solving the Eilenberger equation in junctions of ACs. Although we focus our analysis on junctions between antiferromagnetic ACs, the mathematical procedure presented here is general and it can be applied to obtain the quasiclassical GFs in junctions between any type of collinear ACs.

We start by defining the σ-spin projection of the *chain propagators* of the left (right) ACs, $\hat{S}_{L(R)\sigma}$, as the operator that propagates the GFs through a unit cell of the crystal, Eq. (3.41). The *chain propagator* is given by Eq. (3.57) in ferromagnetic and by Eq. (3.59) in antiferromagnetic ACs. Solving the eigenvalue problem of these operators we find a set of vectors for which the chain propagator is diagonal,

$$\hat{S}_{L(R)\sigma} \, |\lambda^{\pm}_{L(R)\sigma}\rangle = e^{\pm\lambda_{L(R)\sigma}} \, |\lambda^{\pm}_{L(R)\sigma}\rangle \, . \tag{3.65}$$

Because $\hat{S}_{L(R)\sigma}$ is, in general, not Hermitian, the left eigenvectors that form the co-basis

$$\langle\tilde{\lambda}^{\pm}_{L(R)\sigma}| \, \hat{S}_{L(R)\sigma} = e^{\pm\lambda_{L(R)\sigma}} \, \langle\tilde{\lambda}^{\pm}_{L(R)\sigma}| \, , \tag{3.66}$$

are not related by Hermitian conjugation to the right-eigenvectors of Eq. (3.65). The eigenvectors can be represented as exponentials with arguments of opposite sign because $\det(\hat{S}_{L(R)\sigma}) = 1$. In ferromagnetic and antiferromagnetic ACs λ_σ is purely imaginary (real) for energies where the infinite chain's spectrum shows (does not show) states. Similarly to the description of the propagation within

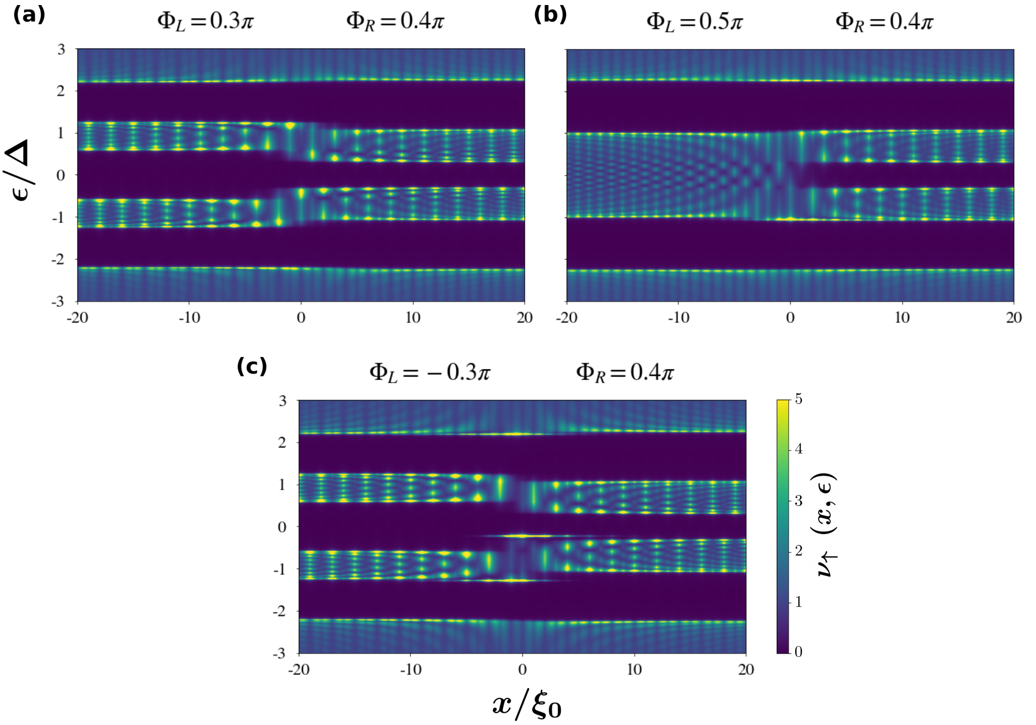

Figure 3.12: Local density of states of spin-up electrons, $\nu_\uparrow(x,\epsilon)$, in a junction between two different antiferromagnetic ACs. Inversion of the gap across the junction leads to the appearance of states bounded to the interface at every gap in the spectrum. These states move from one edge of the gap to the opposite one with increasing Φ_L. The closer the energy of the states are to the gap edge of one chain, the more they penetrate into that chain.

the superconducting region between two subsequent impurities, Eq. (3.37), the propagation of the spin-polarized GFs through the reference points of different unit cells reads

$$\hat{g}_\sigma(ml) = \sqrt{1 - v_{s\sigma} w_{s\sigma}} \Big(|\lambda^+_{s\sigma}\rangle \langle \tilde{\lambda}^+_{s\sigma}| - |\lambda^-_{s\sigma}\rangle \langle \tilde{\lambda}^-_{s\sigma}| \Big) + v_{s\sigma} e^{2\lambda_{s\sigma} m} |\lambda^+_{s\sigma}\rangle \langle \tilde{\lambda}^-_{s\sigma}| + w_{s\sigma} e^{-2\lambda_{s\sigma} m} |\lambda^-_{s\sigma}\rangle \langle \tilde{\lambda}^+_{s\sigma}| \,. \tag{3.67}$$

Here, the s index is substituted by L and R on the left and right ACs, respectively, l is the length of the unit cell, m is the unit cell index and we set the reference point inside the unit cell to $x_0 = 0$. The square root multiplying the first term on the r.h.s. of Eq. (3.67) comes from the normalization condition of the GF and the substraction of projectors that it multiplies corresponds to the quasiclassical GF of the infinite AC at the left interface of the reference impurity.

Equation (3.67) provides the quasiclassical GFs for a single spin, σ, at the reference points of each unit cell in terms of four parameters (two parameters per side of the junction): $v_{s\sigma}$ and $w_{s\sigma}$. Commensurability of $\check{g}(x)$ at $x \longrightarrow \pm\infty$ requires that at each side of the junction one of these parameters has to be zero. Which one of the parameters is set to zero depends on the sign of $\lambda_{s\sigma}$: for $s = L$ ($s = R$) we set $w_{s\sigma} = 0$ ($v_{s\sigma} = 0$) when $\lambda_{s\sigma} > 0$, whereas we set $v_{s\sigma} = 0$ ($w_{s\sigma} = 0$) otherwise. The value of the remaining two parameters is obtained from the continuity of the quasiclassical GFs through the junction. Having obtained the four parameters we next propagate $\hat{g}_\sigma(ml)$ according to Eqs. (3.37) and (3.40) to obtain the quasiclassical GFs in any position of the chain, x. This method leads to analytic expressions of the quasiclassical GFs for any junction configuration. In particular, in Appendix A we apply this method in junctions between antiferromagnetic ACs and obtain the analytic expression of the quasiclassical GF, $\check{g}(x)$ [Eqs. (A.11)–(A.20)].

In Fig. 3.12, we show the obtained LDOS for a single spin species around the interface between two antiferromagnetic ACs for different values of Φ_L and fixed values of $\Phi_R = 0.4\pi$ and $a = \xi_0$. The left panel of Fig. 3.12 shows the situation where the function of the energy of the single-impurity Andreev states, ω_0, has the same sign at both sides of the junction. The spectrum exhibits a transition area around the interface where the size of the gap between the Andreev bands changes, but no bound states appear. When $\Phi_L = \pi/2$ (middle panel of Fig. 3.12), the gap on the left side of the junction closes, whereas the gap on the right remains open. Further increasing of Φ_L leads to a reopening of the left gap, as shown on the right panel of Fig. 3.12. One can clearly see how spin-polarized bound states appear around the interface as a consequence of the gap inversion. Interestingly, these bound states are not restricted to the gap between the low-energy Andreev bands, but appear inside all gaps in the spectrum, indicating that the inversion of the central gap carry the inversion of all the remaining gaps.

From the quasiclassical GF of the junction, we can also compute the spin of the system by integrating Eq. (3.43) over x. We consider the zero-temperature case. As it is well know, quasiclassical GFs only describe the physics close to the Fermi surface and, hence, to obtain the total spin density one has to add the Pauli paramagnetic term [117, 195]. Namely, the Pauli paramagnetic contribution of each magnetic impurity is given by Φ/π in units of $\hbar/2$ [94]. The resulting total value depends on the way the ACs terminate. As we are dealing with an infinite system, it is calculated from the average over all possible ending configurations of the chains (see the discussion in Sec. 3.3.2.1). This is equivalent to the so-called *sliding window average* method (see, for example, Sec. 4.5 of Ref. [193]) and it results in a Pauli paramagnetic contribution of $\frac{\Phi_L - \Phi_R}{2\pi}$ that has to be added

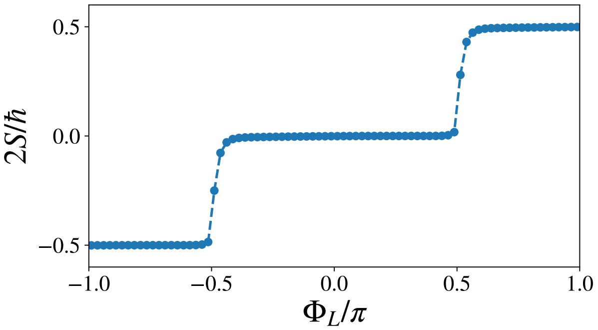

Figure 3.13: Contribution of a single Fermi valley to the surface spin polarization at $T = 0$ of a junction between antiferromagnetic ACs in terms of Φ_L for fixed values of $\Phi_R = 0.4\pi$ and $a = \xi_0$. The transition between plateaus is rounded due to the Dynes parameter, $\Gamma = 10^{-3}\Delta$, used to avoid numerical convergence problems.

to the integrated magnetization density of Eq. (3.43).

In Fig. 3.13, we show the contribution of a single Fermi valley (See Fig. 3.1) to the surface spin polarization at $T = 0$ of a junction between two antiferromagnetic ACs as a function of Φ_L. We set $a = 0.1\xi_0$ and $\Phi_R = 0.4\pi$, although any other value of a and $-\pi/2 < \Phi_R < \pi/2$ give the same results, as long as the separation between the impurities is large enough such that the regions in-between remain in the superconducting phase. The magnetization per Fermi valley can only take half-integer values of the electronic spin, which indicates fractionalization of the surface spin per electron-hole valley. The contribution from both Fermi valleys are equal and, hence, the total surface magnetization equals to an integer value of $\hbar/2$. Choice of Φ_R outside the range $-\pi/2 < \Phi_R < \pi/2$ would shift the ladder-like curve in Fig. 3.13 some steps up or down due to the Pauli paramagnetic contribution (see previous paragraph). Finding the value of a below which superconductivity breaks down would require self-consistent calculation of Δ. However, we can make an upper-bound estimation of the critical value of a by demanding that the mean value of the exchange field along the wire does not exceed the value of Δ. In ferromagnetic ACs this condition requires that $a > \xi_0$, whereas in antiferromagnetic ACs the exchange field averages to zero and superconductivity may survive even at $a < \xi_0$. In Fig. 3.13, the smooth transition between plateaus is a consequence of the small imaginary positive number that we add to the energy, $\epsilon + i\Gamma$, with $\Gamma = 10^{-3}\Delta$, in order to avoid numerical problems. Γ is known as Dynes parameter [145] and models the effect of inelastic scattering which leads to a broadening of the coherent peaks peaks in the spectrum. In absence of inelastic processes, $\Gamma = 0$ and the magnetization shows sharp steps.

The surface spin polarization per electron-hole valley, calculated from the quasiclassical GFs and shown in Fig. 3.13, verifies the result that we obtained in Sec. 3.3.2.1 using the tight-binding up to first-neighbor calculation and the connection between the spin polarization and the spectral asymmetry index in gapped systems that we discuss in Sec. 3.1.2. Therefore, Fig. 3.9b gives the correct value of the spin polarization in junctions between antiferromagnetic ACs.

Chapter 4

S/FI hybrid systems: Fundamentals and applications

Superconducting films with spin-split density of states have been used for a long time to determine the spin polarization of ferromagnetic metals tunnel-coupled to the superconductor (S) [41, 42, 196, 44, 45, 46, 40]. Originally, the spin splitting was induced by applying in-plane magnetic fields to thin superconducting films. These fields had to be large, of the order of few Tesla, in order to obtain sizable splittings. Interestingly, as shown in the late 1980s, such spin splitting can also be observed at rather small, or even zero, magnetic fields in superconducting Al layers adjacent to ferromagnetic insulators (FIs) [197, 39]. In this case the splitting is attributed to the exchange interaction at the FI/S interface [37]. Additionally, those first works on FI/S structures showed that thin FI layers can also be used as very efficient spin-filters, with potential application as sources for highly spin-polarized spin currents [198].

More recently, non-equilibrium properties of superconductors with a spin-split density of states have attracted a renewed attention [199, 200, 51, 201, 202, 31, 32]. In such systems, two additional spin-dependent modes appear and couple to the widely studied non-equilibrium energy and charge modes [202, 203]. FI/S structures have also been suggested for several applications, such as highly efficient thermoelectric elements [48, 54], bolometers [52], thermometers [50], cryogenic RAM memories [53], and different caloritronic devices to access the electronic heat current in nanostructures [55, 56, 49, 57, 58]. Most of these applications require both superconductors with spin-split density of states and highly polarized spin-filter interfaces. This motivates the works presented in this chapter, in which we explore different devices with S/FI interfaces.

In Sec. 4.1, we develop a general model of S/FI bilayers that describes both spectral effects in the S layer and effect on the currents flowing across the FI. Our model takes into account self-consistently magnetic disorder, spin-orbit coupling, and orbital effects of the magnetic field, as well as non-collinear spin-splitting fields, and provides a tool to describe S/FI bilayers in a myriad of experiments. In Sec. 4.2, we use this model to describe the coupling of two spin-split superconductors through an additional spin-filter barrier. We predict several features in FI/S-based junctions, such as additional coherent peaks in the differential conductance when the FI layers are monodomain with non-collinear magnetization, and the possible realization of an anomalous Josephson junction at zero phase bias. At the end of the section, we use this model to successfully describe some experimental data.

In Sec. 4.3, we apply the model for the study of structures with S/FI layers to build on-chip cooling devices. Tunnel junctions between superconductors and normal metals proved to be a very efficient way to refrigerate small metallic islands below sub-Kelvin temperatures [204, 205, 206, 207, 208, 209, 210, 211, 212]. In that section we show how the addition of FIs into these type of devices systems enhance their refrigeration capabilities. We also explore other configurations where the normal metal is substituted by a superconducting material.

Finally, in Sec. 4.4 we add the flavour of spin-orbit coupling (SOC) to the S/FI structures considered so far. The interplay between the superconducting correlations, the exchange field and the SOC results into magnetoelectric effects [72, 73, 74, 75, 76, 77] with various potential applications. In particular, in this section we consider finite quasi-1D structures where this interplay leads to a difference of the superconducting phase between the ends of the wire. When plugging such a structure into a superconducting loop, a supercurrent flows along the circuit. In analogy to the usual batteries used in electronics, these devices are called *Josephson phase batteries* [63, 87, 86]. Along the section we compute the phase accumulated across phase batteries of different geometries to find the optimum setup.

4.1 Modelization of diffusive S/FI bilayers

In this section, we study the properties of diffusive superconductor (S) – ferromagnetic insulator (FI) bilayers. The effect of the FI layer on the system can be twofold. On the one hand, the spin-dependent back-scattering of conduction electrons from the S layer that hit the FI interface results in an effective exchange field in the superconductor. This field generates an spin splitting in the density of states (DOS). We study this case in Sec. 4.1.1. On the other hand, when a current is passed through the FI, the latter acts as a spin filter. We study the spin filtering effect of FI layers in Sec. 4.1.2.

4.1.1 Spectral effects: spin splitting

In this section, we introduce the spin splitting effect that a FI layer has on an adjacent superconducting thin film. We consider diffusive systems where the films are stacked along the z axis and where translation symmetry is preserved in the $x-y$ plane. We also assume that the width of the S layer is much smaller than the superconducting coherence length, $w_S \ll \xi_0$, which lets us assume that the superconducting properties of the film do not change across its width. Such films can also handle strong in-plane magnetic fields without breaking superconductivity because their small lateral dimension impairs orbital effects, letting only the paramagnetic effects harms the superconducting phase.

To model the system, we use the Green's functions defined in the Keldysh $\otimes$ Nambu $\otimes$ spin space[1], which are 8×8 matrices that satisfy the normalization condition

$$\left[\breve{g}(z)\right]^2 = 1\ . \tag{4.1}$$

In the Keldysh space they can be written as [122]:

$$\breve{g}(z) = \begin{pmatrix} \breve{g}^R(z) & \breve{g}^K(z) \\ 0 & \breve{g}^A(z) \end{pmatrix}, \tag{4.2}$$

where $\breve{g}^R$ stands for the retarded component of the GFs, and $\breve{g}^A = -\hat{\tau}_3 \breve{g}^{R^\dagger} \hat{\tau}_3$ is the advanced component. Due to the normalization condition, the Keldysh component can be written as

$$\breve{g}^K(z) = \breve{g}^R(z)\check{f} - \check{f}\breve{g}^A(z). \tag{4.3}$$

In these expressions, the "checks" $\breve{\cdot}$ indicate 8 × 8 matrices, whereas $\check{\cdot}$ are used for 4 × 4 matrices in Nambu-spin space, and $\hat{\cdot}$ for 2 × 2 matrices. $\hat{\tau}_i$ is the i-th Pauli matrix spanning Nambu space and $\hat{f}$ stands for the electron distribution function. In equilibrium, the latter is proportional to the unit matrix in Nambu and spin space and reads:

$$\check{f}(\epsilon) \equiv f_0(\epsilon, T) = \tanh\frac{\epsilon}{2k_B T}, \tag{4.4}$$

---

[1] To simplify the notation we skip throughout the text the direct product symbol, $\otimes$

where k_B is the Boltzmann's constant and T is the temperature of the system. Whenever we do not specify any matrix structure via Pauli matrices, it is implied that the matrix is proportional to the unit matrix in the corresponding space.

We now calculate the GFs in the superconducting layer, which we assume to be in thermal equilibrium. As it was indicated after Eq. (4.2) and in Eq. (4.3), we only need to compute their retarded component. In the diffusive limit, the retarded GF obeys the Usadel equation [132] [see Eq. (2.50)],

$$-D\partial_z\left(\check{g}^R\partial_z\check{g}^R\right) - \left[i\epsilon\hat{\tau}_3 - \Delta\hat{\tau}_1 - ih^a_{int}\hat{\sigma}^a\hat{\tau}_3 w_{int}\delta(z) - \check{\Sigma},\ \check{g}^R\right] = 0. \tag{4.5}$$

Here Δ stands for the superconducting order parameter, the interface is placed at $z = 0$, summation over repeated indices is implied, $\hat{\sigma}^a$ is the a-th Pauli matrix spanning spin space, h^a_{int} is the value of the a spin component of the interfacial exchange field (due to the presence of the FI film) and w_{int} is the effective thickness of the interface (*i.e.*, the effective thickness of the δ function within the quasiclassical limit) over which the exchange field is finite. In Eq. (4.5), $\check{\Sigma}$ stands for the self energy term, whose structure we discuss it later.

We can now integrate Eq. (4.5) from the lower to the top boundary of the S layer (*i.e.* from $z = 0$ to $z = w_S$, where w_S is the thickness of the superconducting layer). Regarding that the superconductor neighbours an insulating media at both $z = 0$ and $z = w_S$, we have that $\check{g}\partial_z\check{g}\big|_{z=0} = \check{g}\partial_z\check{g}\big|_{z=w_S} = 0$ as boundary conditions (see Sec. 2.4.3). When the thickness of the S layer is much smaller than the superconducting coherence length, $w_S \ll \xi_0$, the quasiclassical GF remains almost constant, $\check{g}^R(z) \approx g^R(0)$ and, therefore, the integration process is straightforward and converts Eq. (4.5) into:

$$\left[i\epsilon\hat{\tau}_3 - ih^a\hat{\sigma}^a\hat{\tau}_3 - \Delta\hat{\tau}_1 - \check{\Sigma},\ \check{g}^R\right] = 0, \tag{4.6}$$

where $\check{g}^R \equiv \check{g}^R(0)$ and we defined the effective value of the exchange field as its mean value over the S layer's thickness, $h^a \equiv h^a_{int}w_{int}/w_S$ [213]. The self-consistent superconducting order parameter, Δ, in Eq. (4.6) reads

$$\Delta = \frac{\lambda}{16i}\int_{-\Omega_D}^{\Omega_D} d\epsilon \mathrm{Tr}\left[(\tau_1 - i\tau_2)\,\check{g}^K(\epsilon)\right]. \tag{4.7}$$

Here, λ is the coupling constant and Ω_D is the Debye cutoff energy. The self energy in Eq. (4.6), $\check{\Sigma}$, consists of three contributions:

$$\check{\Sigma} = \check{\Sigma}_{so} + \check{\Sigma}_{sf} + \check{\Sigma}_{orb}, \tag{4.8}$$

namely, the spin relaxation due to spin-orbit coupling, $\check{\Sigma}_{so}$, and spin-flip[2] relaxation, $\check{\Sigma}_{sf}$, and the orbital depairing, $\check{\Sigma}_{orb}$, due to the external magnetic fields. Explicitly, each contribution within the relaxation time approximation, reads:

$$\check{\Sigma}_{so} = \frac{\hat{\sigma}^a \check{g}^R \hat{\sigma}^a}{8\tau_{so}}, \tag{4.9}$$

$$\check{\Sigma}_{sf} = \frac{\hat{\sigma}^a \hat{\tau}_3 \check{g}^R \hat{\tau}_3 \hat{\sigma}^a}{8\tau_{sf}}, \tag{4.10}$$

$$\check{\Sigma}_{orb} = \frac{\hat{\tau}_3 \check{g}^R \hat{\tau}_3}{\tau_{orb}}, \tag{4.11}$$

where τ_{so}, τ_{sf} and τ_{orb} stand for spin-orbit, spin-flip and orbital depairing relaxation times, respectively, and we sum over repeated indices.

The general solution of the Usadel equation, Eq. (4.6), is then given by the following structure in the Nambu-spin space:

$$\check{g}^R = (F_0 + F_a \hat{\sigma}^a)\hat{\tau}_1 + (G_0 + G_a \hat{\sigma}^a)\hat{\tau}_3. \tag{4.12}$$

The components proportional to $\hat{\tau}_3$ are the normal components. They determine the quasiparticle spectrum and enter the expression for the quasiparticle current. The off-diagonal terms in Nambu space, here proportional to τ_1, are the anomalous GFs and describe the superconducting condensate. The anomalous GFs have two components: F_0 describes the singlet condensate, whereas the component F_a describes the triplet component with zero total spin projection. Because we are considering diffusive systems, both components have s-wave symmetry. This implies that the triplet component is odd in frequency [214].

Using the expression for the Keldysh component in Eq. (4.3) and the parametrization of the Green's functions shown in Eq. (4.12), we can rewrite the self-consistency equation of the superconducting gap, Eq. (4.7), as

$$\Delta = \frac{\lambda}{2} \int_{-\Omega_D}^{\Omega_D} d\epsilon \, \mathrm{Im}\left[F_0(\epsilon)\right] \tanh\left(\frac{\epsilon}{2k_B T}\right) . \tag{4.13}$$

This is the equation for the self-consistent superconducting gap that we use, together with the Usadel equation in Eq. (4.6), to calculate the quasiclassical GFs in S/FI bilayers.

---

[2] Spin-flip processes are typically considered to be triggered by magnetic disorder at the S/FI interface and, therefore, it would have required exactly the same treatment as the one to go from the interfacial exchange field, h^a_{int}, in Eq. (4.5) to the effective one, h^a, in Eq. (4.6) [213]. We decided to obviate it for clarity in the presentation.

4.1.2 Transport effects: spin filtering

In this section, we consider diffusive heterostructures formed by stacked thin films, where the FI layer acts as a tunneling barrier between two other films and study the spin filtering effect that affects the current. Such an structure forms a junction, where the FI is the barrier that divides the two electrodes. For simplicity, we consider the FI to be totally polarized with its magnetization pointing towards the positive direction of the z axis. The spin filtering effect is originated from the spin dependent conductivity in the magnetic material, which favours the transfer of quasiparticles with the spin parallel to the polarization direction of the FI through the layer over those with antiparallel spin orientation. In particular, the spin filtering is described by the polarization vector $\boldsymbol{P} = P\boldsymbol{n}_z$, with $P \equiv \frac{G_\uparrow - G_\downarrow}{G_\uparrow + G_\downarrow}$, where $\boldsymbol{n}_z$ is the unit vector pointing along the z axis and $G_{\uparrow(\downarrow)}$ stands for the barrier conductance for spin up (down) quasiparticles. From the expression for the polarization of the barrier, P, it follows that $-1 < P < 1$.

Let us work again with the quasiclassical Green's functions defined in the Nambu ⊗ spin ⊗ Keldysh space that we describe in Sec. 4.1.1, Eqs. (4.1)–(4.4) and (4.12). Without lose of generality, we consider that the junction is at $z = 0$ and that it extends all through the the x−y plane. The spectral current flowing perpendicular to the ferromagnetic barrier reads [139, 140] (see Sec. 2.4.3):

$$\check{J}_z\Big|_{z=0} = \frac{G_N}{\sigma_n}\left[\hat{\Gamma}\check{g}^L\hat{\Gamma},\ \check{g}^R\right]_{z=0}, \tag{4.14}$$

where $G_T = G_\uparrow + G_\downarrow$ and σ_n are the normal state conductance of the junction and the Drude conductivity, respectively. In Eq. (4.14), $\check{g}^L$ and $\check{g}^R$ label the quasiclassical GFs on the *left* and *right* interfaces of the FI layer[3]. In Eq. (4.14), the matrix $\check{\Gamma}$ describes the effect of the spin-filtering layer and it is defined as

$$\check{\Gamma} = u + v\hat{\sigma}_3\hat{\tau}_3\ , \tag{4.15}$$

where the parameters u and v depend on the polarization of the barrier P as follows:

$$u = \sqrt{\frac{1 + \sqrt{1 - P^2}}{2}}, \tag{4.16}$$

$$v = \sqrt{\frac{1 - \sqrt{1 - P^2}}{2}}. \tag{4.17}$$

---

[3] Even though in the geometry considered here it would be more accurate to use *upper* and *lower* labels, we stick to the choice of *left* and *right* labels to be consistent all throughout the thesis.

One can easily check from these expressions that $u^2 + v^2 = 1$, that $2uv = P$ and that $u^2 - v^2 = \sqrt{1 - P^2}$. Using the spectral current in Eq. (4.14) one can calculate any desired observable current after taking the proper Nambu ⊗ spin Pauli component, as shown in Sec. 2.4.2.1 [see Eqs. (2.55) and (2.56)].

4.2 Spin-dependent transport between spin-split superconductors

In this section we study, both theoretically and experimentally, the charge transport flowing through a spin-polarized tunnel junction between two spin-split superconductors. The section is based on the work that we published in Ref. [215]. We present experimental measurements of the tunneling conductance of an EuS/Al/AlO$_x$/EuS/Al junction (see the inset in Fig. 4.1a) as a function of the applied voltage and magnetic field. The differential tunneling conductance, dI/dV, shows sharp peaks whose heights depend on the effective spin splitting induced in both Al layers and the spin filtering of the barrier. Below, we perform a self-consistent calculation that allows us to determine unambiguously the main parameters governing the transport of the junction

The text is organized as follows. In the next section, Sec. 4.2.1, we present the measurements of the tunneling conductance of the junction under consideration as a function of the magnetic field. In Sec. 4.2.2, we present a theoretical model based on the quasiclassical Green's functions for the description of the transport properties of a generic FI/S/I/FI/I/S/FI junction. In Sec. 4.2.2.1, we discuss the Josephson current through such junctions with emphasis on the anomalous behavior when the FI magnetizations are non-collinear. In Sec. 4.2.3, we focus on the quasiparticle current and the tunneling differential conductance. The latter is compared to the experimental data, and a discussion of the results follows.

4.2.1 Tunneling Conductance of a EuS/Al/AlO$_x$/EuS/Al junction

In this section we present our measurements of the current-voltage (I-V) characteristic of a EuS(4)/Al(4)/AlO$_x$/EuS(1.2)/Al(4.3) [4] junction (thickness in nanometers), see inset in Fig. 4.1a. The samples consist of cross bars fabricated by electron-

---

[4] During growth, the oxidation of the aluminum layer was not controled. Therefore, it does not necessarily have the stoichometry of Al$_2$O$_3$.

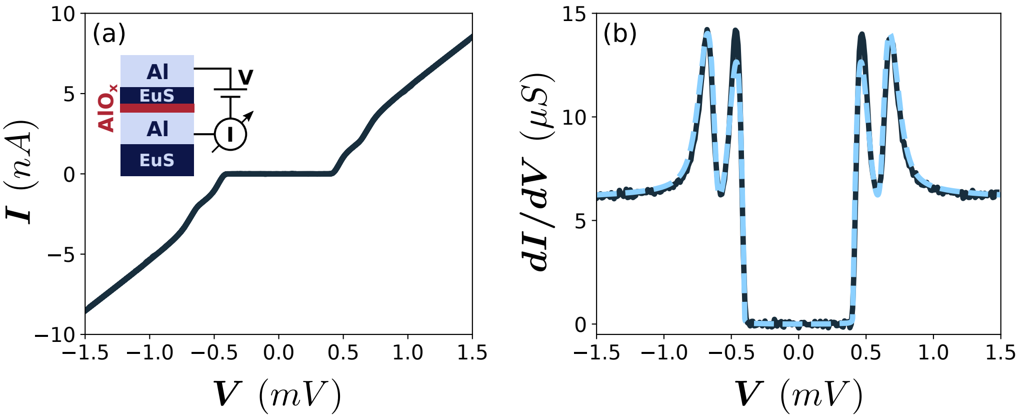

Figure 4.1: Tunneling spectroscopy of a FI/S/I/FI/S junction before applying an external magnetic field. (a) Typical current (I) vs voltage (V) characteristic of the junction measured at 25 mK. (b) Numerical derivative of the $I-V$ characteristic extracted from the data in panel (a)(black line). The blue dashed line is obtained from our theoretical model presented in Sec. 4.2.2. The parameters used for the fitting are: $G_T = 6\ \mu$S, $\Delta_0 = 320\ \mu$eV, $h_L = 0$, $h_R = 100\ \mu$eV, $\tau_{sf}^{-1} = 0.08\Delta_0$ and $\tau_{so}^{-1} = \tau_{orb}^{-1} = 0$. In the demagnetized regime, the effective spin splitting in the upper Al layer is negligibly small. The spin splitting arises from the very large domain structure of the bottom EuS layer, with size much larger than the superconducting coherence length ξ_0. The measured peak structure resembles the one measured in Ref. [216] without the spin-filtering effect at work [see discussion after Eq. (4.48) for more details].

beam evaporation on an in situ metallic shadow mask with a typical junction area of 290×290 μm^2 [216].

The tunneling spectroscopy is obtained by measuring the I-V characteristic in a DC two-wire setup, as sketched in the inset of Fig. 4.1a. From this measurement we determine the differential conductance, dI/dV, via numerical differentiation. The measurements are done at cryogenic temperatures in a filtered cryogen-free dilution refrigerator. We first cool down the sample from room temperature to 25 mK in a non-magnetic environment. Before applying any external magnetic field, we measure the I-V characteristic (Fig. 4.1a) and extract the dI/dV shown by the solid line in Fig. 4.1b. We then apply an in-plane magnetic field (up to 160 mT) strong enough to align the magnetization of both EuS layers, and start decreasing it. During this process, we measure the I-V characteristic and determine the tunneling conductance at each value of the applied magnetic field. The full dependence is shown in the color plot of Fig. 4.2d. Panels (a-c) in Fig. 4.2

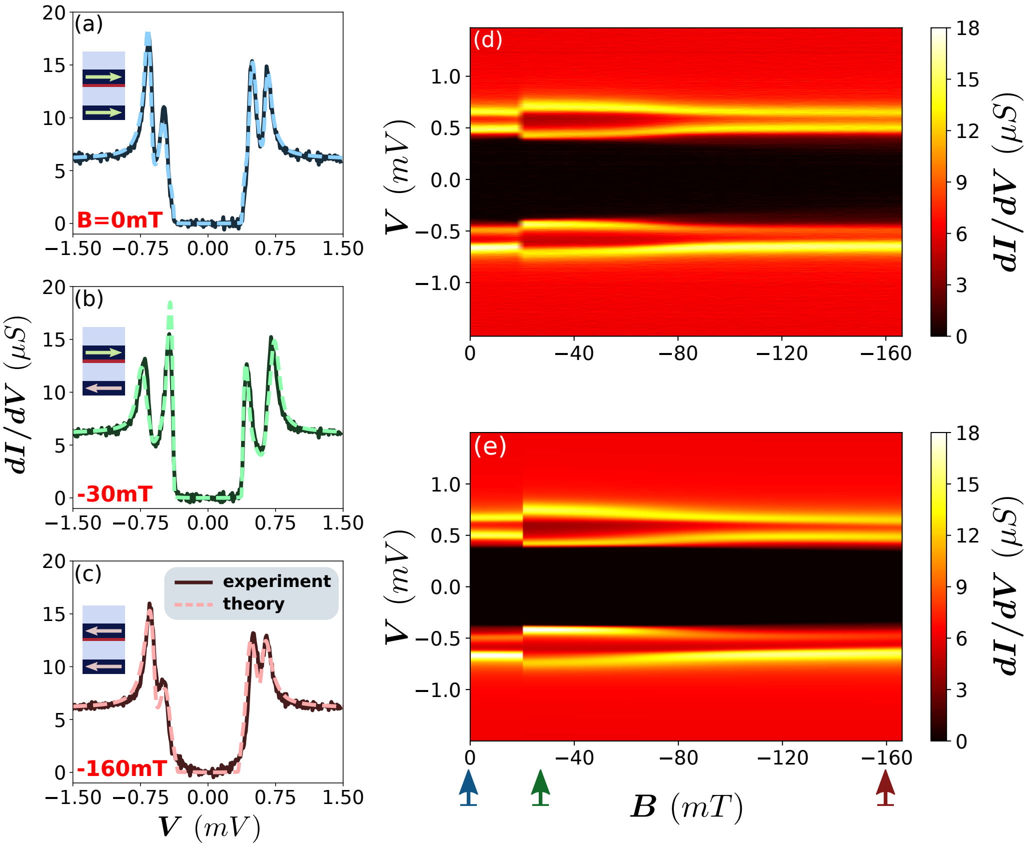

Figure 4.2: Magnetic-field dependence of the tunneling conductance of the spin-polarized junction. Before the measurement, the system is polarized with a positive magnetic field (B = 160mT). The differential conductance is then measured at different values of magnetic fields from 0 to −160mT. (a), (b) and (c) show three different curves measured at 0, -20 and -160 mT, respectively. (d) shows the full measured B-dependence. Panel (e) is the fitting resulting from the theoretical model.

correspond to different vertical cuts of Fig. 4.2d at the positions indicated by the arrows placed at the bottom of the figure.

The obtained tunneling conductance clearly shows the four-peak structure expected from the spin-split superconducting density of states (DOS) [39]. Notice that these peaks are also observed before applying any magnetic field, Fig. 4.1b. The position of the peaks in Figs. 4.2(a-c) is always symmetric with respect to the sign of the applied voltage, however, after the first magnetization of the junction, their heights are not. This behavior contrasts with the one shown in Fig. 4.1b for the demagnetized sample. The asymmetry is a fingerprint of spin-polarized tunneling through the middle EuS thin layer [197, 39, 40], which only after magnetization turns out to be apparent. In contrast, and according to the physical picture provided in Sec. 4.2.3, when the sample is demagnetized, the thin EuS barrier layer consists of magnetic domains smaller than the coherence length with random polarization directions. This leads to a negligibly small value of the induced spin-splitting field on the upper superconductor and no spin-filtering effect on the current after averaging over the junction area.

The separation between the peaks at positive (or negative) voltage, Fig. 4.1b and Fig. 4.2(a-c), provides information about the size of the spin-splitting energy induced in the Al layers. This splitting is proportional to the effective exchange energy between the spins localized at the EuS/Al interface and the Al conduction electrons [217].

We observe a sudden increase of the spin-splitting energy at -20 mT (Fig. 4.2d), which occurs when the system switches to the antiparallel configuration. As it turns out from our theoretical discussion in Sec. 4.2.3, it is the bottom EuS layer that switches first and abruptly. By further increasing the magnetic field, B, the parallel configuration is recovered gradually with a smooth switching of the middle EuS magnetization. The two rather different switching behaviors of the EuS films can be attributed to a different magnetic configuration and anisotropy of the two films due to different deposition conditions, which crucially depends on the growth morphology [218, 53].

Whereas the peak positions can be explained by using a simple tunneling model [40], detailed features such as the width and height of the peaks can only be understood by taking into account different scattering and depairing mechanisms and performing a self-consistent calculation of the superconducting order parameter. With this aim, in the next sections we present a theoretical model that allows us to describe the dI/dV curves, extract the values of the different parameters, and provide a physical picture that explains the full behavior shown in Fig. 4.2d.

4.2.2 Theoretical modeling

In this section we present a theoretical model to describe the electronic transport in junctions with spin-split superconductors and spin-filtering barriers. The goal of this section is twofold: On the one hand, to obtain general results for the current in tunnel junctions between two spin-split superconductors in the presence of a spin-filtering barrier. On the other hand, we provide a complete description of the experimental results presented in the previous section.

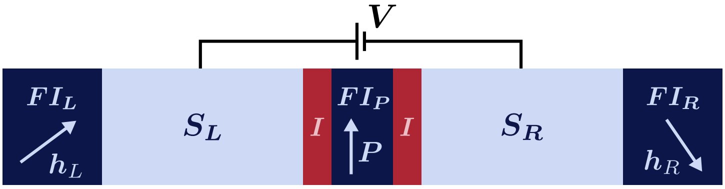

Figure 4.3: Schematic of a tunnel junction between two spin-split superconductors with a spin polarized tunneling barrier and biased at a voltage V. The left (right) superconductor $\mathrm{S_L}$ ($\mathrm{S_R}$) experiences a spin-splitting field $\boldsymbol{h}_L$ ($\boldsymbol{h}_R$) by an attached ferromagnetic insulator layer $\mathrm{FI_L}$ ($\mathrm{FI_R}$). The spin polarized tunneling barrier, with polarization $\boldsymbol{P}$, is another ferromagnetic insulator (FI). To avoid the magnetic proximity effect, the superconductors are separated from the spin-polarized tunneling barrier by insulating layers (I). The superconductor $\mathrm{S_L}$ ($\mathrm{S_R}$) is at temperature T_L (T_R).

We consider a generic junction, sketched in Fig. 4.3. It consists of two spin-split superconductors separated by a spin-polarized tunneling barrier. The spin-split superconductors correspond to two S/FI bilayers, whereas the tunneling barrier is an additional FI layer with adjacent thin insulating layers to decouple it magnetically from the superconductors.

To describe the current through the junction below, we use the tunneling Hamiltonian approach, such that the system is described by

$$\mathcal{H} = \mathcal{H}_L + \mathcal{H}_R + \mathcal{H}_T. \tag{4.18}$$

Here $\mathcal{H}_{L(R)}$ describes the left(right) superconducting electrode attached to a FI and $\mathcal{H}_T$ the tunneling of electrons between the superconductors [117].

In order to compute the current one needs to determine the spectral properties of the decoupled FI-S electrodes. We model them by assuming that the interaction between the localized magnetic moments in the FI and the conduction electrons in the S layer creates an effective exchange field in the latter [219, 220, 217, 32] (see Sec. 4.1.1). If the superconducting films are thinner than the coherence length such exchange field can be assumed to be homogeneous in the S and, hence, the S electrodes are described by

$$\mathcal{H}_{L(R)} = \mathcal{H}_{BCS} + \mathbf{h}_{L(R)} \cdot \hat{\boldsymbol{\sigma}} \,, \tag{4.19}$$

where $\mathbf{h}_{L(R)} = h_{L(R)}\mathbf{n}_{L(R)}$ is the exchange field pointing in the direction of the unit vector $\mathbf{n}_{L(R)}$, $\hat{\boldsymbol{\sigma}}$ is the vector of Pauli matrices and $\mathcal{H}_{BCS}$ is the BCS Hamiltonian that also includes random impurities, magnetic, non-magnetic and those with spin-orbit coupling [221].

For the tunneling Hamiltonian [the last term of Eq. (4.18)] we assume that the tunneling through the barrier is spin dependent; in other words, that the electron tunneling probability depends on whether its spin is oriented parallel or anti-parallel with respect to the barrier magnetization [140] (see Sec. 4.1.2).

We consider a general case where the directions of the magnetization in each of the three FIs are independent of each other. A voltage V is applied across the junction and, in principle, the temperatures of the two FI/S electrodes are different $T_L \neq T_R$. Here, the indices L and R denote the left and right electrode respectively.

The effective splitting of the left and right superconductors in Fig. 4.3 is given by the induced exchange fields $\boldsymbol{h}_L = h_L \boldsymbol{n}_L$ and $\boldsymbol{h}_R = h_R \boldsymbol{n}_R$ respectively, whereas the spin filtering is described by the polarization vector $\boldsymbol{P} = P\boldsymbol{n}_P$ with $P \equiv \frac{G_\uparrow - G_\downarrow}{G_\uparrow + G_\downarrow}$ and $-1 \leq P \leq 1$. The vectors $\boldsymbol{n}$ are unit vectors pointing in the respective directions, the magnitude of the exchange fields $h_{L/R}$ has energy units and $G_{\uparrow(\downarrow)}$ stands for the tunneling conductance through the junction for carriers with up (down) spin along the direction of $\mathbf{n}_P$.

Without loss of generality, we set the barrier magnetization along the z axis, $\boldsymbol{n}_P = (0, 0, 1)$, such that the magnetization orientations of the adjacent S/FI bilayers can be parametrized by three angles, $\theta_{L,R}$ and γ:

$$\boldsymbol{n}_L = (\sin\theta_L, 0, \cos\theta_L) \tag{4.20}$$

and

$$\boldsymbol{n}_R = (\sin\theta_R \cos\gamma, \sin\theta_R \sin\gamma, \cos\theta_R). \tag{4.21}$$

In a collinear configuration, *i.e.* $\theta_L = \theta_R = 0$, the current through the junction can be straightforwardly calculated from the well-known tunneling expression [40]. We next generalize the latter for non-collinear magnetizations. Moreover, in order to include the effects of spin relaxation and depairing, we use the quasiclassical Green's functions (GFs) for an accurate description of the spectrum of the S/FI electrodes. As described in Sec. 4.1.1, the quasiclassical GFs, $\breve{g}_s$ has the structure described in Eqs. (4.1)–(4.4), whereas the retarded component quasiclassical GFs on the each side of the junction is given by the following Usadel equation [Eq. (4.6)]:

$$\left[i\epsilon\hat{\tau}_3 - ih_s\hat{\tau}_3\hat{\sigma}^z - \Delta_s\hat{\tau}_1 - \check{\Sigma}_s,\ \check{g}_s^R\right] = 0, \tag{4.22}$$

where $s = L(R)$ stands for the left (right) electrode and we work in a local reference frame where $V = 0$, $\Delta = |\Delta|$ (*i.e.*, the superconducting phase is zero, $\varphi = 0$) and the exchange field is parallel to the z axis. In such a reference frame $\check{g}_s^R$

can be parametrized as in Eq. (4.12). In Eq. (4.22), $\check{\Sigma}_s$ stands for the self energy term described in Eqs. (4.8)–(4.11) and the superconducting order parameter, Δ_s, fulfills the self consistent equation, Eq. (4.7) or, alternatively, Eq. (4.13).

From Eq. (4.22) we obtain the quasiclassical GFs in the local reference frame of each electrode. We can now use these results to calculate the total electric current across the Josephson junction, sketched in Fig. 4.3, in the presence of a finite voltage, a phase difference and a non-collinear magnetic configuration. This can be done by a gauge transformation and a spin-rotation of the GFs.

In the presence of a voltage, the phase of a superconductor evolves in time as

$$\varphi(t) = \varphi + \frac{2eV}{\hbar}t\,, \tag{4.23}$$

where φ is the dc phase. We define the corresponding gauge matrix

$$\hat{U}(t) = \exp\Big(- i\varphi(t)\hat{\tau}_3\Big)\ . \tag{4.24}$$

If we assume that the voltage is applied on the left superconductor and the magnetizations of the two S/FI and the spin-filter barrier are non-collinear [see Eqs. (4.20-4.21)] we can obtain the GFs $\breve{\tilde{g}}$ from those obtained from Eq. (4.22) via the following transformations:

$$\breve{\tilde{g}}_L(t-t') = \hat{R}_L\ \hat{U}(t)\ \breve{g}_L(t-t')\ \hat{U}(t')^\dagger\ \hat{R}_L^\dagger, \tag{4.25}$$

$$\breve{\tilde{g}}_R(t-t') = \hat{R}_R\ \breve{g}_R(t-t')\ \hat{R}_R^\dagger. \tag{4.26}$$

Here, the operators $\hat{R}_s$ describe spin-rotations in the left and right electrodes:

$$\hat{R}_L = \exp\Big(- i\theta_L\hat{\sigma}^y/2\Big), \tag{4.27}$$

$$\hat{R}_R = \exp\Big(- i\gamma\hat{\sigma}^z/2\Big)\exp\Big(- i\theta_R\hat{\sigma}^y/2\Big)\ , \tag{4.28}$$

and the time-dependent Green's functions in Eqs. (4.27-4.28) are obtained from the GFs in frequency space:

$$\breve{g}_s(t-t') = \frac{1}{2\pi}\int_{-\infty}^{\infty} d\epsilon\ \breve{g}_s(\epsilon)\ e^{i\epsilon(t-t)}\ . \tag{4.29}$$

From Eqs. (4.25) and (4.26) we can now write the full expression for the time-dependent electric current across the junction shown in Fig. 4.3 [139] (see Sec. 4.1.2):

$$I_c(t) = \frac{G_T\pi}{16e}\,\mathrm{Tr}\Bigg(\hat{\tau}_3\Big[\breve{\tilde{g}}_L\overset{\circ}{,}\check{\Gamma}\breve{\tilde{g}}_R\check{\Gamma}\Big]^K\Bigg), \tag{4.30}$$

where G_T is the normal state conductance of the junction, $[\cdot \overset{\circ}{,} \cdot]$ is a commutator of convolutions[5], the superscript K stands for the Keldysh component of the commutator and Tr stands for the trace over the Nambu⊗spin spaces. This equation returns the proper component of the spectral current, Eq. (4.14), that corresponds to the charge current with the correct normalization terms.

Equation (4.30) is valid in the tunneling limit. The matrix $\check{\Gamma} = u + v\hat{\sigma}^z\hat{\tau}_3$ describes the effect of the spin-filtering layer, where the u and v parameters are defined in Eqs. (4.16) and (4.17).

After a lengthy but straightforward algebra we obtain from Eq. (4.30) the charge current through the junction which can be written as the sum of three components:

$$I_c(t) = I + J_1 \sin\left(\varphi + \frac{2eVt}{\hbar}\right) + J_2 \cos\left(\varphi + \frac{2eVt}{\hbar}\right) . \tag{4.31}$$

Here I is the quasiparticle tunneling current and the remaining part is the Josephson current. Specifically, J_1 is the usual Josephson critical current. The third term is proportional to the cosine of $\varphi(t)$. In a non-magnetic Josephson junction this term is finite only at non-zero bias. In the literature it is known as the $\cos\varphi$ term and has been widely studied [222, 223, 224]. Interestingly, in a magnetic junction this term can be non-zero even when $V = 0$. In this case this term leads to the so-called anomalous Josephson current that appears in certain magnetic system with spin-orbit coupling or inhomogeneous magnetization [225, 226, 227, 228, 229, 62, 63, 230, 231, 232, 233] and is discussed in more detail in Sec. 4.2.2.1.

From Eq. (4.30) we derive the expressions for the three components of the current in terms of the GFs. For the quasiparticle tunneling current, first term in Eq. (4.31), we obtain

$$\begin{aligned} I = \frac{G_T}{2e}\int_{-\infty}^{\infty} d\epsilon \Big[f_0(\epsilon + eV, T_L) - f_0(\epsilon, T_R)\Big]\Big\{ P\Big[\nu_{0L}(\epsilon + eV)\nu_{zR}(\epsilon)\boldsymbol{n}_R \cdot \boldsymbol{n}_P \\ + \nu_{zL}(\epsilon + eV)\nu_{0R}(\epsilon)\boldsymbol{n}_L \cdot \boldsymbol{n}_P\Big] + \nu_{0L}(\epsilon + eV)\nu_{0R}(\epsilon) \\ + \nu_{zL}(\epsilon + eV)\nu_{zR}(\epsilon)\Big[\boldsymbol{n}_L^{\parallel} \cdot \boldsymbol{n}_R^{\parallel} + \sqrt{1 - P^2}\, \boldsymbol{n}_L^{\perp} \cdot \boldsymbol{n}_R^{\perp}\Big]\Big\}, \end{aligned} \tag{4.32}$$

---

[5] When the operators depend only on the difference of times the convolution is defined as

$$(A \circ B)(t) = \int_{-\infty}^{\infty} dt' A(t - t')B(t' - t),$$

and, consequently, the commutator reads $\left[A\,;B\right] = (A \circ B)(t) - (B \circ A)(t)$.

where $\nu_{as}(\epsilon) \equiv \mathrm{Re}\big[G_{as}(\epsilon)\big]$ is the semi-sum ($a = 0$) and semi-difference ($a = 3$) of the spin-up/spin-down densities of states (DOS). In deriving this expression, we made use of the following relations between the unit vectors pointing in the direction of the polarization of the barrier, $\boldsymbol{n}_P$, and induced the exchange fields in the left, $\boldsymbol{n}_L$, and right, $\boldsymbol{n}_R$, electrodes. We define the parallel and perpendicular components of the exchange fields with respect to the polarization vector:

$$\boldsymbol{n}_s^{\parallel} \equiv (\boldsymbol{n}_s \cdot \boldsymbol{n}_P)\boldsymbol{n}_P = \cos\theta_s \boldsymbol{n}_P, \tag{4.33}$$

$$\boldsymbol{n}_s^{\perp} \equiv \boldsymbol{n}_s - \boldsymbol{n}_s^{\parallel}, \tag{4.34}$$

where $s = \{L, R\}$ labels the position of the electrode. According to these definitions and the unit vectors expressions of the Zeeman fields, Eqs. (4.20) and (4.21), we obtain the following useful relations:

$$\boldsymbol{n}_L \cdot \boldsymbol{n}_R = \boldsymbol{n}_L^{\parallel} \cdot \boldsymbol{n}_R^{\parallel} + \boldsymbol{n}_L^{\perp} \cdot \boldsymbol{n}_R^{\perp}, \tag{4.35}$$

$$\boldsymbol{n}_L^{\parallel} \cdot \boldsymbol{n}_R^{\parallel} = \cos\theta_L \cos\theta_R, \tag{4.36}$$

$$\boldsymbol{n}_L^{\perp} \cdot \boldsymbol{n}_R^{\perp} = \sin\theta_L \sin\theta_R \cos\gamma, \tag{4.37}$$

$$\boldsymbol{n}_P \cdot (\boldsymbol{n}_L \times \boldsymbol{n}_R) = \sin\theta_L \sin\theta_R \sin\gamma. \tag{4.38}$$

For the second and third terms in Eq. (4.31) we obtain that

$$J_1 = A_0\sqrt{1-P^2} + A_z\Big[\sqrt{1-P^2}\ \boldsymbol{n}_L^{\parallel} \cdot \boldsymbol{n}_R^{\parallel} + \boldsymbol{n}_L^{\perp} \cdot \boldsymbol{n}_R^{\perp}\Big] - B_z\ P\boldsymbol{n}_P \cdot (\boldsymbol{n}_L \times \boldsymbol{n}_R) \tag{4.39}$$

and

$$J_2 = B_0\sqrt{1-P^2} + B_z\Big[\sqrt{1-P^2}\ \boldsymbol{n}_L^{\parallel} \cdot \boldsymbol{n}_R^{\parallel} + \boldsymbol{n}_L^{\perp} \cdot \boldsymbol{n}_R^{\perp}\Big] + A_z\ P\boldsymbol{n}_P \cdot (\boldsymbol{n}_L \times \boldsymbol{n}_R), \tag{4.40}$$

where A_a and B_a ($a = 0, z$) are expressed in terms of the real and imaginary part of the anomalous GFs, $F_{as}(\epsilon)$, as follows:

$$\begin{aligned} A_a = \frac{G_T}{2e}\int_{-\infty}^{\infty} d\epsilon\Big[&f_0(\epsilon, T_R)\mathrm{Re}\big[F_{aL}(\epsilon + eV)\big]\mathrm{Im}\big[F_{aR}(\epsilon)\big] \\ &+ f_0(\epsilon + eV, T_L)\mathrm{Im}\big[F_{aL}(\epsilon + eV)\big]\mathrm{Re}\big[F_{aR}(\epsilon)\big]\Big], \end{aligned} \tag{4.41}$$

$$B_a = \frac{G_T}{2e}\int_{-\infty}^{\infty} d\epsilon\Big[f_0(\epsilon + eV, T_L) - f_0(\epsilon, T_R)\Big]\mathrm{Im}\big[F_{aL}(\epsilon + eV)\big]\mathrm{Im}\big[F_{aR}(\epsilon)\big]. \tag{4.42}$$

Equations (4.31-4.42) determine the total current through the junction and are used in the next sections. We start by analyzing the Josephson current in magnetic junctions.

4.2.2.1 Anomalous Josephson current

An interesting situation occurs when $V = 0$, $\varphi = 0$, $T_L = T_R$ and the magnetization vectors of the three FI layers are not in the same plane. In this case $I = 0$, $B_0 = B_z = 0$ and the only term contributing to the current J_2 is the one proportional to A_z in Eq. (4.40). The latter is finite when $\boldsymbol{n}_P \cdot (\boldsymbol{n}_L \times \boldsymbol{n}_R) \neq 0$, *i.e.*, when three vectors are not co-planar. In this case a finite Josephson current may flow through the junction even if the dc phase difference φ is zero. This is the so-called anomalous Josephson current and the junction is referred as a φ_0-junction. The latter has been widely studied in magnetic junctions with spin-orbit coupling [225, 234, 235, 231, 63, 62, 236] or multilayer metallic ferromagnets [237, 238, 239, 240, 234, 241, 233, 232].

In this section, we discuss the possible observation of the anomalous Josephson junction in FI/S-based junctions. This effect was not yet seen in the samples discussed here, because the large value of the normal-state resistance made it impossible to measure any Josephson current at the temprature of the experiments. However, similar type of samples with increased junction transparency would be good candidates for measuring the φ_0 effect.

Because we assume a unique temperature, $T_L = T_R = T$, and the junction is in equilibrium ($V = 0$), quasiparticle current is zero and one can write the expression for the Josephson current in terms of a sum over Matsubara frequencies. The anomalous functions proportional to the Pauli matrix σ^z correspond to the odd-in-frequency triplet components of the condensate, $F_z(i\omega_n) = -F_z(-i\omega_n)$, whereas those proportional to σ^0 arise from the singlet components $F_0(i\omega_n) = F_0(-i\omega_n)$ [30]. The total current, Eq. (4.31), can then be written as

$$J_1 = \pi T \frac{\pi G_T}{2e} \sum_{\omega} \left[\sqrt{1 - P^2} \left(F_0^2 + F_z^2 \boldsymbol{n}_L^{\parallel} \cdot \boldsymbol{n}_R^{\parallel} \right) + F_z^2 \boldsymbol{n}_L^{\perp} \cdot \boldsymbol{n}_R^{\perp} \right] \tag{4.43}$$

$$J_2 = \pi T \frac{\pi G_T}{2e} P \boldsymbol{n}_P \cdot (\boldsymbol{n}_L \times \boldsymbol{n}_R) \sum_{\omega} F_z^2. \tag{4.44}$$

The contribution proportional to $\sin\varphi$ contains the conventional singlet Josephson current that vanishes when the barrier is fully polarized $P = 1$. If the magnetizations and the barrier magnetization are non-collinear, there is an additional contribution stemming entirely from the interference of the triplet component of the condensate, as discussed in Refs. [140, 139].

The anomalous current in Eq. (4.44) is also a pure triplet current which requires non-coplanar vectors, *i.e.* a finite triple product $\boldsymbol{n}_P \cdot (\boldsymbol{n}_L \times \boldsymbol{n}_R)$, and it is proportional to the polarization of the barrier. The well-defined splitting and strong barrier polarization make the EuS/Al material combination suitable for the realization of such magnetic anomalous junctions.

In the limit $T \longrightarrow 0$, we obtain analytic results for the Josephson current by assuming equal amplitudes of the exchange fields, $h_L = h_R \equiv h$, and neglecting all relaxation processes, $\tau_{so}^{-1} = \tau_{sf}^{-1} = \tau_{orb}^{-1} = 0$:

$$J_1 = \frac{\pi G_T \Delta}{2e}\left[\sqrt{1-P^2}\eta + \left(\sqrt{1-P^2}\boldsymbol{n}_L^{\parallel}\cdot\boldsymbol{n}_R^{\parallel} + \boldsymbol{n}_L^{\perp}\cdot\boldsymbol{n}_R^{\perp}\right)\left(\eta-1\right)\right], \tag{4.45}$$

$$J_2 = \frac{\pi G_T \Delta}{2e}P\left(\eta-1\right)\boldsymbol{n}_P\cdot(\boldsymbol{n}_L\times\boldsymbol{n}_R), \tag{4.46}$$

where Δ is the real self-consistent superconducting order parameter at zero temperature and exchange field h and

$$\eta \equiv \frac{32\Delta^2(256\Delta^4 - 32\Delta^2 h^2 + 9h^4)}{(16\Delta^2 - h^2)^3} - 1. \tag{4.47}$$

In the case where $h = 0$ (and, therefore, $\boldsymbol{n}_L = \boldsymbol{n}_R = 0$), the coefficient $\eta = 1$ and Eq. (4.45) yields the well-known Ambegaokar-Baratoff [242] formula for the Josephson current with a prefactor $\sqrt{1-P^2}$ due to the barrier polarization.

4.2.3 Quasiparticle current and differential conductance

In this section, we discuss the quasiparticle current, Eq. (4.32), and use our theoretical framework to describe the experimental data shown in Figs. 4.1-4.2. In the following discussion, we identify the layer at the bottom (top) in the experimental setup, Fig. 4.1, with the left (right) electrode of the model in Fig. 4.3.

The experimental setup corresponds to a situation in which the EuS barrier serves two purposes: on the one hand, it acts as a spin-filtering barrier and, on the other hand, it causes the spin-splitting in one of the superconductors (the right one in Fig. 4.3). This means that the orientation of barrier magnetization coincides with the direction of the exchange field in the right superconductor, $\boldsymbol{n}_P = \boldsymbol{n}_R$, while the magnetization $\boldsymbol{n}_L$ is, in principle, independent of the magnetization of the barrier. The left superconductor (S_L) is in a good contact with the outer EuS, which induces a finite h_L. At the other interface between S_L and the tunneling barrier, a thin oxide layer is formed, preventing the exchange coupling [39]. Thus, for our specific sample, the thinnest FI layer in the middle is a tunneling barrier (1.2 nm) which induces the spin splitting only on the right superconductor and polarizes the current, whereas the thicker EuS layer (4 nm) causes the spin splitting in the left Al film.

Because the two EuS layers are of different thicknesses and they were grown on two different substrates, it is expected that the magnetization switching is different, as well as the strength of the induced exchange splittings in the superconductors, $h_R \neq h_L$. We assume the same superconducting order parameter, spin orbit and spin flip relaxation times for both Al films. Moreover the temperatures are assumed to be equal, $T_L = T_R = T$.

Because of the high normal-state resistance of the tunneling barrier (~ 160 kΩ), no Josephson current through the junction could be measured, as shown in the left panel of Fig. 4.1. In particular, the Josephson energy $E_J = \hbar J_1/(2e)$ was of the order of the temperature and, therefore, the thermal fluctuations of the phase smeared out the Josephson effect. The current shown in that figure corresponds only to the quasiparticle contribution and it can be determined from Eq. (4.32) for $\boldsymbol{n}_R \cdot \boldsymbol{n}_P = 1$ and $\boldsymbol{n}_R^{\perp} = 0$. We can parametrize the magnetic configuration of the junction by a single angle θ between the splitting field in the left and right superconductor: $\boldsymbol{n}_R \cdot \boldsymbol{n}_L = \boldsymbol{n}_P \cdot \boldsymbol{n}_L = \cos\theta$.

From Eq. (4.32), we compute the current and, after differentiation with respect to V, we obtain the differential tunneling conductance dI/dV. In Fig. 4.4, we show its dependence on the voltage for different values of the angle θ and certain values of spin splitting fields and spin relaxation times. For a collinear configuration of magnetizations, $\cos\theta = \pm 1$, the differential conductance shows the four-peak structure, observed in most of experiments on EuS/Al based structures [197, 39, 38, 40, 216]. These peaks appear at voltages $eV = \pm(\Delta_L + \Delta_R) \pm (h_L - \cos\theta h_R)$.

However, if the magnetizations of the FIs are non-collinear, we find a qualitatively new result (see the solid black line in Fig. 4.4). Instead of four peaks, the differential conductance shows eight peaks for any value of θ between 0 and π. These two different behaviors can be understood as follows: In the collinear case, the spin component along the single direction of magnetization is globally conserved and the two spin species tunnel independently. When the polarization of the tunneling barrier is non-collinear with the magnetization of one of the electrodes, tunneling does not conserve spin. The additional peaks in the dI/dV stem from the projection of the electron spin of one of the electrodes onto the local spin basis in the other electrode. The peaks in dI/dV then appear at $eV = \pm(\Delta_L + \Delta_R) \pm (h_L \pm h_R)$

This unusual situation occurs when the induced exchange field, and hence the magnetization of the EuS films, is spatially homogeneous, so that the eight-peak structure of dI/dV shown in Fig. 4.4 can only be observed if the EuS are monodomain magnets with non-collinear magnetizations. In our EuS/Al sam-

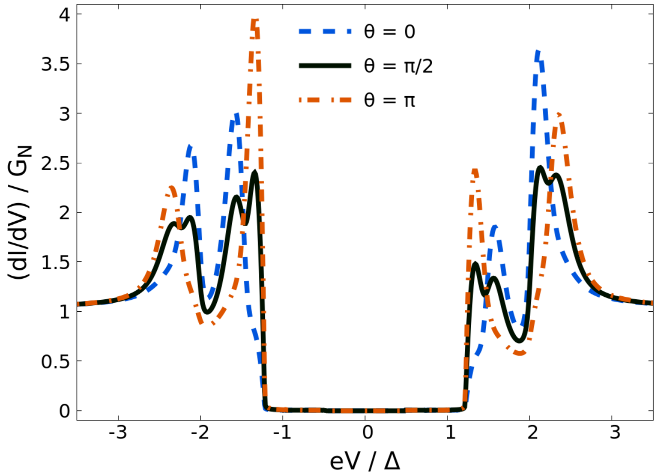

Figure 4.4: Normalized differential conductance spectrum of the $\mathrm{FI}_L/\mathrm{S}_L/\mathrm{I}/\mathrm{FI}_R/\mathrm{S}_R$ junction calculated from our theoretical model. Both superconductors are assumed to have the same order parameter, Δ_0. The polarization of the barrier is parallel to the exchange field induced in the right superconductor, $\boldsymbol{n}_P \parallel \boldsymbol{n}_R$, while the exchange field of the left superconductor forms an angle θ with $\boldsymbol{n}_R$. The dashed lines correspond to collinear situations, (blue) $\theta = 0$ and (red) $\theta = \pi$, while the solid black line corresponds to a non-collinear one, $\theta = \pi/2$. The remaining parameters used in the calculation are $\tau_{so}^{-1} = \tau_{orb}^{-1} = 0$ and $\tau_{sf}^{-1} = 0.08\Delta_0$ for the relaxation times in both superconductors, Zeeman splitting values of $h_L = 0.35\Delta_0$ and $h_R = 0.10\Delta_0$, a polarization of $P = 0.25$ and a global temperature of $k_B T = 0.01\Delta_0$.

ples the situation is rather different. As discussed in Ref. [216], EuS films consist of an ensemble of crystallites with intrinsic magnetization [243]. Therefore, before applying any external magnetic field, the magnetic configuration of the EuS layers consists of randomly oriented magnetic domains. Typically the size of EuS/Al tunnel junctions (here ~ 290 × 290 $\mu\mathrm{m}^2$) is much larger than the size of these domains and, therefore, the measured tunneling current is determined by an average over the angle θ, $\langle I \rangle_\theta \equiv \int_0^\pi \frac{d\theta}{\pi} I$, which reads:

$$\langle I \rangle_\theta = \frac{G_T}{2e} \int_{-\infty}^{\infty} d\epsilon \Big[f_0(\epsilon + eV, T_L) - f_0(\epsilon, T_R) \Big] \times \Big[\nu_{0L}(\epsilon + eV)\nu_{0R}(\epsilon) + P\nu_{0L}(\epsilon + eV)\nu_{zR}(\epsilon) \Big]. \tag{4.48}$$

We use this averaging procedure to fit the experimental data shown in Fig. 4.1, which corresponds to the situation before any magnetic field has been applied.

As discussed above, the finite spin-filtering coefficient P results in an asymmetry in the dI/dV curve with respect to the sign of V. However, Fig. 4.1 shows a quite symmetric curve. This can be explained by assuming that the domain size in the upper thin EuS layer is smaller than ξ_0 and, therefore, the possible splitting in the corresponding superconductor (R in our case) averages out. The absence of a Zeeman field in the right superconductor leads to an equal density of states for up and down electrons and, hence, $\nu_{3R}(\epsilon) = 0$. Consequently, the second term on the second line of Eq. (4.48) does not contribute to the current, which now does not depend on the spin polarization of the tunneling barrier.

The theory curve in Fig. 4.1b (blue line), is obtained for $G_T = 6\,\mu S$, which is the value of the conductance measured at sufficiently large voltages (see the right panel of Fig. 4.1). The superconducting gap at zero field and zero temperature is set to $\Delta_0 = 320\ \mu$eV in both Al layers. According to previous studies on the spin relaxation processes in aluminum layers [244, 245, 31], we set the spin-orbit relaxation time to $\tau_{so}^{-1} = 0.005\Delta_0$. The spin-flip relaxation is however enhanced due to the magnetic disorder caused by the adjacent EuS layer and we chose $\tau_{sf}^{-1} = 0.08\Delta_0$ in both Al layers. Since the measurements in Fig. 4.1 are for zero field then $\tau_{orb}^{-1} = 0$. The best fitting is obtained for $h_L = 100\ \mu$eV (bottom layer in the experiment), whereas $h_R = 0$ as explained above. The EuS at the bottom is a thicker film and its magnetic domain size is of the order of, or even larger than, the superconducting coherence length ξ_0 [216]. Therefore it induces a sizable exchange splitting in the bottom Al layer.

We now focus on the results of Fig. 4.2 when an external field is applied. These measurements are done after the first magnetization of EuS, *i.e.*, after a strong enough in-plane magnetic field is applied ($B = 160$ mT). After this, we switched off the B-field and measured the I-V characteristic varying the magnetic field from $B = 0$ to $B \approx -160$ mT. The differential conductance obtained by a numerical differentiation is shown with solid lines in panels (a-c) of Fig. 4.2 for $B = 0$, $B = -30$ mT and $B = -160$ mT, respectively. A full overview of the dI/dV is presented as a color map in panel Fig. 4.2(d).

From the four-peak structure of dI/dV and the theoretical prediction in Fig. 4.4, we can conclude that the average induced exchange fields in the left and right superconductors are collinear. After the application of the initial strong magnetic field, the magnetizations of both EuS are aligned in the direction of B. By decreasing the field until it switches its direction, the magnetization of the FIs may also switch at their corresponding coercive fields leading to the usual ferromagnetic hysteresis loop. Such switching events can be seen from the evolution of the peak positions in the dI/dV map in Fig. 4.2d.

We calculate the current using Eq. (4.32) and fit the data shown in Fig. 4.2. We use for the values of the spin-splitting fields for large magnetic fields (saturation of the magnetization of the EuS films) $h_L^{sat} = 120\ \mu$eV and $h_R^{sat} = 30\ \mu$eV. The difference between the values of the exchange fields after and before the first magnetization of the EuS layers is consistent with the result in Ref. [216]. In order to describe the evolution of the conductance peaks with the magnetic field we assume that the exchange field follows the evolution of the local magnetization. In particular, for the color plot in Fig. 4.2e we assume that $h_L(B) = h_L^{sat} \cdot y_L(B)$ and $h_R(B) = h_R^{sat} \cdot y_R(B)$, whereas spin-polarization of the barrier is chosen to be $P(B) = 0.25 \cdot y_R(B)$. Here, $y_L(B) = 1 - 2\theta(B + 20)$ and $y_R(B) = \tanh \frac{B+70}{40}$ are two empirical functions that describe the evolution of the magnetization in the bottom and top EuS layers as a function of the magnetic field B given in mT, where $\theta(x)$ is the step function.

We also take into account the orbital depairing in the superconducting layers due to the applied magnetic field, determined by [131, 118]

$$\tau_{orb}^{-1} = \left(\frac{\pi d \xi_0 B}{\sqrt{6}\Phi_0} \right)^2 \Delta_0, \tag{4.49}$$

where Φ_0 is the magnetic flux quantum, $d \approx 4$ nm is the width of the Al layers and $\xi_0 \approx 200$ nm is the superconducting coherence length.

The results of our fitting procedure are the dashed lines in panels (a), (b) and (c) of Fig. 4.2 and the color map in panel (e). All in a good agreement with the experimental data.

At first glance our fitting suggests an unexpected behavior: the thin EuS layer switches its magnetization slower than the thicker one. Here we provide a plausible explanation for this behavior, which can be caused by the different polycrystalline structures of EuS layers grown under different conditions. The 4 nm thick EuS (bottom layer in Fig. 4.2) is grown on an Al_2O_3 substrate, while the 1.2 nm barrier is grown directly on the previously oxidized underlying Al layer. As the oxidation of this layer is not controlled, its stoichiometry is completely different to the one on top of the substrate. Most likely, the thin layer consists of a more disordered set of crystallites and islands, resembling a superparamagnet. Such a large structural roughness could also arise from the propagation of defects created during growth in the bottom EuS and Al layers. If the RMS roughness is larger than half thickness of the top EuS layer, the layer would become discontinuous. Thus, the different thicknesses of the two EuS layers plays an important role in determining their magnetic properties as well. Presumably, the crystallites in the thick EuS layer are magnetically well coupled, while in the thin magnetic layer they form decoupled magnetic islands. Consequently, the EuS in the bottom would form magnetic domains on a scale much larger than the crystallite size, which leads to the sharp switching of the magnetization observed around $B = -20$ mT in Fig. 4.2d. In the thin EuS layer, by contrast, the macroscopic magnetization is an average over the magnetization of the crystallites. Due to disorder, the anisotropy is also random and such crystallites would not switch simultaneously, resulting into the gradual magnetization reversal that we observe from $B \approx -60$ mT to $B \approx -100$ mT in Fig. 4.2d. Moreover, the assumption of an island-like structure due to the growth morphology [218] can also explain the low polarization of the FI layer (25%) in comparison with previous results of near to 80% polarization [38, 197]. Indeed, it seems that the coverage of the EuS barrier is not complete and, in addition to the spin polarized current, there is a parallel direct tunneling current through the AlO_x layer.

4.3 Electron refrigeration in heterostructures with spin-split superconductors

The common way to refrigerate electron systems at sub-Kelvin temperatures is to lower the temperature of the whole sample via different refrigeration methods. In those cases the lattice temperature is lowered first, and the electron-phonon coupling then refrigerates the electrons. This mechanism becomes inefficient at low temperatures as, there, the phonons decouple from the electrons. An alternative scheme is to directly refrigerate the electrons. A scheme for such direct electron refrigeration was presented more than two decades ago [204, 205]. It is based on electron tunneling between a superconducting (S) electrode and a normal-metal (N) island, where the gapped density of states in S allows for a selective transport of hot electrons out of N by a proper choice of the bias voltage [208]. This refrigeration method is very efficient, as the absolute temperature of the N electrons can be lowered to a tiny fraction of the starting temperature [206, 207, 209, 210, 211]. This heat transfer through the junction could be used for the realization of on-chip cooling [212] of nanosized systems, such as highly-sensitive detectors and quantum devices.

At high starting temperatures (in case of Al-based microcoolers, typically above 200 mK) the mechanism limiting the lowest reached electron temperatures is the electron-phonon coupling. However, the electron refrigerators become especially useful below these temperatures. In those cases the limiting factor is rather the low coefficient of performance (COP, refrigeration efficiency): as the refrigeration requires electric power which comes with Joule heating, the excess heat is dumped into the superconductor, which then heats up, and the resulting backflow of heat limits the refrigeration. This has been partially cured with a design involving quasiparticle traps [210], but increasing the COP would allow for further progress.

The improvement of the cooling power due to a spin filter between N and superconducting (S) electrodes was theoretically discussed in Ref. [246]. However, the effect of spin-splitting was not considered in that work. More recently, the electronic cooling power between a ferromagnetic metal and a superconductor in the presence of an external magnetic field has been studied both theoretically and experimentally [54, 247]. It was shown that due to the spin-splitting field the cooling power can be larger with respect to the N-S coolers at certain subgap voltages. This is a direct consequence of the linear thermoelectric effect predicted in Ref. [54] and first observed in Ref. [201]. Improvement of the cooling at low voltages suggests an improvement of electron refrigeration. However, the electronic refrigeration and, in particular, the calculation of the reduction of the electron temperature in such structures has not been reported before.

Here we propose a way to improve the refrigeration efficiency by considering spin-split superconductors (SS), *i.e.* superconductors with a spin splitting in their density of states, coupled to other electrodes via ferromagnetic insulators (FI). The latter, on the one hand, acts as a spin-filter [198] and, on the other hand, induces a spin-splitting in the superconducting electrodes without the need of applying an external magnetic field, as observed in Al/EuS junctions [41, 42, 248, 249, 250, 216]. In a SS-FI-N junction the cooling power has a linear term in voltage and the optimal cooling power of N shifts to lower voltages. We show that this linear behavior also allows for cooling of the SS as the sign of the bias voltage across the junction is changed. Moreover, we also found that the cooling of the N-electrode in a N-FI-SS junction can be improved if N is substituted by a superconductor S’ with a gap smaller than SS gap. We finally analyze the electron refrigeration by computing the electron temperature in SS-FI-N-FI-SS, N-FI-SS-FI-N and SS-FI-S’-FI-SS junctions for different voltages and temperatures.

4.3.1 The model and basic equations

A typical setup for electron refrigeration is schematically shown in Fig. 4.5. The central island is the one refrigerated and it is tunnel coupled to two electrodes. The latter can be formed by a normal metal or a spin-split superconductor (SS). Besides the energy exchange between the electrodes and the island, carried by the quasiparticles, electron-phonon coupling establishes an energy flow from quasiparticles to the phonon bath of the different parts of the system. We assume

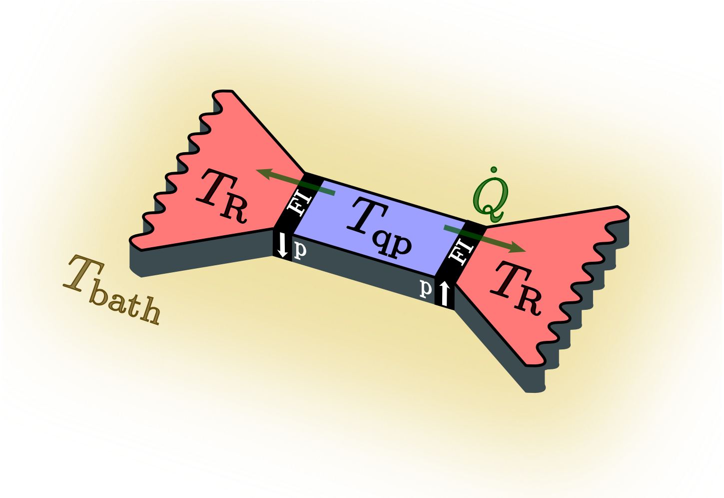

Figure 4.5: Schematic general setup: An island (blue) with quasiparticle temperature T_{qp} is electrically connected to two electrodes with quasiparticle temperature T_{R} through a spin-filtering thin layer of a ferromagnetic insulator. We assume that the film phonons strongly thermalize to the substrate and, thus, their temperature equals T_{bath}. $\dot{Q}$ stands for the cooling power of the island and white arrows show the spin polarization at each FI.

the film phonons to thermalize strongly to those at the thermal bath (*i.e.*, the substrate), so that their temperature equals T_{bath}. Decoupling the island from the substrate, however, can lead to phonon refrigeration and a consequent enhancement in the refrigeration of the quasiparticles, as it was reported in [207, 212].

We define the cooling power, $\dot{Q}$, as the energy current flowing out of the central island to the electrodes, whereas the energy current flow resulting from the electron-phonon coupling is labeled as $\dot{Q}_{\mathrm{qp\text{-}ph}}$. Our goal is to determine the final temperature of the quasiparticles in the central island, T_{qp}, when the system is voltage biased. This temperature can be calculated from the heat balance equation, which in the stationary situation (no build-up of energy) reads

$$\dot{Q}(T_{qp}, T_R) + \dot{Q}_{\mathrm{qp\text{-}ph}}(T_{qp}, T_{\mathrm{bath}}) = 0 \ . \tag{4.50}$$

Here, T_R is the quasiparticle temperature in the electrode(s), which can differ from T_{bath} if the thermalization is incomplete. In practice, the electrodes may heat up close to the junction. We model this heating by considering a finite size of the electrodes as well as that of the island. In addition, the cooling power $\dot{Q}$ depends on the bias voltage and other system parameters, as discussed in each of the examples consider below.

The quasiparticle-phonon heat flow entering Eq. (4.50) is given by [251, 252]

$$
\begin{aligned}
\dot{Q}_{\text{qp-ph}} = &-\frac{\Sigma\Omega}{96\zeta(5)}\int_{-\infty}^{\infty} d\epsilon\ \epsilon \int_{-\infty}^{\infty} d\omega\ \omega^2\ \text{sgn}(\omega) L_{\epsilon,\epsilon+\omega} \\
&\times\left\{\coth\left(\frac{\omega}{2T_{\text{ph}}}\right)\left[\tanh\left(\frac{\epsilon}{T_{\text{qp}}}\right)\tanh\left(\frac{\epsilon+\omega}{2T_{\text{qp}}}\right)\right]\right. \\
&\left.-\tanh\left(\frac{\epsilon}{2T_{\text{qp}}}\right)\tanh\left(\frac{\epsilon+\omega}{2T_{\text{qp}}}\right)+1\right\}, \qquad (4.51)
\end{aligned}
$$

where Σ is a constant describing the coupling strength, Ω stands for the sample volume, $\zeta(5) \approx 1.037$, we set $k_B = 1$, and the kernel $L_{\epsilon,\epsilon'}$ reads

$$
L_{\epsilon,\epsilon'} = \frac{1}{2}\sum_{\sigma=\pm}\nu_S(\epsilon_\sigma)\nu_S(\epsilon'_\sigma)\left[1-\frac{\Delta(T_{qp},h)}{\epsilon_\sigma\epsilon'_\sigma}\right]. \qquad (4.52)
$$

Here $\nu_S(\epsilon) = \text{Re}\left[(\epsilon+i\Gamma)/\sqrt{(\epsilon+i\Gamma)^2-\Delta^2}\right]$ is the density of states of the superconductor, we define $\epsilon_\pm \equiv \epsilon \pm h$, where h is the effective spin splitting, Γ stands for the Dynes parameter [145, 146] and $\Delta(T_{qp}, h)$ is the self-consistently calculated superconducting order parameter [31]. Both the DOS and the self-consistent equation for Δ that we use in this section are obtained from the quasiclassical GFs of the model described in Sec. (4.1.1) in absence of spin relaxation and/or orbital depairing processes [*i.e.*, $\check{\Sigma} = 0$ in Eq. (4.6)]. If the central conductor is a normal metal (i.e. $\Delta_0 \equiv \Delta(0,0) = 0$), $\dot{Q}_{\text{qp-ph}}$ simplifies to [253]

$$
\dot{Q}^N_{\text{qp-ph}} = \Sigma\Omega\left(T^5_{\text{qp}} - T^5_{\text{ph}}\right). \qquad (4.53)
$$

These results, along with the ones shown in the following section, are used in Sec. 4.3.3 to determine the final electronic temperature of the island for different systems with geometries equivalent to the one displayed in Fig. 4.5.

4.3.2 Cooling power of a SS-FI-N junction

We first analyze the cooling power $\dot{Q}$ of a SS-FI-N junction, where SS is a spin-split superconductor. We assume that the spin-filter efficiency of the ferromagnetic insulator is 100% and hence we can neglect the Andreev-reflection processes at the barrier [254]. Such an assumption is justified in the case of EuO and EuS barriers with spin-filter efficiencies > 95% [255]. The suppression of coherent processes such as Andreev reflection enables us to describe the problem within the tunneling formulation (see below Eq. (4.54)) which substantially simplifies the calculations.

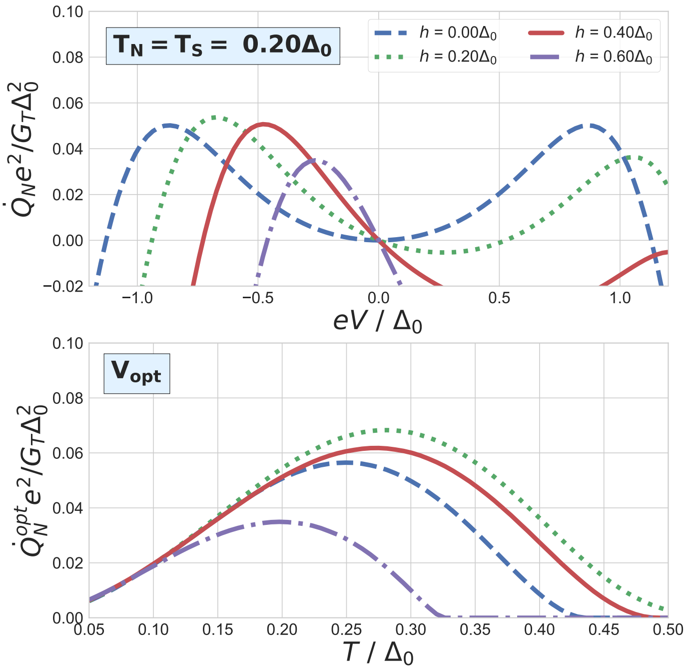

Figure 4.6: (*top*) Cooling power $\dot{Q}_N$ of the metallic electrode as a function of the bias voltage at $T_N = T_S = 0.2\Delta_0$ for different values of the exchange field h. (*bottom*) Cooling power optimized vs. bias voltage as a function of the temperature of the junction $T = T_N = T_S$. V_{opt} stands for the applied bias for which $\dot{Q}^{opt}$ is obtained.

The junction can be both temperature and voltage biased, and the cooling power in each of the electrodes is given by [31],

$$\dot{Q}_i = \frac{G_T}{e}\int_{-\infty}^{\infty} d\epsilon(\epsilon + \mu_i)\nu_N\left[\nu_+ + P\nu_-\right](f_N - f_{SS}), \tag{4.54}$$

where $i = \{N, SS\}$ labels the metal and the spin-split superconductor, $\mu_i = eV_i$ is the electrochemical potential on each of the samples, G_T is the normal-state conductance of the junction, $\nu_\pm \equiv \frac{1}{2}\left[\nu_S(\epsilon + h) \pm \nu_S(\epsilon - h)\right]$ takes into account the spin-split DOS of the superconductor and $f_{SS} \equiv f(\epsilon)$ and $f_N \equiv f(\epsilon + eV_N)$, where $f(\epsilon) = 1/(1 + e^{\epsilon/T})$ stands for the Fermi-Dirac distribution function.

The combination of spin splitting and spin filtering effectively moves the Fermi level in the superconductor from the middle of the superconducting gap an energy equal to h. This situation breaks the preexistent electron-hole symmetry of the currents and, consequently, it makes $\dot{Q}$ asymmetric in voltage.

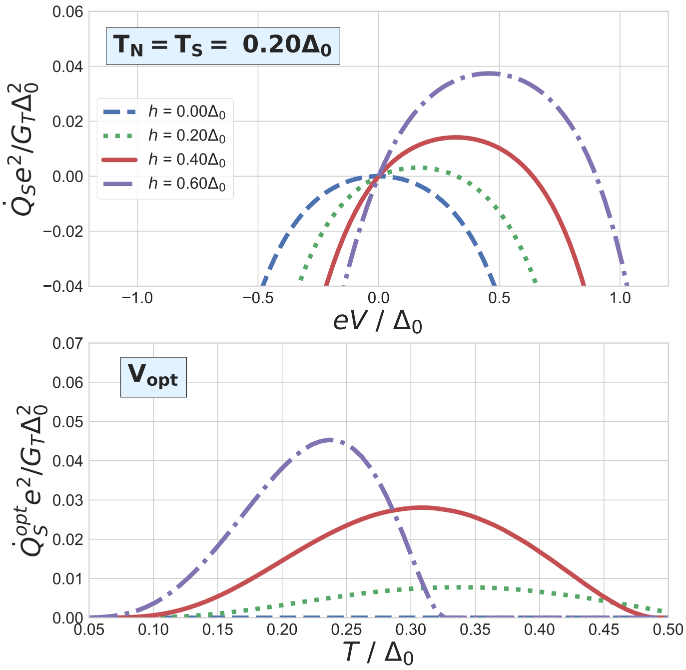

Figure 4.7: (*top*) Cooling power $\dot{Q}_S$ of the spin-split superconductor as a function of the bias voltage for different values of the exchange field h, at $T_S = T_N = 0.2\Delta_0$. (*bottom*) Cooling power for optimal bias voltage V_{opt}, as a function of the temperature of the junction $T = T_N = T_S$.

In Figs. 4.6 and 4.7 the cooling power in the normal metal, $\dot{Q}_N$, and the spin-split superconductor, $\dot{Q}_{SS}$, are shown for different spin-splitting amplitudes h. In the upper panels their bias dependence at a given temperature is shown, whereas in the lower panels the maximum of cooling power $\dot{Q}^{opt}$ is represented in terms of the temperature of the junction.

For the normal-metal cooling (Fig. 4.6), the most important effect is the shift of the maximum cooling power, $\dot{Q}_N^{opt}$, towards lower values of V by increasing the value of h. Since the Joule heating driven by dissipative currents is given by $P_J = IV$, this shift towards lower bias voltages implies lower dissipation [201]. On the other hand the maximum cooling power $\dot{Q}_N$ may decrease on increasing h due to the suppression of the superconducting gap. This is the case of the $h = 0.6\Delta_0$ curve in Fig. 4.6, for which the superconductor makes a transition to the normal state at $T \approx 0.32\Delta_0$. In the next section we study the consequences of this behavior on the electronic refrigeration.

If we now focus on the cooling power in the superconducting electrode (Fig.

4.7) it is interesting to notice that the spin splitting opens the possibility to refrigerate it. In the upper panel of Fig. 4.7 one clearly sees the linear behavior of the cooling power for low positive voltages for a non-zero exchange field h. In this case, larger spin-splitting implies better cooling. Of course the superconducting phase transition limits this enhancement only to temperatures lower to the critical one, as can be seen in the bottom panel of Fig. 4.7.

4.3.3 Electron refrigeration

In the previous section, Sec. 4.3.2, we calculated the cooling power of each electrode in a SS-FI-N junction as the amount of energy flowing out from the electrode per unit of time due to hot quasiparticle extraction. In this section we combine these results together with the energy transfer happening between the electronic system and the bath of thermalized phonons, Eq. (4.50), to calculate the final electronic temperature of the island in a system like the one sketched in Fig. 4.5 for various combinations of materials.

4.3.3.1 N-FI-SS-FI-N structure

We first consider a spin-split superconducting island between two metallic electrodes. We assume both junctions to be identical and, in order to enhance the cooling power, the polarizations of the spin filters are directed opposite to each other. Such a setting is analogous to the n-p-n or p-n-p thermoelectric setups containing two junctions with opposite thermoelectric coefficients in series. In this configuration, the total heat current flowing out of the island is two times larger than the one obtained from Eq. (4.54) for a single interface.

Cooling power only gives information about the extraction of *hot carriers* from the system of interest. In order to quantify the refrigeration (which implies change in the temperature) thermalization processes must be taken into consideration via the electron-phonon coupling. Combining the cooling power, $\dot{Q}$, with the heat flowing to the phonons, $\dot{Q}_{\text{qp-ph}}$ [Eq. (4.51)], we can obtain the final temperatures of the island by solving Eq. (4.50).

In order to simplify the notation, we group all the parameters in a single dimensionless one,

$$\tilde{\Sigma} \equiv \frac{\Sigma\Omega\Delta_0^3 e^2}{G_T k_B^5}. \tag{4.55}$$

Values of the coupling parameter Σ are presented in Ref. [208]. We set $\tilde{\Sigma} = 300$

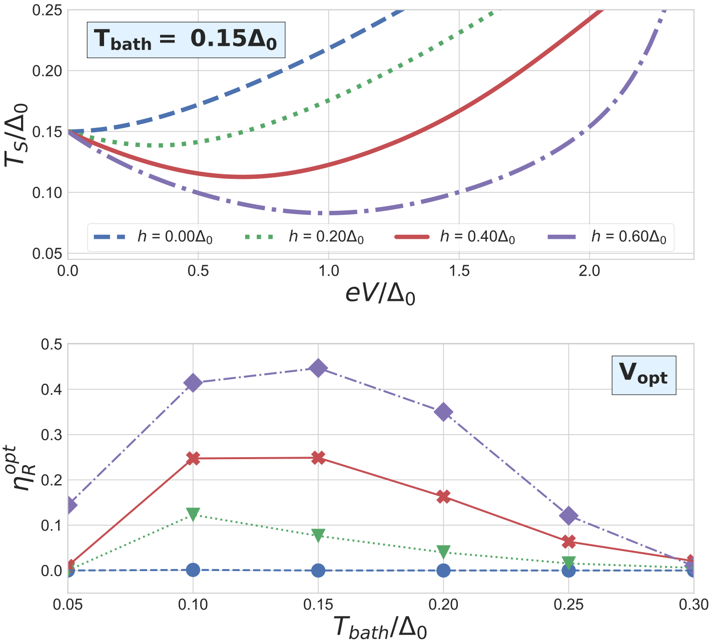

Figure 4.8: (*top*) Final temperature of the superconducting island vs. the voltage across the structure for $T_{\text{bath}} = 0.15\Delta_0$. (*bottom*) Optimum value of the relative refrigeration efficiency, $\eta_R \equiv (T_{\text{bath}} - T_{qp})/T_{\text{bath}}$, in terms of phonon temperature. Both values are obtained for different spin-splitting amplitudes and a qp-ph interaction parametrized by $\tilde{\Sigma} = 300$.

which corresponds to a junction with a resistance of $R_T \sim 1\ \text{k}\Omega$ in an aluminum sample with $\Omega \sim 1\ (\mu\text{m})^3$.

The top panel of Fig. 4.8 shows the final temperatures of the spin-split superconducting island as a function of the bias voltage across the whole structure for different values of the exchange field h. Here, we disregard heating of the electrodes, so the quasiparticle temperature in them equals the bath temperature, $T_N = T_{\text{bath}}$. In the absence of an exchange field, refrigeration of the superconducting island cannot be achieved, whereas a non-zero spin-splitting field allows for it.

The bottom panel of Fig. 4.8 shows the refrigeration efficiency at different bath temperatures T_{bath}. For this, we define the *relative refrigeration efficiency*,

$$\eta_R \equiv \frac{T_{\text{bath}} - T_{\text{qp}}}{T_{\text{bath}}}, \tag{4.56}$$

indicating the relative temperature drop in the island, and plot it for different h values. The bottom panel of Fig. 4.8 shows a strong dependence of the refrigera-

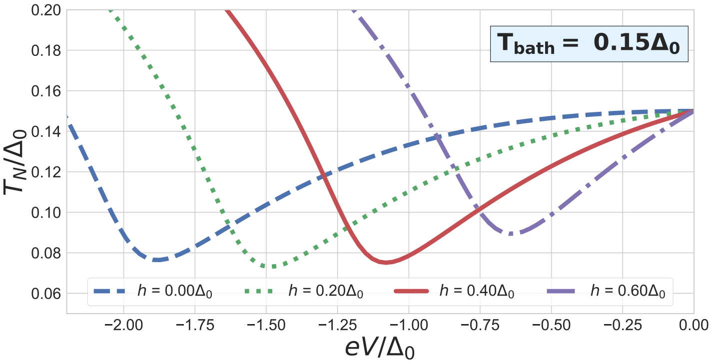

Figure 4.9: Steady-state temperature in the metallic island attached to two SS electrodes as a function of the bias voltage V across the structure for different exchange fields h. Here we disregard the heating of the electrodes. The qp-ph interaction in the normal metal is parametrized by $\tilde{\Sigma}_N = 300$.

tion efficiency on the temperature of the phonon bath, which is consequence of the competition between how $\dot{Q}_{SS}^{opt}$ and $\dot{Q}_{\text{qp-ph}}^{SS}$ change with T_{qp} and T_{bath}. The dependence of the former is shown in Fig. 4.7 and discussed in Sec. 4.3.2, while the absolute value of the latter quickly increases with increasing temperature (*i.e.* with an increasing number of phonons). Therefore, at low temperatures the refrigeration efficiency is mainly governed by $\dot{Q}_{SS}(T_{qp}, T_{\text{bath}})$, whereas the rapidly increasing density of phonons governs η_R^{opt} at high bath temperatures, dropping the refrigeration efficiency to very small values.

Notice that at very low temperatures, the electron-phonon relaxation is so weak that, in fact, it does not determine the ultimate minimum temperature that can be achieved. It is the anomalous heating caused by the nonzero DOS within the superconducting gap, which depends on the Dynes parameter Γ [145], that determines it [206].

4.3.3.2 SS-I-N-I-SS structure

We now focus on the refrigeration of a normal metal island between two spin-split superconducting electrodes. The polarization direction of the spin filters is again opposite to each other in order to optimize the refrigeration. The cooling power in this configuration equals twice the one in Eq. (4.54) with $\mu_i = eV/2$, where V is the bias voltage across the whole structure.

As seen in Fig. 4.6, the spin splitting in the superconducting density of states shifts the maximum of cooling power in the normal metal towards lower values of V. This implies lower dissipation and, hence, less heat on the superconducting electrodes.

We first disregard the heating of the electrodes by assuming perfect reservoirs for which the temperature is fixed to T_{bath} and compute the temperature T_N in the normal island. Results are shown in Fig. 4.9.

As expected from the results on the cooling power shown in Fig. 4.6, there is not much improvement of the refrigeration for a finite h, but the optimal refrigeration occurs at lower voltages.

We now consider the effect of the electrode heating on the previous results. We do this by adding a second heat balance equation concerning the electrodes, assuming for simplicity that they are uniformly heated across a volume Ω_{SS}. Thus, we get two coupled heat balance equations for the two temperatures T_N and T_{SS},

$$\begin{cases} 2\dot{Q}_N(T_N, T_{SS}) + \dot{Q}^{N}_{\text{qp-ph}}(T_N) = 0 \\ \dot{Q}_{SS}(T_N, T_{SS}) + \dot{Q}^{SS}_{\text{qp-ph}}(T_{SS}) = 0 \end{cases}, \tag{4.57}$$

where the factor of 2 stems from the fact that the metallic island is connected to two electrodes. Obviously the heat currents in Eq. (4.57) also depend on other parameters like the bias potential or the spin-splitting amplitude, which for simplicity are not explicitly written.

We use Eqs. (4.57) to describe a typical experimental situation. Even though the volume of the electrodes is typically much larger than that of the island, the bad heat transport properties of superconductors at low temperatures would generate a temperature gradient in them, *i.e.* local heating close to the interface. As shown in Ref. [210], this unwanted effect can be palliated using metallic quasiparticle traps near the junction. The traps dissipate heat more efficiently than the superconductor and, hence, reduces the local temperature of the electrode near the interface.

In Fig. 4.10 we show the obtained results in the case where the volumes of the electrodes and the island are comparable (in particular, when $\tilde{\Sigma}_N = \tilde{\Sigma}_{SS} = 300$). In this configuration, the spin splitting enhances the refrigeration in the island, with an optimal exchange field around $h \sim 0.4\Delta_0$. For higher h, the reduction of the Joule heating of the electrodes does not compensate the decrease of $\dot{Q}_S$. Moreover, the crossing between the blue and purple lines in the bottom panel of Fig. 4.10 is a consequence of the strong decrease of Δ near the critical temperature. In particular, at $T = 0.3\Delta_0$ and $h = 0.6\Delta_0$, $\Delta \approx 0.5\Delta_0$.

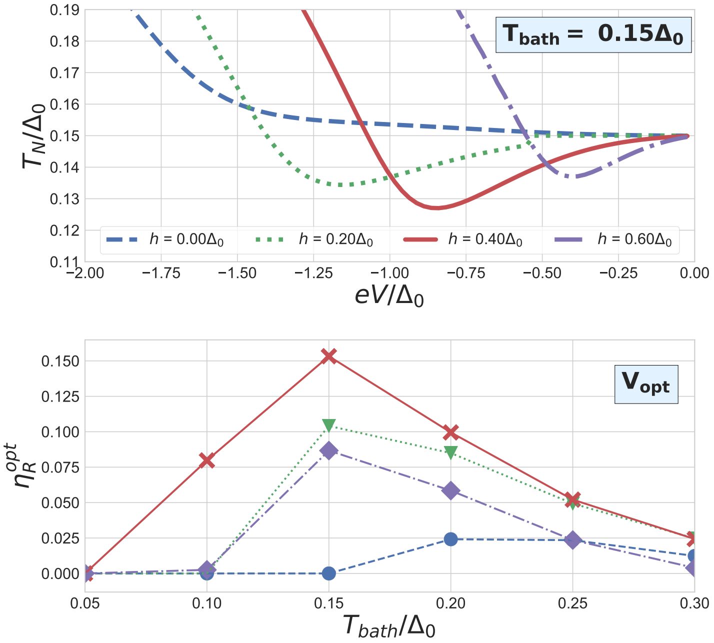

Figure 4.10: (*top*) Steady-state electronic temperature of the metallic island between two finite spin-split superconductors as a function of the bias voltage V across the whole structure. (*bottom*) Optimum value of the relative refrigeration efficiency as a function of phonon temperature. Results are obtained for different values of h in a particular case where $\tilde{\Sigma}_{SS} = \tilde{\Sigma}_N$.

4.3.3.3 SS-S'-SS structure

We finally analyze the refrigeration of a superconducting island (S') between two spin-split superconducting electrodes (SS). The order parameter of the island at zero temperature, Δ_0', is assumed to be smaller than the one of the spin-split electrodes Δ_0 at $T = 0$ and $h = 0$.

As in previous cases, we assume two thin FI layers with opposite polarizations connecting the island with the electrodes. The cooling power of the island is given by Eq. (4.54), where instead of the normal metal DOS we write the usual BCS one: $\nu_{S'}(\epsilon) = \mathrm{Re}\left[(\epsilon + i\Gamma)/\sqrt{(\epsilon + i\Gamma)^2 - \Delta'^2}\right]$, where $\Delta' \equiv \Delta'(T_{S'})$ is obtained self-consistently.

We first show in Fig. 4.11 the results for $\dot{Q}_{S'}$ in a single SS-FI-S' junction, for different values of h and Δ_0' as a function of the voltage bias, V. The bath temperature has been chosen as $T_{bath} = 0.2\Delta_0$. Thus, for $\Delta_0' = 0.2\Delta_0$ (dotted blue

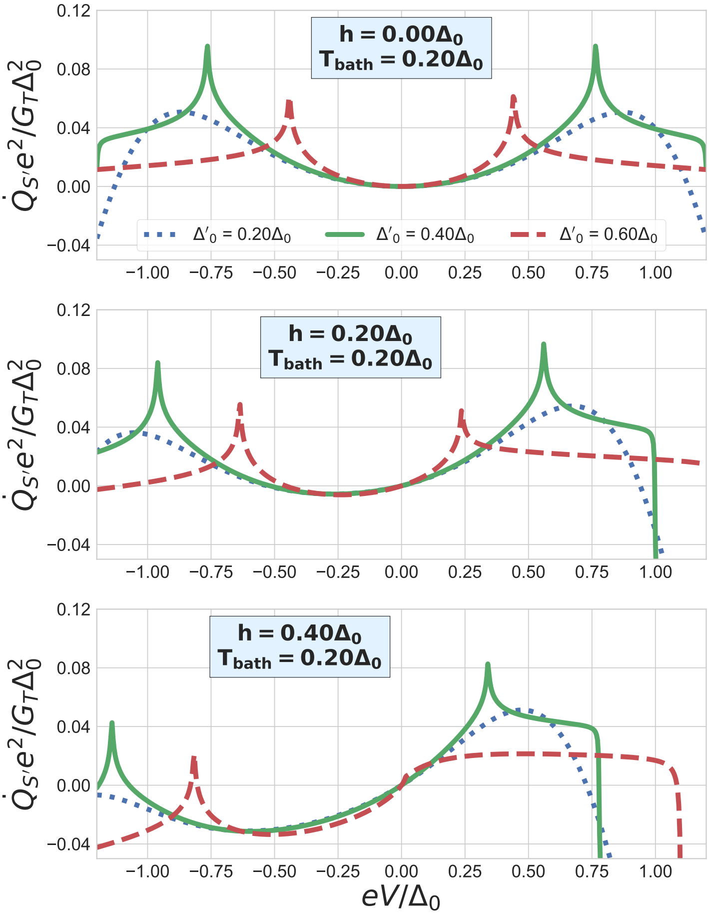

Figure 4.11: Cooling power $\dot{Q}_{S'}$ as a function of the applied voltage for different exchange fields and order parameters $\Delta'_0 = \Delta'(T = 0)$ of the superconducting island. $T_{\text{bath}} = 0.2\Delta_0$ is set in all the plots.

curve in Fig. 4.11) the bath temperature is larger than the superconducting critical temperature of the island and, hence, this corresponds to a SS-FI-N junction (*cf.* Fig. 4.6). For larger values of Δ'_0, the island remains in the superconducting state and its cooling power shows peaks at $eV \approx h \pm (\Delta - \Delta')$ (Fig. 4.11), *i.e.* the voltage for which the BCS-coherent peaks in the DOS of S' and SS line up. At these values $\dot{Q}$ is logarithmically divergent in the absence of inelastic scattering [222, 223]. A finite Dynes parameter leads to a finite height and broadening of these peaks [256, 206].

Correspondingly, the electron refrigeration is highly enhanced at voltages of those peaks, as shown in Fig. 4.12. In the calculations, we assume that the *SS* electrodes are perfect reservoirs with electronic temperature equal to T_{bath}.

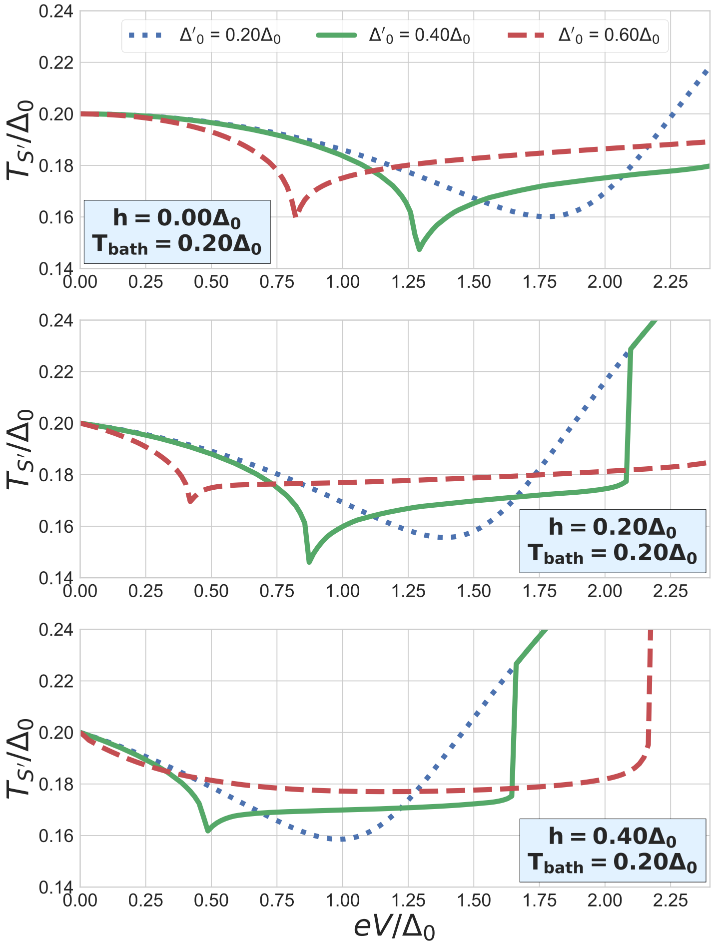

Figure 4.12: Steady-state temperatures in the island as a function of the bias voltage for different values of exchange fields and superconducting order parameters Δ'_0. We set $T_{\text{bath}} = 0.2\Delta_0$, disregard heating of the electrodes, and parametrize the qp-ph interaction in the island by $\Sigma_{S'} = 300$.

Moreover, in principle a temperature difference between the superconductors may induce a phase-coherent heat current proportional to $\cos\varphi$, where φ is the phase difference between the superconductors [257, 258]. This current, however, is proportional to $\sqrt{1-P^2}$ and hence vanishes in the case with perfect spin filters [259] considered here, $P = \pm 1$.

4.4 Geometry optimization of a Josephson phase battery

Up to this point in the thesis, we have only considered effects related to the interplay between the superconducting correlations and Zeeman fields. In this section, we go one step further and add the flavour of spin-orbit coupling (SOC) to the "cocktail". The interplay between superconductivity, magnetism and SOC leads to magnetoelectric effects, such as the spin Hall effect [72, 73], the Edelstein effect [74, 75] or its inverse [76, 77], that can find a lot of applications. Systems with such features can be realized as structures formed by a superconducting layer (S) on top of a ferromagnetic layer (F) that presents an interfacial Rashba-like spin-orbit coupling (SOC) [59, 60] at its lower interface (see Fig. 4.13 below). The coexistence of SOC and magnetic exchange field, couples the singlet and triplet components of the superconducting condensate that leaks from the S wire via proximity effect, generating anomalous charge currents flowing along the lower interface of F. If the triple product between the direction of the Zeeman field, the symmetry axis of the Rashba SOC and the axial direction of the wire is nonzero, the anomalous charge current flows along the wire [84, 85]. When we restrict the wire to have a finite length a superconducting phase difference, φ_0, is generated between the ends of the wire. This phase difference creates a supercurrent, equal and opposite to the anomalous one, that accounts for a net zero charge current flowing along the wire. When plugging such a device into a superconducting circuit, a supercurrent flows along the circuit. Thus, we know these devices as *Josephson phase batteries* [86, 87], in analogy to the usual batteries used in common electronics.

In this section, we explore in detail such a device and focus on the optimization of the φ_0 effect. As we find, in an infinite system like the one shown in Fig. 4.13, the supercurrent that counter-flows the anomalous current mostly flows along the S layer because that is where the density of the superconducting condensate is higher. This situation generates a distribution of the phase that is linear in space and that, for typical experimental values of the parameters, yields to very small φ_0 accumulations along lengths about the superconducting coherence length, ξ_0. Such accumulation can be greatly enhanced around regions where the top S layer gets interrupted along a distance L [62, 86]. In those regions the supercurrent is restricted to flow along the F wire, where the superfluid density is much smaller. If $L < \xi_0$, the anomalous current flowing along the SOC-active interface does not change much. Consequently, in order to counteract the anomalous current, the gradient of the phase has to increase a lot (in comparison with the situation where the S layer is present). The accumulated phase across the interruption will depend on its size, the size of the lateral superconducting leads and, more interestingly form an experimental point of view, the exchange field in the F layer.

In this section, we explore the importance that the geometry has on the successful realization of a phase battery. In Sec. 4.4.1 we introduce the model that describe these type of devices. In Sec. 4.4.2, we calculate the phase accumulated across a device without any interruption of the S layer, as the one shown in Fig. 4.14. In Sec. 4.4.3, we study the phase difference between two equal-size S islands, in terms of its size and the separation between them. Finally, in Sec. 4.4.3.1 we explore the possible enhancement of the phase accumulated across these phase batteries by periodically interrupting the S layer along the wire.

4.4.1 The model and main equations

Let us consider a two-layer structure in the diffusive limit with lateral dimensions much smaller than the superconducting coherence length, ξ_0, like the one shown in Fig. 4.13, below. The top layer is a superconducting (S) wire of width d_S, weakly coupled to a ferromagnetic metal (F) of width d_F on the bottom that presents a strong Rashba-like SOC concentrated in a narrow region of width d_{sc} around its lower interface. The wires extend along the x axis and it has a rectangular cross-section, where the stack is piled along the z axis and the width of the wire along the y axis is w. In the following sections we study different configurations where the S wire in the top is interrupted in different regions of the space.

In the S layer, the imaginary-frequency Usadel equation that governs the quasiclassical GF in spin × Nambu space, $\check{g}^S \equiv \check{g}(0 < z < d_S)$, reads

$$\partial_k \check{\mathcal{J}}_k^S(\boldsymbol{r}) + \frac{\sigma_n}{D}\left[\omega\hat{\tau}_3 + \Delta(\boldsymbol{r})e^{i\varphi(\boldsymbol{r})\hat{\tau}_3}\hat{\tau}_2,\ \check{g}^S(\boldsymbol{r})\right] = 0, \tag{4.58}$$

where,

$$\check{\mathcal{J}}_k^S(\boldsymbol{r}) \equiv -\sigma_n \check{g}^S(\boldsymbol{r})\partial_k \check{g}^S(\boldsymbol{r}), \tag{4.59}$$

is the bulk *matrix current* in the S wire, $\sigma_n = \nu(0)De^2/\hbar$ is the normal state Drude conductivity for a single spin specie, with $\nu(0)$ being the DOS at the Fermi level and D being the diffusion coefficient. Here, $\Delta(\boldsymbol{r})$ is the superconducting order parameter, $\varphi(x)$ stands for the superconducting phase, ω is the imaginary energy, $[\cdot,\cdot]$ stands for the commutation operation and $\hat{\tau}_{1,2,3}$ are the Pauli matrices spanning the Nambu space. In general, the superconducting order parameter equals $\Delta(\boldsymbol{r}) = \Delta$ in all the regions where the S wire is present and that the superconducting phase can change. As usual, in Eq. (4.58) we sum over repeated indices.

The weak coupling between the F and S layers generates small superconducting correlations in the F wire. Using the Usadel equation obtained in Refs. [61, 63, 64] for systems with SOC and small superconducting correlations, we can write the diffusion equation for the quasiclassical GFs in the F layer, $\check{g}^F(\boldsymbol{r}) \equiv \check{g}(-d_F < z < 0)$, as follows:

$$\partial_k \check{\mathcal{J}}^F_k(\boldsymbol{r}) + \frac{\sigma_n}{D}\left[\omega\hat{\tau}_3 + ih\hat{\sigma}^y\hat{\tau}_3,\ \check{g}^F(\boldsymbol{r})\right] = 0, \tag{4.60}$$

where,

$$\check{\mathcal{J}}^F_k(\boldsymbol{r}) = -\sigma_n \check{g}^F(\boldsymbol{r})\partial_k \check{g}^F(\boldsymbol{r}) + \frac{\sigma_{sc}(\boldsymbol{r})}{2}\epsilon_{kja}\left\{\hat{\sigma}^a, \partial_j \check{g}^F(\boldsymbol{r})\right\}, \tag{4.61}$$

is the bulk *matrix current* in the F wire. Here, $\hat{\sigma}^a$ are the Pauli matrices spanning spin space, h stands for the exchange field, which we consider to be homogeneous and pointing along the y direction, $\sigma_{sc}(\boldsymbol{r})$ is the microscopic value of the spin-to-charge conductance that accounts for the SOC in the interfacial region, which equals $\sigma^{mic}_{sc}(\boldsymbol{r}) = \sigma^{mic}_{sc}$ in a region of width d_{sc} around the interface and zero otherwise. The symbol ϵ_{kja} is the Levi-Civita or antisymmetric symbol and $\{\cdot,\cdot\}$ stands for the anti-commutation operation.

The interface between the S and F wires is described by the Kuprianov-Lukichev boundary conditions [135]:

$$\check{\mathcal{J}}^S_z\Big|_{z=0} = \check{\mathcal{J}}^F_z\Big|_{z=0} = -\frac{G_\square}{2}\left[\check{g}^F,\ \check{g}^S\right]_{z=0}, \tag{4.62}$$

where $G_\square$ is the conductance of the barrier between the S and F wires per unit of area. This equation couples the quasiclassical GFs in the F layer with those in the S layer. The condition for $G_\square$ in order to fulfill the weak coupling requirement will be discussed later in the text.

Using the bulk *matrix current*, we can calculate the charge current density flowing along the k direction in each layer,

$$ej^{S,F}_k(\boldsymbol{r}) = \pi i T\sum_{\omega_n}\frac{1}{4}\mathrm{Tr}\left[\hat{\tau}_3\check{\mathcal{J}}^{S,F}_k(\boldsymbol{r})\right], \tag{4.63}$$

where the trace runs over the spin × Nambu space, T is the temperature of the system and $\omega_n = (2n+1)\pi T$ are the Matsubara frequencies.

All the equations shown up to this point are written for the three-dimensional space. In the following, we take advantage of the small lateral dimensions of the structure to simplify the problem into a one-dimensional one.

4.4.1.1 Quasi-1D formulation

Given that the lateral dimensions of the wire are much smaller than the superconducting coherence length, ξ_0, one can assume that the quasiclassical GFs do not change across the wires' cross-section, *i.e.*, that $\check{g}^S(\boldsymbol{r}) = \check{g}^S(x)$ and $\check{g}^F(\boldsymbol{r}) = \check{g}^F(x)$. In that case, we can integrate Eqs. (4.58) and (4.60) over the lateral dimensions to obtain the following 1D Usadel equations:

$$\sigma_n \partial_x \left(\check{g}^S \partial_x \check{g}^S \right) + \frac{G_\square}{2d_S} \left[\check{g}^F, \check{g}^S \right] - \frac{\sigma_n}{D} \left[\omega \hat{\tau}_3 + \Delta e^{i\varphi \hat{\tau}_3} \hat{\tau}_2, \check{g}^S \right] = 0, \tag{4.64}$$

$$\partial_x \left(\sigma_n \check{g}^F \partial_x \check{g}^F + \frac{\sigma_{sc}}{2d_F} \left\{ \hat{\sigma}^y, \check{g}^F \right\} \right) + \frac{G_\square}{2d_F} \left[\check{g}^S, \check{g}^F \right] - \frac{\sigma_n}{D} \left[\omega \hat{\tau}_3 + ih \hat{\sigma}^y \hat{\tau}_3, \check{g}^F \right] = 0, \tag{4.65}$$

where the term under the partial derivative, ∂_x, are now the 1D *matrix currents* in the wires. In obtaining these equations, we used that the matrix current normal to the surfaces between the materials and the vacuum is zero at those surfaces.

The charge current flowing along the wires can be calculated from the 1D current matrices in the 1D Usadel equations above, using the integrated version of Eq. (4.63) across the cross section of the wires. This procedure results into a current flowing along the S and F wires that reads

$$eJ^S = -w d_S \pi i T \sum_{\omega_n} \frac{\sigma_n}{4} \mathrm{Tr} \left[\hat{\tau}_3 \check{g}^S \partial_x \check{g}^S \right], \tag{4.66}$$

$$\begin{aligned} eJ^F + eJ_{an} = \\ - w d_F \pi i T \sum_{\omega_n} \frac{\sigma_n}{4} \mathrm{Tr} \left[\hat{\tau}_3 \check{g}^F \partial_x \check{g}^F \right] - w \pi i T \sum_{\omega_n} \frac{\sigma_{sc}}{8} \mathrm{Tr} \left[\hat{\tau}_3 \{ \hat{\sigma}^y, \check{g}^F \} \right], \end{aligned} \tag{4.67}$$

respectively. In these equations, the term proportional to the trace of $\hat{\tau}_3 \check{g} \partial_x \check{g}$ is the usual diffusive current, and we label it as J^S and J^F in the S and F wires, respectively. In equilibrium, this term is proportional to the gradient of the superconducting phase, $\partial_x \varphi$, which let us identify it as a *supercurrent.*

In the superconducting wire, the *supercurrent* J^S is the only term that contributes to the current, Eq. (4.66). In the F wire, by contrast, there is one extra contribution to the current [Eq. (4.67)]: the *anomalous current*, J_{an}. The microscopic origin of this term, as explained in Ref. [85], has to do with the continuity condition of the current. The interplay between the SOC and exchange field at the bottom interface of the F region generates a microscopic current along the z direction [see $\check{\mathcal{J}}_k^F$ in Eq. (4.61)] that, as it cannot leak into the vacuum, bends

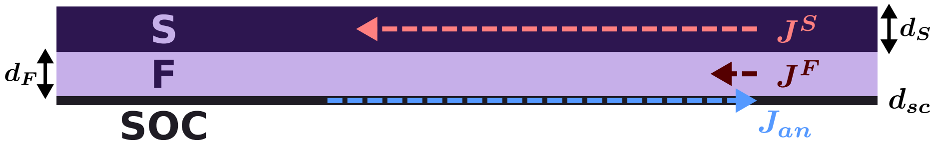

Figure 4.13: Pictorial representation of the base quasi-1D heterostructure studied in this section. A superconducting layer (S) of width d_S is grown on top of a ferromagnetic one (F) of width d_F, whose bottom interface presents strong spin-orbit coupling (SOC) over a small width $d_{sc} \ll d_s, d_F$. The interplay between the superconducting correlations, the exchange field and the SOC generates an anomalous charge current J_{an} (blue arrow) that flows along the bottom interface. To get a net charge current flowing along the wire, a phase gradient appears in the superconductor that generates a counter-flowing supercurrents both in S (light red arrow) and, via proximity effect, F (dark red arrow), J^S and J^F, respectively. Because we assume that the S and F layers are weakly coupled, then $J^S \gg J^F$.

into the x direction. This generates a current J_{an} localized at the lower boundary of F, where the interfacial SOC is present.

In a finite system, the total charge current flowing through any cross-section of the full structure must be zero, *i.e.*,

$$J^S(x) + J^F(x) + J_{an}(x) = 0. \tag{4.68}$$

This means that, when the interplay between SOC and the exchange field generates an anomalous current, $J_{an} \neq 0$, a counterflowing supercurrent is generated such that Eq. (4.68) holds, as shown in Fig. 4.13. The generation of such supercurrent implies a space-dependent phase, φ, which may result into a phase accumulation between the edges of the wire. Because the supercurrent is greater in those places where the superconducting condensate is stronger, most of it flows along the S wire, as indicated in Fig. 4.13. Moreover, the supercurrent is proportional to $\partial_x \varphi$ and, therefore, from direct inspection of Eqs. (4.66) and (4.67) one would expect that $d_S \partial_x \varphi \sim \sigma_{sc}/\sigma_n$ (we discuss this in more detail in Sec. 4.4.2). In known materials, $\sigma_{sc}/\sigma_n \ll 1$ [85, 86] and, consequently, the superconducting phase changes very slowly. In several works on spin-Hall effect the ratio that we use here is known as the *spin-Hall angle*, and they label it as $\theta = \sigma_{sc}/\sigma_n$.

In the following, we develop a method to solve the problem stated in this section for an arbitrary distribution of the top S wire. In doing so, we take advantage of the weak coupling between the S and F wires to linearize the 1D Usadel equation in F, Eq. (4.65).

4.4.1.2 General solution to the linearized problem

In previous sections we have stated that the interface between the S and F layers is resistive, which causes very weak leakage of the superconducting condensate into the ferromagnetic region. In the language of the quasiclassical GFs, such weak coupling means that the Nambu structure of $\check{g}^F$ can be written as follows:

$$\check{g}^F(x) \approx \begin{pmatrix} \mathrm{sign}(\omega) & \hat{f}(x) \\ \hat{f}^*(x) & -\mathrm{sign}(\omega) \end{pmatrix}, \tag{4.69}$$

where $|\hat{f}(x)| \ll 1$. The anomalous GF in Eq. (4.69) is a 2×2 matrix in spin space with the following parametrization

$$\hat{f}(x) = f_s(x) + i\mathrm{sign}(\omega) f_t(x)\hat{\sigma}^y. \tag{4.70}$$

Here, we know f_s and f_t as the singlet and triplet components of the anomalous GFs in the F wire, respectively.

Taking this in mind, we now solve the 1D Usadel equation in the S wire, Eq. (4.64). Up to zeroth order in the anomalous component of $\check{g}^F$, we obtain that the quasiclassical GF in the superconducting layer has trivial structure in spin space and reads,

$$\check{g}^S(x) = \begin{pmatrix} g^S(x) & -if^S(x)e^{i\varphi(x)} \\ if^S(x)e^{-i\varphi(x)} & -g^S(x) \end{pmatrix}, \tag{4.71}$$

where

$$g^S(x) = \frac{\omega + \frac{DG_\square}{2\sigma_n d_S}\mathrm{sign}(\omega)}{\sqrt{\left(\omega + \frac{DG_\square}{2\sigma_n d_S}\mathrm{sign}(\omega)\right)^2 + \Delta^2}}, \tag{4.72}$$

$$f^S(x) = \frac{\Delta}{\sqrt{\left(\omega + \frac{DG_\square}{2\sigma_n d_S}\mathrm{sign}(\omega)\right)^2 + \Delta^2}}. \tag{4.73}$$

To obtain these results we neglected terms proportional to $\partial_x^2\varphi$ because, as discussed above, the spatial change of the superconducting phase is very slow. In the very weak-coupling limit where $DG_\square/2\sigma_n d_S \ll \Delta$, the components of the GF in Eqs. (4.72) and (4.73) are approximately the BCS ones. In the following section we will see that this is indeed the case for situations where $d_S \sim d_F$ and $h \sim \Delta$.

In addition, we substitute the parametrization of $\check{g}^F$ in Eqs. (4.69) and (4.70) into the 1D Usadel equation, Eq. (4.65). Up to first order in f_s and f_t, we obtain the following system of equations for the different components of the quasiclassical GF:

$$\begin{cases} \Big(\partial_{xx} - \kappa_\omega^2\Big) f_s(x) + \Big(\kappa_h^2 + 2i\kappa_{sc}\partial_x\Big) f_t(x) = -i\frac{G_\square}{\sigma_n d_F} f^S(x) e^{i\varphi(x)} \\ -\Big(\kappa_h^2 + 2i\kappa_{sc}\partial_x\Big) f_s(x) + \Big(\partial_{xx} - \kappa_\omega^2\Big) f_t(x) = 0 \end{cases} . \tag{4.74}$$

These are the *linearized* Usadel equations in the F region. Here, we define the inverse lengths $\kappa_\omega^2 \equiv 2|\omega|/D$, $\kappa_h^2 \equiv 2h/D$ and $\kappa_{sc} \equiv \sigma_{sc}/2d_F\sigma_n$ and $f^S(x)$ equals the anomalous GF of the S wire, Eq. (4.73), in those x values where the top S layer is present and zero otherwise.

The charge currents flowing along the S and F wires, Eqs. (4.66) and (4.67), in the linearized problem respectively read,

$$eJ^S = -wd_S\frac{en_S(x)}{2m}\partial_x\varphi(x), \tag{4.75}$$

$$eJ^F = -wd_F\pi iT\frac{\sigma_n}{2}\sum_{\omega_n}\Big[f_s\partial_x f_s^* - f_t\partial_x f_t^* - c.c.\Big], \tag{4.76}$$

$$eJ_{an} = wd_F\pi iT\frac{\sigma_n}{2}\sum_{\omega_n}\Big[2i\kappa_{sc}f_s f_t^* - c.c.\Big]. \tag{4.77}$$

where $n_S(x)$ is the *superfluid density* [119] in the S layer defined as [Eq. (2.63)]:

$$\begin{aligned} \frac{en_S(x)}{2m} &\equiv \sigma_n\pi T\sum_{\omega_n}\left[f^S(x)\right]^2 \\ &= \sigma_n\frac{\pi\Delta}{4}\left[\tanh\left(\frac{\Delta + \frac{DG_\square}{2\sigma_n d_S}}{2T}\right) + \tanh\left(\frac{\Delta - \frac{DG_\square}{2\sigma_n d_S}}{2T}\right)\right]. \end{aligned} \tag{4.78}$$

Note that the expression under the summation sign in Eq. (4.76) is purely imaginary, which makes J^F a purely real quantity. To obtain this expression one has to consider the normalization condition of $\check{g}^F$.

In this section, we have stated the problem and we have obtained the expressions for the quasiclassical GFs in the S layer [Eqs. (4.71)–(4.73)], the system of equations from which the components of the quasiclassical GFs in the F wire can be obtained [Eqs. (4.74)] and the expressions for the current [Eqs. (4.75)–(4.78)]. In the following sections, we solve the problem for different configurations of the structure and discuss in each case the anomalous phase.

4.4.2 Homogeneous configuration

In this section, we consider a homogeneous S/F quasi-1D heterostructure of length L and with interfacial SOC at the bottom of the ferromagnetic layer, as the one shown in Fig. 4.13, and we estimate the phase accumulated along the wire for reasonable experimental values of the magnitudes involved in the problem.

Disregarding the edge effects at the ends of the wire, continuity of the charge current imposes the superconducting phase to fulfill a Laplace equation, $\partial_x^2 \varphi = 0$, *i.e.*, that the phase is linear in x. Therefore, the solution to the linearized Usadel equation in the F wire, Eq. (4.74), reads

$$f_s(x) \approx i \frac{G_\square}{\sigma_n d_F} \frac{\kappa_\omega^2}{\kappa_\omega^4 + \kappa_h^4} f^S e^{i\varphi(x)}, \tag{4.79}$$

$$f_t(x) \approx -i \frac{G_\square}{\sigma_n d_F} \frac{\kappa_h^2}{\kappa_\omega^4 + \kappa_h^4} f^S e^{i\varphi(x)}, \tag{4.80}$$

up to first order in $\kappa_{sc} \sim \partial_x \varphi$. The weak-coupling condition between the S and F wires that possibilities all the analysis carried here requires the absolute value of the prefactor multiplying $f^S e^{i\varphi}$ in the expressions of Eqs. (4.79) and (4.80) to be much smaller than one. Assuming that $h \sim \Delta$, this condition coincides with the one discussed below Eqs. (4.72) and (4.73), after substitution of d_S with d_F, namely, that $DG_\square/2\sigma_n d_F \Delta \ll 1$.

Thus, the supercurrent flowing along the F wire, Eq. (4.76), reads

$$eJ^F = -w d_F \frac{e n_F}{2m} \partial_x \varphi(x), \tag{4.81}$$

where the *superfluid density* in the F layer is defined as

$$\frac{e n_F}{2m} \equiv \sigma_n \pi T \left(\frac{G_\square}{\sigma_n d_F} \right)^2 \sum_{\omega_n} \frac{\kappa_\omega^4 - \kappa_h^4}{(\kappa_\omega^4 + \kappa_h^4)^2} \left(f^S \right)^2 \ll \frac{e n_S}{2m}. \tag{4.82}$$

Finally, the anomalous current flowing along the lower interface of the F wire reads

$$eJ_{an} = w \pi T \sigma_{sc} \left(\frac{G_\square}{\sigma_n d_F} \right)^2 \sum_{\omega_n} \frac{\kappa_\omega^2 \kappa_h^2}{(\kappa_\omega^4 + \kappa_h^4)^2} \left(f^S \right)^2 . \tag{4.83}$$

These expressions of the currents, together with the zero total current condition, $J^S + J^F + J_{an}$, provides us with an expression for the derivative of the phase that

Δ_0	D	σ_n	σ_{sc}	d_S	d_F	T
$150\ \mu eV$	$13\ eV \cdot nm^2$	$2 \times 10^5\ S/cm$	$50\ S/cm$	$2\ nm$	$2\ nm$	$25\ mK$

Table 4.1: Value of the parameters used in all the numerical calculations of this section, Sec. 4.4, unless otherwise indicated. The values of Δ_0, D, σ_{sc} and σ_{sc} are taken from Ref. [86]. These values result into an estimated diffusive superconducting coherence length of $\xi_0 = \sqrt{D/\Delta_0} \approx 300\ nm$.

reads,

$$\begin{aligned} \partial_x \varphi &= \left(\frac{G_\square}{\sigma_n d_F} \right)^2 \frac{\sigma_{sc} \pi T \sum_{\omega_n} \frac{\kappa_\omega^2 \kappa_h^2}{(\kappa_\omega^4 + \kappa_h^4)^2} \left(f^S \right)^2}{e(n_S + n_F)/2m} \\ &\approx 4 \frac{G_\square^2}{\sigma_n^2 d_S d_F} \frac{\sum_{\omega_n} \frac{\kappa_\omega^2 \kappa_h^2}{(\kappa_\omega^4 + \kappa_h^4)^2} \left(f^S \right)^2}{\tanh \frac{\Delta}{2T}} \kappa_{sc}, \end{aligned} \tag{4.84}$$

where to obtain the expression in the second line we neglected the proximity effect in n_S [the term summed to Δ in the hyperbolic tangents in Eq. (4.78)] and used that $n_S \gg n_F$. Both approximations are justified because of the small coupling between the S and F layers. Consequently, the phase accumulated across the wire of length L is given by the following expression:

$$\Delta \varphi = \partial_x \varphi L \approx \left[4 \frac{G_\square^2}{\sigma_n^2 d_S d_F} \frac{\sum_{\omega_n} \frac{\kappa_\omega^2 \kappa_h^2}{(\kappa_\omega^4 + \kappa_h^4)^2} \left(f^S \right)^2}{\tanh \frac{\Delta}{2T}} \right] \kappa_{sc} L. \tag{4.85}$$

Here, the expression multiplying L in the r.h.s. is the phase gradient and for $h \sim \Delta$ it is expected to be of the order of $\partial_x \varphi \sim \frac{G_\square^2 D^2}{\sigma_n^2 \Delta^2 d_S d_F} \kappa_{sc}$. Because the weak-coupling between the S and F layers condition reads $(G_\square D)(2\sigma_n \Delta d_F) \ll 1$, in systems with similar widths of the S and F layers the gradient of the phase fulfills $\partial_x \varphi / \kappa_{sc} \ll 1$.

In Fig. 4.14, we show the dependence of the superconducting phase gradient, $\partial_x \varphi$, in terms of the exchange field in the F layer, h, for the parameter values shown in Table 4.1 and a weak coupling between the S and F layers mediated by the conductance per unit of area $\frac{G_\square}{\sigma_n} = 0.1 \frac{2 d_F \Delta}{D} \approx 4.5\ \mu m^{-1}$. In Table 4.1, we take the values of Δ_0, D, σ_n and σ_{sc} from the estimations obtained by the authors of Ref. [86] for a similar structure. Although in that particular work the SOC was generated by embedded impurities in the bulk of the wire, other experiments on spintronic effects with layered materials showing interfacial SOC show similar values of σ_{sc} [260, 85, 86]. The superconducting coherence length resulting from

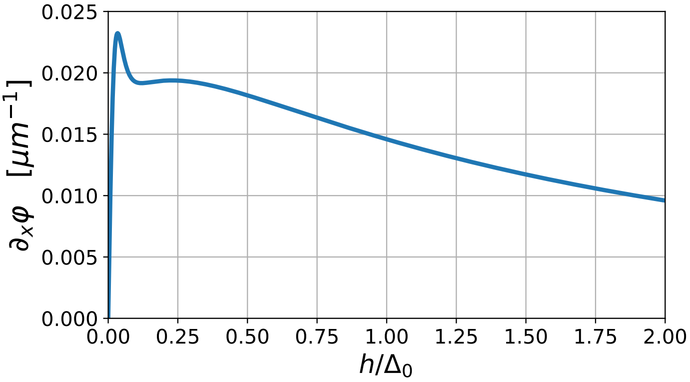

Figure 4.14: Gradient of the superconducting phase, $\partial_x \varphi$ [Eq. (4.85)], in terms of the exchange field in the F layer, h, for the configuration shown in Fig. 4.13. We take the values of the parameters shown in Tab. 4.1 and a coupling between the F and S layers mediated by $\frac{G_\square}{\sigma_n} = 0.1\frac{2d_F\Delta}{D} \approx 4500\,m^{-1}$. In order to obtain a phase difference of $\Delta\varphi \sim 1$, the wire should have a length $L \sim 50\ \mu m$, which exceeds ξ_0 by an order of magnitude.

this values in the diffusive wire is $\xi_0 \sim \sqrt{D/\Delta_0} \approx 300\ nm$. We choose this value as the maximum length of our phase battery, as in longer wires phase decoherence suppresses the Josephson coupling.

The results shown for $\partial_x \varphi$ in Fig. 4.14 suggest that, to obtain phase differences of the order of $\Delta\varphi \sim 1$ between the ends of the wire, the length of the phase battery should be of $L \sim 50\ \mu m \gg \xi_0$. Thus, the structure shown in Fig. 4.13 is not a suitable geometry for a phase battery. The high *superfluid density* in the superconductor, n_S [Eq. (4.78)], permits the generation of a supercurrent equal in magnitude and opposite to the anomalous current with a small value of $\partial_x \varphi$ [see Eq. (4.75)]. Because in the F layer the *superfluid density* induced from the S layer is much smaller than in the latter, $n_F \ll n_S$, we expect that the gradient of the phase would greatly increase if the superconducting layer is interrupted along a region. This is considered in the next section.

4.4.3 Two island configuration

In the previous section, we have seen that the phase accumulation in a quasi-1D structure consisting on a S layer weakly coupled to a F layer with superficial SOC is too small. In that case, the obtained expression for $\partial_x \varphi$ shows a common denominator proportional to $n_S + n_F$ [see the first line in Eq. (4.84)], where n_S and

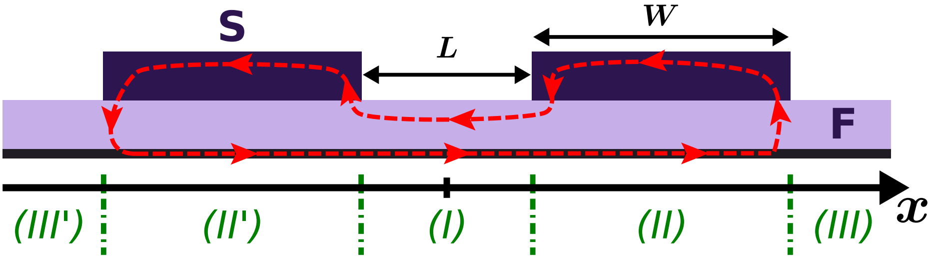

Figure 4.15: Sketch of the two-island configuration studied in Sec. 4.4.3, where two S islands of width W are separated by a gap of length L. The green roman numbers below the x axis are the labels of the different regions in which we split the space (see the text for more information). The red arrow is a pictorial representation of the charge current profiles flowing along the structure. In the regions with S islands are present, the supercurrent that counter-flows J_{an} mainly flows along the S layer, resulting into a negligible phase accumulation. In the region between the islands, however, the supercurrent can only flow along the F wire that, due to the weak coupling between the S and F layers, generates a big phase gradient. This results into a phase difference φ_0 between the borders of the interruption.

n_F are the *superfluid densities* in the S and F layers, respectively. Because $n_S \gg n_F$, one expects that if interrupting the top S layer along a given distance, L, would highly increase the accumulated phase across the interruption (due to the fact that $n_S = 0$ in that region). In Ref. [63], the authors exploited this idea to calculate the jump in the superconducting phase happening across an interruption of the S layer in an otherwise infinite system. They predicted non-negligible phase accumulation across the borders of the interruption for reasonable values of L. In Ref. [86], an experimental realization of such a system confirmed a sizable accumulation of phase across an interruption of $\sim 100nm$.

In this section, we study the slightly different configuration shown in Fig. 4.15. It consists on an infinite F layer of width d_F and with interfacial SOC at the bottom, weakly coupled to two overlying superconducting island of equal width, W, and separated by a distance L. In the upcoming analysis, we split the space along the x direction in the five regions indicated in Fig. 4.15. These regions correspond to (*I*) $-L/2 < x < L/2$, (*II*) $L/2 < x < L/2 + W$, (*III*) $L/2 + W < x$, and the *primed* regions, (*II*') and (*III*'), that are related to the non-primed ones, (*II*) and (*III*), after $x \longrightarrow -x$ substitution.

In the regions II and II', the top superconducting layer is present and, hence, the superconducting phase is well defined. Due to symmetry considerations, we impose that

$$\varphi(x) = \begin{cases} -\varphi_0/2 + \delta\varphi(x) & \text{in region } II' \\ \varphi_0/2 + \delta\varphi(x) & \text{in region } II \end{cases}, \tag{4.86}$$

where $\delta\varphi(x)$ is a small correction to φ_0, as we expect from the discussion at the beginning of this section. The symmetry of the system allows us to find an odd solution for the superconducting phase that fulfills $\varphi(-x) = -\varphi(x)$. We can gauge out this correction to the phase from the 1D Usadel equation in the F layer, Eq. (4.74), by explicitly writing it in the singlet and triplet components of the quasiclassical GF, $f_s(x) = \tilde{f}_s(x)e^{i\delta\varphi(x)}$ and $f_t(x) = \tilde{f}_t(x)e^{i\delta\varphi(x)}$, and then neglecting the $\partial_x\delta\varphi$ terms from the Usadel equation. This process allows us to write Eq. (4.74) in the following way:

$$\begin{cases} (\partial_x + \kappa_{sc})^2\tilde{f}_+ - q^2\tilde{f}_+ = \tilde{S}(x) \\ (\partial_x - \kappa_{sc})^2\tilde{f}_- - (q^*)^2\tilde{f}_- = \tilde{S}(x) \end{cases}, \tag{4.87}$$

where,

$$\tilde{S}(x) = -i\frac{G_\square}{\sigma_n d_F}f^S\Big\{ e^{i\varphi_0/2}\big[\theta(x - L/2) - \theta(x - L/2 - W)\big] \\ + e^{-i\varphi_0/2}\big[\theta(-x - L/2) - \theta(-x - L/2 - W)\big]\Big\}. \tag{4.88}$$

is the inhomogeneous part of the system of differential equations and f^S is the anomalous GF in the S layer, shown in Eq. (4.73). To obtain Eq. (4.87), we defined the *plus* and *minus* components of the anomalous GF in the ferromagnet as

$$f_+ \equiv f_s + if_t, \tag{4.89}$$

$$f_- \equiv f_s - if_t, \tag{4.90}$$

and the inverse length:

$$q \equiv \sqrt{\kappa_\omega^2 + \kappa_{sc}^2 + i\kappa_h^2}. \tag{4.91}$$

In Eq. (4.87) the system of equations is already decoupled. Thus, we can solve it for $f_+(x)$ and, then, directly obtain the expression for $f_-(x)$ by making the substitutions $\kappa_{sc} \longrightarrow -\kappa_{sc}$ and $q \longrightarrow q^*$. We first solve the resolvent[6] of the differential equation for f_+,

$$\left[(\partial_x + \kappa_{sc})^2 - q^2\right]K_+(x - x') = \delta(x - x'), \tag{4.92}$$

---

[6] Here, we use the term *resolvent* instead of *Green's function* to avoid misunderstandings with the GFs that we have been working with all along this thesis.

that reads,

$$K_+(x-x') = -\frac{e^{-q|x-x'|}e^{-\kappa_{sc}(x-x')}}{2q} \ , \tag{4.93}$$

in terms of which we can obtain the *plus* component of the GF by computing the following integral:

$$f_+(x) = \int_{-\infty}^{\infty} dx' K_+(x-x')S(x'). \tag{4.94}$$

From the relation between the first and second differential equation in Eq. (4.87) it follows that

$$K_-(x-x') = -\frac{e^{-q^*|x-x'|}e^{\kappa_{sc}(x-x')}}{2q}. \tag{4.95}$$

$f_-(x)$ can be computed in the same way as Eq. (4.94), *i.e.*, $f_-(x) = \int_{-\infty}^{\infty} dx' K_-(x-x')S(x')$.

In terms of the new defined components, f_+ and f_- in Eqs. (4.89) and (4.90), the sum of the supercurrent flowing along the F wire and the anomalous current flowing along the interface with strong SOC compactly reads:

$$eJ^F + eJ_{an} = wd_F \pi T \sigma_n \frac{1}{2} \sum_{\omega_n} \mathrm{Im}\left[f_+(\partial_x - \kappa_{sc})f_-^* + f_-(\partial_x + \kappa_{sc})f_+^*\right]. \tag{4.96}$$

In the following sections, we use Eqs. (4.93)–(4.95) to calculate f_+ and f_- in each one of the regions *I*, *II* and *III*. We then calculate the total current flowing through the cross section of the structure using Eq. (4.96) [and Eq. (4.75), when necessary]. Continuity of the current requires the net current flowing through the cross-section of the structure at any x position to be zero. Therefore, wecan find the value of the phase jump, φ_0, occurring between the superconducting islands, , and the evolution of the phase in the regions where the S wire is present, $\delta\varphi(x)$.

Region I: the phase jump, φ_0

In the region between the islands, $|x| < L/2$, the integral shown in Eq. (4.94) results into

$$f_+(x) = i\frac{G_\square f^S}{\sigma_n q d_F}\left[\frac{e^{-i\varphi_0/2}e^{-(q+\kappa_{sc})(L+W)/2}\sinh\frac{(q+\kappa_{sc})W}{2}}{q+\kappa_{sc}}e^{-(q+\kappa_{sc})x}\right.$$
$$\left.+\frac{e^{i\varphi_0/2}e^{-(q-\kappa_{sc})(L+W)/2}\sinh\frac{(q-\kappa_{sc})W}{2}}{q-\kappa_{sc}}e^{(q-\kappa_{sc})x}\right]. \tag{4.97}$$

The expression for $f_-(x)$ can be obtained from the equation above, after making the following substitutions: $\kappa_{sc} \longrightarrow -\kappa_{sc}$ and $q \longrightarrow q^*$.

As in this region there is no S wire, the total current flowing along the structure at $x = 0$ reads:

$$eJ^F(0) + eJ_{an}(0) = -wd_F\pi T\sigma_n\left(\frac{G_\square}{\sigma_n d_F}\right)^2\sum_{\omega_n}\mathrm{Im}\left\{(f^S)^2 e^{i\varphi_0}\right.$$
$$\left.\times\left[\frac{e^{-(q-\kappa_{sc})(L+W)}\sinh^2\frac{(q-\kappa_{sc})W}{2}}{q(q-\kappa_{sc})^2}+\frac{e^{-(q^*+\kappa_{sc})(L+W)}\sinh^2\frac{(q^*+\kappa_{sc})W}{2}}{q^*(q^*+\kappa_{sc})^2}\right]\right\}. \tag{4.98}$$

Therefore, to obtain the zero current condition expression under the summation symbol has to be purely real. Inserting the summation into the imaginary-part function and taking $e^{i\varphi_0}$ as a common factor, one immediately sees that there is no current flowing across the interruption when,

$$\varphi_0 = -\arctan\left\{\frac{\sum_{\omega_n}(\tilde{f}^S)^2\mathrm{Im}\left[\frac{e^{-(q-\kappa_{sc})(L+W)}\sinh^2\frac{(q-\kappa_{sc})W}{2}}{q(q-\kappa_{sc})^2}+\frac{e^{-(q^*+\kappa_{sc})(L+W)}\sinh^2\frac{(q^*+\kappa_{sc})W}{2}}{q^*(q^*+\kappa_{sc})^2}\right]}{\sum_{\omega_n}(\tilde{f}^S)^2\mathrm{Re}\left[\frac{e^{-(q-\kappa_{sc})(L+W)}\sinh^2\frac{(q-\kappa_{sc})W}{2}}{q(q-\kappa_{sc})^2}+\frac{e^{-(q^*+\kappa_{sc})(L+W)}\sinh^2\frac{(q^*+\kappa_{sc})W}{2}}{q^*(q^*+\kappa_{sc})^2}\right]}\right\}. \tag{4.99}$$

In Fig. 4.16, we show the phase accumulated across the interruption, Eq. (4.99), in terms of the exchange field in the F layer, for a fixed separation between the S islands of $L = 100\ nm$ and different widths of the islands, W (different lines withing each panel). The values of the remaining parameters are those shown in Tab. 4.1. The left and right panels differ in the range of values of h. As it is shown in the figure, increasing h increases the phase, φ_0, slowly (see the right panel of the figure) up to a point where its value rapidly changes from $\varphi_0 \approx 0$ to $\varphi_0 \approx \pi$. The position of the transitions shifts towards lower values of h with increasing

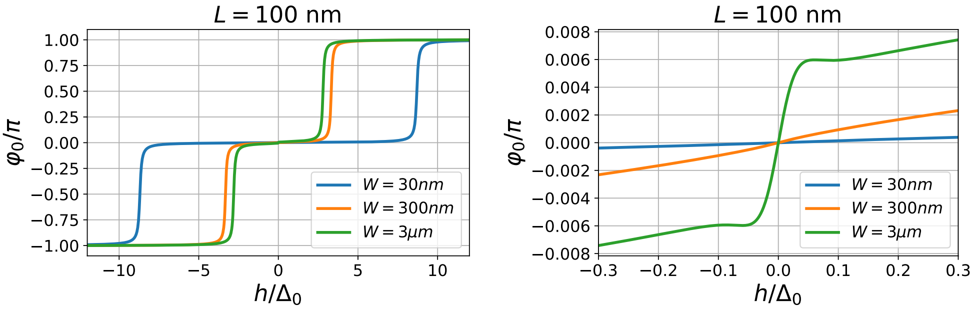

Figure 4.16: Phase accumulated across the interruption, φ_0 [Eq. (4.99)], in terms of the exchange field in F, h for different widths of the islands, W, and a fixed separation between the S regions of $L = 100\ nm$. The value of the remaining parameters are those shown in Table 4.1.

W. Further increase of h (beyond the limits shown in the left panel of Fig. 4.16) shows more transitions where the value of φ approximately increases by π. The sharp shape of the transitions shown in Fig. 4.16 make it difficult to use these devices as phase batteries, because a very fine tuning of h is required to obtain a value of φ_0 that would generate a sizable Josephson current in a superconducting circuit, *i.e.*, that $|\cos\varphi_0| \ll 1$. This problem could be overcome by increasing strength of the interfacial SOC (*i.e.*, by increasing κ_{sc}), as that would soften the transitions.

In Fig. 4.17, we show the phase accumulated across the interruption, φ_0, in terms of the separation between the S islands, L, for a fixed value of the exchange field in the F layer of $h = 5\Delta_0$ and different island sizes, W (different lines within each panel). The remaining parameters are chosen according to Table 4.1. As shown in the inset, at $L \longrightarrow 0$, the accumulated phase presents a small but non-zero value that monotonically increases with L. The value of the $\lim_{L\to 0}\varphi_0$ gets bigger with wider superconducting islands. In a similar way as it happened with the dependence of φ_0 with h in Fig. 4.16, the dependence of φ_0 with L is similar to a staircase. The value of the accumulated phase approximately changes by π is a small range of L values, whereas in the remaining values of L it barely changes. The position these transitions happen shift towards lower values of L with increasing width of the islands, W. The transition can be smoothed by increasing the value of κ_{sc}.

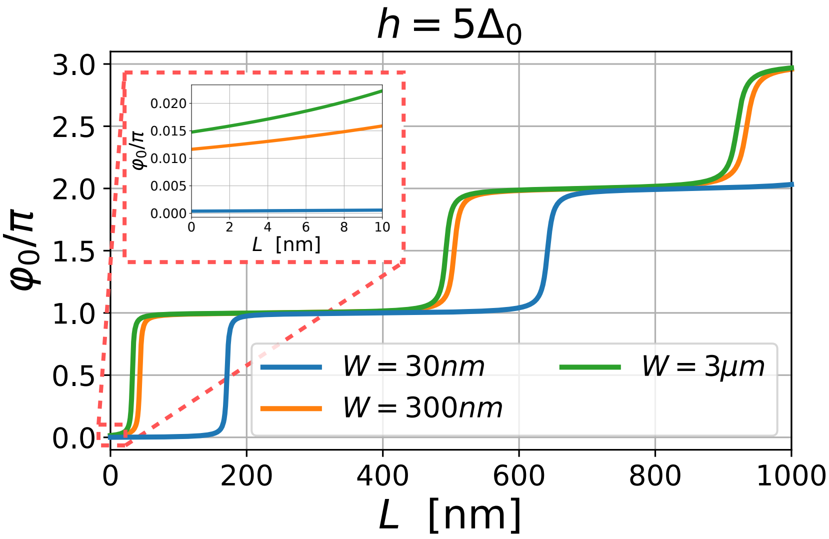

Figure 4.17: Phase accumulated across the interruption, φ_0 [Eq. (4.99)], in terms of the separation between the S islands, L, for different widths, W, in the configuration shown in Fig. 4.15. We fix a value of $h = 5\Delta_0$ and set the value of the remaining parameters according to Table 4.1. The inset shows a zoom of the area indicated with the small dashed red rectangle.

Region *II*: the evolution of the phase, $\delta\varphi(x)$

Below the superconducting island, $L/2 < x < L/2 + W$, the gauge-transformed *plus* component of the GF in the F wire reads,

$$\tilde{f}_+(x) = i\frac{G_\square f^S}{2\sigma_n q d_F}\left\{\left[e^{-i\varphi_0/2}e^{-(q+\kappa_{sc})L/2}\left(1-e^{-(q+\kappa_{sc})W}\right) - e^{i\varphi_0/2}e^{(q+\kappa_{sc})L/2}\right]\frac{e^{-(q+\kappa_{sc})x}}{q+\kappa_{sc}} \right.$$
$$\left. - e^{i\varphi_0/2}e^{-(q-\kappa_{sc})(W+L/2)}\frac{e^{(q-\kappa_{sc})x}}{q-\kappa_{sc}} + \frac{2qe^{i\varphi_0/2}}{(q-\kappa_{sc})(q+\kappa_{sc})}\right\}. \tag{4.100}$$

As usual, the expression for $f_-(x)$ is obtained from this one after the substitutions: $\kappa_{sc} \longrightarrow -\kappa_{sc}$ and $q \longrightarrow q^*$. In this case, the full expression of the current flowing along the F wire is quite complicated.

From conservation of the current it follows that the zero-current conditions holds all along x, $J^S(x) + J^F(x) + J_{an}(x) = 0$. Recalling the gauge transformation that we made to f_+ and f_- before Eq. (4.87), the correction to the superconducting phase φ_0 in Eq. (4.86) that ensures such absence of current reads,

$$\delta\varphi(x) = \frac{d_F}{2}\int_{L/2}^{x} dx' \frac{\sum_{\omega_n} \mathrm{Im}\left[\tilde{f}_+(x')(\partial_{x'} - \kappa_{sc})\tilde{f}_-^*(x') + \tilde{f}_-(x')(\partial_{x'} + \kappa_{sc})\tilde{f}_+^*(x')\right]}{e(d_S n_S + d_F n_F(x'))/2m}. \tag{4.101}$$

where n_S is the *superfluid density* in the S layer given in Eq. (4.78) and the *superfluid density* in the F wire in terms of f_+ and f_- reads,

$$\frac{e n_F(x)}{2m} \equiv \sum_{\omega_n} \mathrm{Re}\left[f_+(x) f_-^*(x)\right]. \tag{4.102}$$

Due to the weak coupling between the S and F layers, the superconducting condensate is much more dense in the superconductor, *i.e.*, $n_S \gg n_F$. This allows us to neglect the $n_F(x')$ term in the denominator of Eq. (4.101). Thus, the correction to the phase for $h \sim \Delta$ is, roughly, of the order of $\delta\varphi(x) \sim \frac{G_\square^2 D^2}{\sigma_n^2 \Delta^2 d_F^2}\kappa_{sc} W$, which coincides with the estimated magnitude of the phase accumulated in an equal-length structure without interruption of the S layer, studied in Sec. 4.4.2. According to the results of that section, the correction to the phase along a S island of width $W \leq \xi_0$ is negligible, $\delta\varphi(L/2 + W) \ll 1$, which is confirmed from numeric calculation of Eq. (4.101). This result suggests that in a periodic arrangement of these islands, the total phase accumulated along the quasi-1D structure is equal to the sum of the accumulated phase at each one of the interruptions. We present a preliminary study of these system in Sec. 4.4.3.1.

Region *III*: a consistency check

At the external parts of the structure, $x > L/2 + W$, the *plus* component of the GF in the F wire reads,

$$f_+(x) = i\frac{G_\square \tilde{f}^S}{\sigma_n d_F}\frac{e^{-(q+\kappa_{sc})x}\sinh\frac{(q+\kappa_{sc})W}{2}}{q(q+\kappa_{sc})}\left[e^{-i\varphi_0/2}e^{-(q+\kappa_{sc})(L+W)/2} + e^{i\varphi_0/2}e^{(q+\kappa_{sc})(L+W)/2}\right]. \tag{4.103}$$

Substituting κ_{sc} and q with $-\kappa_{sc}$ and q^*, respectively, we would obtain the expression for f_-. From these expressions one can easily check that

$$\mathrm{Im}\left[f_+(\partial_x - \kappa_{sc})f_-^* + f_-(\partial_x + \kappa_{sc})f_+^*\right] = 0. \tag{4.104}$$

Therefore, there is no current flowing along the section *III* (and, hence, there is no current in region *III'* either). This result serve as a consistency check for the analysis carried in the whole section.

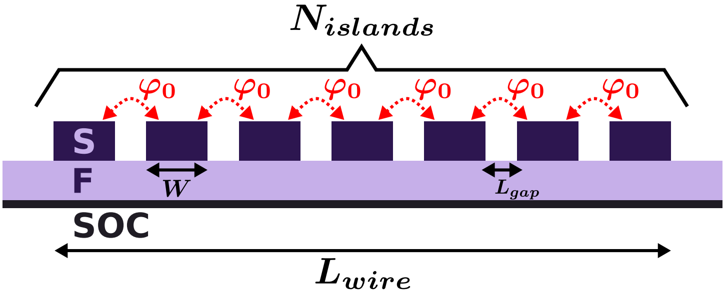

Figure 4.18: An array of $N_{islands}$ superconducting islands of width W and separated by a distance L_{gap} on top a F layer whose with SOC at the bottom interface. The total length of the wire is L_{wire}. Through each of the interruptions between consecutive islands a superconducting phase φ_0 is accumulated, which results into a total phase accumulation along the wire of $\varphi_0^{wire} \approx (N_{islands} - 1)\varphi_0$.

4.4.3.1 Concatenation of many islands

In previos sections we calculated the phase difference, φ_0, between two S islands of width W and separated by a distance L on top of a F wire with interfacial SOC on the opposite surface, Eq. (4.99). We found that the value of φ_0 increases with increasing values of W, L and the exchange field in the F layer, h. As seen in the inset of Fig. 4.17, for $h \neq 0$,the phase difference between the islands is finite even at $L \longrightarrow 0$. This, suggests that the phase accumulated between the ends of a phase battery of fixed length may be enhanced by increasing the number of S islands laying in-between.

Let us consider a structure like the one shown in Fig. 4.18. It consists of an array of $N_{islands}$ superconducting islands of width W and separated by a distance L_{gap} on top a the F with interfacial SOC. The total length of the phase battery reads,

$$L_{wire} = N_{islands} W + (N_{islands} - 1)L_{gap}. \tag{4.105}$$

Because according to the discussion below Eq. (4.102), the change of the superconducting phase within each islands remain almost constant, the total phase accumulated across the phase battery, φ_0^{wire}, equals the sum of the phase jumps at each interruption. Here, we assume that the accumulated phase between each pair of subsequent S islands is equal, and we approximate it by its value in the isolated two-island configuration, φ_0. Therefore, the phase difference between the ends of the wire reads,

$$\varphi_0^{wire} \approx (N_{islands} - 1)\varphi_0, \tag{4.106}$$

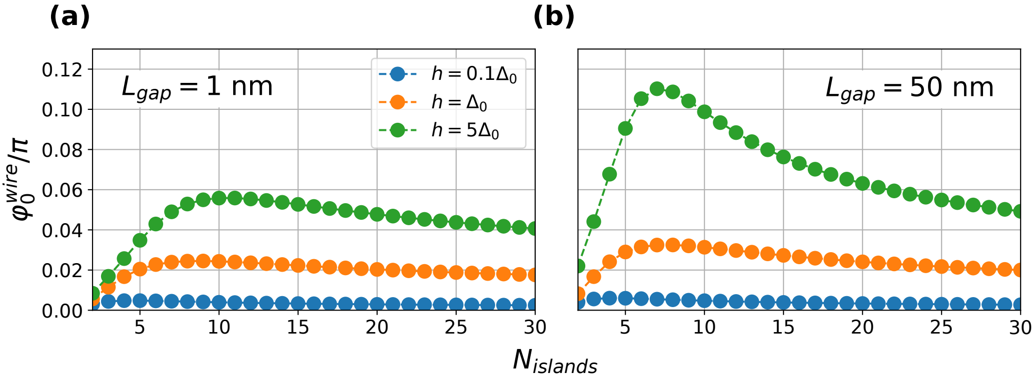

Figure 4.19: Total phase accumulated across the structure in Fig. 4.18 in terms of the number of islands, N, for differeng values of the exchange field in the F layer, h [Eq. (4.106)]. The total length of the structure is $L_{wire} = 3\ \mu m$ and the separation between islands equals (a) $L_{gap} = 1\ nm$ and (b) $L_{gap} = 50 nm$. The rest of parameters are fixed according to Tab. 4.1.

where φ_0 is given by Eq. (4.99). In Fig. 4.19 we show the value of φ_0^{wire} in terms of the number of islands, $N_{islands}$, for different values of the exchange field in the F layer, h. The total length of the structure is $L_{wire} = 3\ \mu m$ and we set the separation between the islands to $L_{gap} = 1 nm$ and $L_{gap} = 50 nm$ in Fig. 4.19a and Fig. 4.19b, respectively. For other parameters we use the values in Table 4.1. For fixed values of L_{wire} and L_{gap}, the increase of $N_{islands}$ involves decreasing the size of the islands, W, which results in the nonmonotonic dependence of Eq. (4.106) with $N_{islands}$ shown in Fig. 4.19.

The phase difference between the ends of the wire increases with increasing h and it has a maximum at a given number of islands that, for the cases shown in Fig. 4.19, lays around five to ten islands. The position and value of the maximum $\varphi_0^{wire}(N_{islands})$ depends on both h and the size of the gap between the islands, L_{gap}. In any case, the interruption of the S-wire always enhances the phase battery capability of the device in comparison to the non-interrupted situation, $N_{islands} = 1$. In the cases shown in Fig. 4.19, the value of φ_0^{wire} for the optimum value of $N_{islands}$ is around five times larger than φ_0^{wire} for $N_{islands} = 1$.

The results presented in Fig. 4.19 are obtained under the assumption that the phase accumulated between every two consecutive islands is given by Eq. (4.99). Therefore, these results should be taken as what they are: a prediction about the potential of a system with the geometry shown in Fig. 4.18 to be used as a Josephson phase battery. Such prediction motivates future research to obtain the phase difference between the borders of each gap following the same method developed in Sec. 4.4.3. Specifically, it would be interesting to slightly modify the geometry of the system to consider semi-infinite S islands at the ends of the wire that would serve as the "battery terminals".

It is important to emphasize that all results in Sec. 4.4 are obtained without taking into account spin-relaxation processes due to the SOC [the Σ_{so} term in the Usadel equation, Eq. (2.50) or Eq. (4.6)]. This approximation allowed us to obtain analytic expressions of the GFs, not possible in other case. Including a $\Sigma_{so} \neq 0$ term in the Usadel equation, Eq. (4.60), decreases the spin polarization caused by the exchange field [31, 32, 215], which ultimately decreases the phase difference between the battery terminals. Thus, the φ_0 values obtained in this section are the upper bound in a best-case scenario. The effect of such relaxation terms can be considered by including them into the Usadel equation in the superconductor, Eq. (4.64), and obtaining numerical solution of the GFs, $\check{g}^S$, in the same way we did in Sec. 4.2.

Chapter 5

Summary and Conclusions

In this thesis, we studied the interplay between superconducting correlations and spin-dependent fields in different heterostructures. The different hybrid systems that we considered all along the thesis can be classified into two groups, which form Chapter 3 and Chapter 4, respectively. In Chapter 3 we focus on quasi-one-dimensional (quasi-1D) superconducting systems with magnetic impurities in the ballistic limit and study their spectral properties. By contrast, in Chapter 4 we explore layered systems, where the proximity effect between different superconducting (S), ferromagnetic (F), metallic (N), etc., stacked films provides the device with unique properties that make them suitable for various applications. In what follows, we provide a summary of the main conclusions of the thesis.

In Sec. 3.1, we demonstrate that the total spin of a superconducting system in presence of a collinear spin-dependent field undergoes integer jumps in units of $\hbar/2$ associated with the clsoing of the superconducting gap. The spin-dependent field may describe magnetic impurities in a superconductor or homogeneous exchange fields, and the gap closure can be caused by zero-energy crossings of bound states. We present two alternative demonstrations of such behavior of the spin polarization: the first one (Sec. 3.1.1) in the form of a generalized Friedel sum rule, and the second one (Sec. 3.1.2) in terms of the *spectral asymmetry index*, a quantity used in topology, quantum field theory and condensed matter physics. In this thesis, we used these two relations only in (quasi-)1D systems. However, both demonstrations are general and also apply for 3D systems.

In Sec. 3.2, we present a complete study of equilibrium properties of a superconducting wire with a magnetic defect. We derive a general expression, Eq. (3.18), that determines the full subgap spectrum provided that the T-matrix of the F region in the normal state is known. Specifically, we analyze the spectrum of a one-dimensional ballistic SFS Josephson with a F region smaller than the superconducting coherence length but arbitrary strength of the exchange field. Our theoretical analysis bridges nicely two previously disconnected limiting cases: the Yu-Shiba-Rusinov (YSR) and the semiclassical ones. We demonstrate that the quantum phase transition predicted by the YSR model can be also found for SFS junctions of finite length, L. Such phase transitions are associated not only to the integer jumps of the total spin described by the generalized Friedel sum rule that we derived in Sec. 3.1.1, but also to a change of the sign of the supercurrent. To obtain a more realistic description of an impurity in a superconductor, further research can be done in extending this model to higher dimensions and/or weak disorder in the media.

In Sec. 3.3, we introduce the concept of quasi-1D helical *Andreev crystals* (ACs), *i.e.* a periodic arrangement of semiclassical magnetic regions separated by a constant distance, a, where the strength of the exchange field of the semiclassical impurities is given by the *magnetic phase*, Φ, and its direction rotates a constant angle 2α between consecutive regions. In Sec. 3.3.2, we present a full analysis of the spectral properties of these quasi-1D helical ACs and junctions between them when the separation between the impurities is much larger than the superconducting coherence length, $a \gg \xi_0$. For energies within the superconducting gap, the spectrum of helical ACs exhibits a pair of energy-symmetric Andreev bands with respect to the Fermi level. In ferromagnetic ACs ($\sin\alpha = 0$) the gap between the Andreev bands closes in a finite range of Φ values around half-integer values of Φ/π (See Fig. 3.6 for the meaning of α and Φ). The range of Φ values for which the gap remains closed increases with decreasing separation between impurities, a. Otherwise, $\sin\alpha \neq 0$, the gap closes only at half-integer values of Φ/π, forming a Dirac point. Inverted junctions of helical ACs may present a pair of states bounded to the interface. These states (always) never appear in inverted junctions of (anti)ferromagnetic ACs, whereas they more likely appear as the rotation of the ACs forming the inverted junction approaches an antiferromagnetic configuration (*i.e.*, with decreasing value of $|\cos\alpha|$).

In Sec. 3.3.3, we go beyond the tight-binding up to first neighbours approximation considered in the previous section and show a method to solve the Eilenberger equation of infinite and junctions between semi-infinite ACs. Because (anti-)ferromagnetic ACs best exemplify the (existence) absence of interfacial states in inverted junctions between them, we apply this method to compute the full quasiclassical GFs of chains and junctions with collinear magnetization of the impurities. Our calculations are exact and generalizes the results of the previous sections for arbitrary distance between the impurities, namely, that the gap around the Fermi level in antiferromagnetic ACs only closes at half-integer values of Φ/π and that junctions between different antiferromagnetic ACs exhibit states bounded to the interface when the gap gets inverted through the junction. From the quasiclassical GFs we calculate the surface spin polarization and demonstrate that such inverted junctions show fractionalization of the surface spin. The method that we present to solve the Eilenberger equation of collinear ACs and junctions between them can be generalized for more complex magnetic configurations.

Overall, the results shown in Sec. 3.3 suggest the use of superconductor–ferromagnetic structures to realize crystals of a mesoscopic scale. We predict a diversity of properties of such ACs, as gap inversion and edge states, that can be proved by state-of-the-art spectroscopic techniques. Given the ballistic nature of the studied system, experimental observation of the predicted properties requires the use of clean materials where the mean free path is larger than the superconducting coherence length, $\ell > \xi_0$. The spectrum and, in particular, the bound states formed at the interface between two ACs can be measured by a local tunneling probe. With magnetic probes one may also determine the spin-polarization of such states. Future works may explore the extension of these ACs to higher dimensions and the effect that weak disorder has on the obtained results.

In Sec. 4.1, we introduce the theoretical model used in the study bilayers between a superconductor (S) and a ferromagnetic insulator (FI). The spin-dependent scattering at the S/FI interface leads to an effective exchange field in the S, which shows as a spin splitting in the superconducting density of states (DOS). When the FI is used as a tunneling barrier between two electrodes, its spin polarization makes it an effective spin-filter of the current. In addition to these two effects, we include the effect of SOC, spin-flipping events and orbital depairing processes, and provide a complete model for the description of real systems. This model is used in some other sections of this thesis to accurately describe experimental data on devices with S/FI heterostructures.

In Sec. 4.2, we present an exhaustive analysis of tunnel junctions between spin-split superconductors coupled via a spin-polarized barrier. With the help of the theoretical model developed in the previous section, we compute the spectral properties of the S/FI electrodes and determine the current through a FI/S/I/FI/I/S/FI junction, where the middle FI layer serves as a spin-filter. Our theory predicts a previously unknown behavior of the differential tunneling conductance when the FI layers are non-collinear. Moreover, we suggest how to use these structures for the realization of so-called φ_0-junctions. In addition, our theory provides an accurate description of the differential conductance measurements of an EuS/Al/AlO$_x$/EuS/Al tunnel junction. We obtain diverse information from the comparison between theory and experiment. On the one hand, we can determine the values for the induced spin-splitting fields, spin-filter efficiency, magnetic disorder, spin-orbit coupling, and orbital effects in the superconductors. On the other hand, from the magnetic field dependence of the dI/dV curves, we can extract information about the magnetic structure of the two EuS layers, which turns out to be very different due to the rather different growth morphology of each layer.

In Sec. 4.3, we show that superconductors with a spin-split density of states (SS) together with ferromagnetic insulators (FI) may improve the refrigeration of a metallic (N) island at low voltages. SS-FI-N junctions also open the possibility to refrigerate the superconductor. Moreover, if the N is substituted by another superconductor S' with a gap smaller than the SS gap, the refrigeration of S' can be highly enhanced. These results can be applied to improve current on-chip cooling of metallic components and may lead to many practical applications where the refrigeration of superconductors is demanded. For experimental realization of these coolers, the most suitable material combination is Al in the superconducting regions and europium chalcogenides (such as EuS or EuO) as ferromagnetic insulators. The normal metal may be Cu. Because of the small spin-orbit interaction, thin Al shows very sharp spin-split density of states when placed in contact with the FI, whereas these europium chalcogenides can also been used as very efficient spin-filtering barriers.

In Sec. 4.4, we show that a superconducting wire on top of a F layer with Rashba SOC at the bottom interface can be used as a Josephson phase battery. In such a device, the geometry of the S layer of crucial importance to obtain a sizable φ_0 effect. For typical experimental values of interfacial SOC, one of these devices where both the S and F layers are present all along the wire would require of lengths much longer than the superconducting coherence length to accumulate a non-negligible phase. This situation changes when the superconducting layers gets interrupted along a distance L. In particular, we calculate the phase difference between two S islands of width W on top of the infinite F wire and separated by a distance L. We show that the value of φ_0 increases with increasing values of W, L and the exchange field in the F layer, h. The possibility to control the value of φ_0 with h is of special interest for potential applications. For $h \neq 0$ we find that φ_0 is finite even for $L \longrightarrow 0$. This let us predict some preliminary results on the phase accumulated along a wire of length L_{wire} where $N_{islands}$ of these S islands are placed on top of the F wire, and find an optimal value of $N_{islands}$ for which the accumulated phase is maximum. This results have been predicted assuming that the accumulated phase between every two consecutive S islands is independent and equal to the value of φ_0 that we obtained before for the situation where the two islands are isolated. Further research should be made on the effect that the presence of more S islands around has on the value of the phase accumulated between two S islands, and on the study of infinite S islands at the ends in order to provide an area to connect the phase battery to the circuit.

Appendix A

Quasiclassical GF in junctions between antiferromagnetic ACs

We consider a junction between two antiferromagnetic ACs, where the separation between impurities, a, remains constant, but their strength changes from one chain to the other one (Φ_L and Φ_R in the left and right AC, respectively). Both chains meet at $x = 0$. The *chain propagator* of each chain is given by Eq. (3.59), substituting Φ by Φ_L and Φ_R in the left and right AC, respectively. The set of eigenvalues and left- and right-eigenvectors of the chain propagator of the AC in the left (right) part of the junction that fulfill,

$$\hat{S}_{L(R)\sigma}\,|\lambda^{\pm}_{L(R)\sigma}\rangle = e^{\pm\lambda_{L(R)\sigma}}\,|\lambda^{\pm}_{L(R)\sigma}\rangle\,, \tag{A.1}$$

$$\langle\tilde{\lambda}^{\pm}_{L(R)\sigma}|\,\hat{S}_{L(R)\sigma} = e^{\pm\lambda_{L(R)\sigma}}\,\langle\tilde{\lambda}^{\pm}_{L(R)\sigma}|\,, \tag{A.2}$$

respectively, read,

$$\begin{aligned} e^{\pm\lambda_{L(R)\sigma}} = {}& 1 + 2\,\langle\tilde{+}|e^{i\sigma\hat{\tau}_3\Phi_{L(R)}}|+\rangle\,\langle\tilde{-}|e^{i\sigma\hat{\tau}_3\Phi_{L(R)}}|-\rangle\sinh^2\frac{a}{\xi} \pm 2\Bigg[\,\langle\tilde{+}|e^{i\sigma\hat{\tau}_3\Phi_{L(R)}}|+\rangle \\ & \times\langle\tilde{-}|e^{i\sigma\hat{\tau}_3\Phi_{L(R)}}|-\rangle\sinh^2\frac{a}{\xi} + \left(\,\langle\tilde{+}|e^{i\sigma\hat{\tau}_3\Phi_{L(R)}}|+\rangle\,\langle\tilde{-}|e^{i\sigma\hat{\tau}_3\Phi_{L(R)}}|-\rangle\sinh^2\frac{a}{\xi}\right)^2\Bigg]^{1/2}, \end{aligned} \tag{A.3}$$

and,

$$\langle\tilde{\lambda}^{\pm}_{L(R)\sigma}| = c^{\pm}_{L(R)\sigma}\begin{pmatrix} \tilde{d}^{\pm}_{L(R)\sigma} & 1 \end{pmatrix}, \tag{A.4}$$

$$|\lambda^{\pm}_{L(R)\sigma}\rangle = c^{\pm}_{L(R)\sigma}\begin{pmatrix} 1 \\ d^{\pm}_{L(R)\sigma} \end{pmatrix}, \tag{A.5}$$

where,

$$d^{\pm}_{L(R)\sigma} = \frac{e^{\pm\lambda_{L(R)\sigma}} - 1 - \left(e^{\frac{2a}{\xi}} - 1\right)\langle\tilde{+}|e^{i\sigma\hat{\tau}_3\Phi_{L(R)}}|+\rangle\langle\tilde{-}|e^{i\sigma\hat{\tau}_3\Phi_{L(R)}}|-\rangle}{(e^{\frac{2a}{\xi}} - 1)\langle\tilde{-}|e^{i\sigma\hat{\tau}_3\Phi_{L(R)}}|-\rangle\langle\tilde{+}|e^{i\sigma\hat{\tau}_3\Phi_{L(R)}}|-\rangle}, \tag{A.6}$$

$$\tilde{d}^{\pm}_{L(R)\sigma} = \frac{e^{\pm\lambda_{L(R)\sigma}} - 1 + \left(1 - e^{-\frac{2a}{\xi}}\right)\langle\tilde{+}|e^{i\sigma\hat{\tau}_3\Phi_{L(R)}}|+\rangle\langle\tilde{-}|e^{i\sigma\hat{\tau}_3\Phi_{L(R)}}|-\rangle}{(e^{\frac{2a}{\xi}} - 1)\langle\tilde{-}|e^{i\sigma\hat{\tau}_3\Phi_{L(R)}}|-\rangle\langle\tilde{+}|e^{i\sigma\hat{\tau}_3\Phi_{L(R)}}|-\rangle}, \tag{A.7}$$

$$c^{\pm}_{L(R)\sigma} = \sqrt{\pm\frac{\left(e^{\frac{2a}{\xi}} - 1\right)\langle\tilde{-}|e^{i\sigma\hat{\tau}_3\Phi_{L(R)}}|-\rangle\langle\tilde{+}|e^{i\sigma\hat{\tau}_3\Phi_{L(R)}}|-\rangle}{2\sinh\lambda_{L(R)\sigma}}}. \tag{A.8}$$

Here $\xi = \frac{\hbar v_F}{\sqrt{\Delta^2-\epsilon^2}}$ is the energy-dependent decay length and one should note that $\tilde{d}^{\pm}_{L(R)\sigma} = d^{\mp}_{L(R)\sigma}$. We can parametrize the value of the quasiclassical GF at the equivalent points of the chain in terms of the eigenvectors of the *chain propagator*, Eq. (A.5), as follows:

$$\begin{aligned}\hat{g}_\sigma(X^L_{2m}) =& \sqrt{1 - v_{s\sigma}w_{s\sigma}}\Big(|\lambda^{+}_{s\sigma}\rangle\langle\tilde{\lambda}^{+}_{s\sigma}| - |\lambda^{-}_{s\sigma}\rangle\langle\tilde{\lambda}^{-}_{s\sigma}|\Big) \\ &+ v_{s\sigma}e^{2\lambda_{s\sigma}m}|\lambda^{+}_{s\sigma}\rangle\langle\tilde{\lambda}^{-}_{s\sigma}| + w_{s\sigma}e^{-2\lambda_{s\sigma}m}|\lambda^{-}_{s\sigma}\rangle\langle\tilde{\lambda}^{+}_{s\sigma}|.\end{aligned} \tag{A.9}$$

Here, m is the unit cell index, X^L_{2m} stands for the left interface of the magnetic impurity located at $X_{2m} = 2ma$ and the sub-index s label the left (L) and right (R) crystal. The unit cells forming the left and right AC are those labeled by $n \leq 0$ and $m > 0$, respectively.

For energies at which $|e^{\pm\lambda_{L(R)\sigma}}| = 1$, Eq. (A.9) describes modes that propagate all along the structure. Otherwise, it describes exponentially decaying states by setting either $v_{L(R)\sigma}$ or $w_{L(R)\sigma}$ to zero to ensure commensurability of $\hat{g}_\sigma$ at the infinities. Which one is set to zero depends on whether $|e^{\pm\lambda_{L(R)\sigma}}| > 1$ or $|e^{\pm\lambda_{L(R)\sigma}}| < 1$. Indeed, numerical analysis of Eq. (A.3) shows that $|e^{\pm\lambda_{L(R)\sigma}}| \leq 1$ and, therefore, we can set $v_{L\sigma} = 0$ and $w_{R\sigma} = 0$. To obtain the remaining two parameters we require continuity of Eq. (A.9) across the junction, which yields

$$w_{L\sigma} = 2i\frac{d^{+}_{R\sigma} - d^{+}_{L\sigma}}{d^{+}_{R\sigma} - d^{-}_{L\sigma}}, \qquad v_{R\sigma} = 2i\frac{d^{-}_{R\sigma} - d^{-}_{L\sigma}}{d^{+}_{R\sigma} - d^{-}_{L\sigma}}. \tag{A.10}$$

Here $d^{\pm}_{L(R)\sigma}$ is given by Eq. (A.6).

Substituting Eq. (A.10) into Eq. (A.9) we get the value of the quasiclassical GF at the left interface of every second magnetic impurity, X^L_{2n}. To obtain $\hat{g}_\sigma(x)$ at every point inside the unit cell, hence, we have to propagate it from X^L_{2n} to x by means of the BCS propagator, Eq. (3.37), when the propagation is across the superconducting regions, and the propagation-like boundary conditions, Eq. (3.40), to connect the GFs at the left and right interfaces of each impurity. Such a propagation allows us writing the quasiclassical GF all along the space as follows:

$$\hat{g}_\sigma(x) = \begin{cases} \mathcal{B}^0_{m\sigma}\Big(|-\rangle\langle\tilde{-}| - |+\rangle\langle\tilde{+}| \Big) + \mathcal{B}^{+-}_{m\sigma} e^{2\frac{x-X_{2m-1}}{\xi}} |+\rangle\langle\tilde{-}| + \mathcal{B}^{-+}_{m\sigma} e^{-2\frac{x-X_{2m-1}}{\xi}} |-\rangle\langle\tilde{+}| \\ \hfill \text{if } X_{2n-2} < x < X_{2n-1}, \\ \\ \mathcal{A}^0_{m\sigma}\Big(|-\rangle\langle\tilde{-}| - |+\rangle\langle\tilde{+}| \Big) + \mathcal{A}^{+-}_{m\sigma} e^{2\frac{x-X_{2m}}{\xi}} |+\rangle\langle\tilde{-}| + \mathcal{A}^{-+}_{m\sigma} e^{-2\frac{x-X_{2m}}{\xi}} |-\rangle\langle\tilde{+}| \\ \hfill \text{if } X_{2n-1} < x < X_{2n}, \end{cases} \tag{A.11}$$

where $|\pm\rangle$ and $\langle\tilde{\pm}|$ are the right- and left-eigenvectors of the BCS propagator given by Eqs. (3.32) and (3.39), respectively. The expressions of the remaining constants depend on the side of the juction. The $\mathcal{A}$ constants in the AC on the left ($m \leq 0$) read:

$$\mathcal{A}^0_{m\sigma} = (c^+_{L\sigma})^2 \left[d^+_{L\sigma} + d^-_{L\sigma} + i w_{L\sigma} e^{-2\lambda_{L\sigma} m} d^-_{L\sigma} \right], \tag{A.12}$$

$$\mathcal{A}^{+-}_{m\sigma} = (c^+_{L\sigma})^2 \left[2 + i w_{L\sigma} e^{-2\lambda_{L\sigma} n} \right], \tag{A.13}$$

$$\mathcal{A}^{-+}_{m\sigma} = -(c^+_{L\sigma})^2 d^-_{L\sigma} \left[2 d^+_{L\sigma} + i w_{L\sigma} e^{-2\lambda_{L\sigma} m} d^-_{L\sigma} \right], \tag{A.14}$$

whereas in the right chain ($m > 0$) they read:

$$\mathcal{A}^0_{m\sigma} = (c^+_{R\sigma})^2 \left[d^+_{R\sigma} + d^-_{R\sigma} + i v_{R\sigma} e^{2\lambda_{R\sigma} m} d^+_{R\sigma} \right], \tag{A.15}$$

$$\mathcal{A}^{+-}_{m\sigma} = (c^+_{R\sigma})^2 \left[2 + i v_{R\sigma} e^{2\lambda_{R\sigma} n} \right], \tag{A.16}$$

$$\mathcal{A}^{-+}_{m\sigma} = -(c^+_{R\sigma})^2 d^+_{R\sigma} \left[2 d^-_{R\sigma} + i v_{R\sigma} e^{2\lambda_{R\sigma} m} d^+_{R\sigma} \right]. \tag{A.17}$$

The remaining expressions for the $\mathcal{B}$-s are given in terms of the $\mathcal{A}$-s shown in

Eqs. (A.12)–(A.17) and read

$$\begin{aligned}\mathcal{B}^{0}_{m\sigma} &= \Big(1 + 2\,\langle\tilde{+}|e^{i\sigma\hat{\tau}_3\Phi_s}|-\rangle\Big)\mathcal{A}^{0}_{m\sigma} + e^{-\frac{2a}{\xi}}\,\langle\tilde{+}|e^{i\sigma\hat{\tau}_3\Phi_s}|+\rangle\langle\tilde{+}|e^{i\sigma\hat{\tau}_3\Phi_s}|-\rangle\,\mathcal{A}^{+-}_{m\sigma} \\ &\quad - e^{\frac{2a}{\xi}}\,\langle\tilde{-}|e^{i\sigma\hat{\tau}_3\Phi_s}|-\rangle\langle\tilde{+}|e^{i\sigma\hat{\tau}_3\Phi_s}|-\rangle\,\mathcal{A}^{-+}_{m\sigma},\end{aligned} \tag{A.18}$$

$$\begin{aligned}\mathcal{B}^{+-}_{m\sigma} &= 2\,\langle\tilde{+}|e^{i\sigma\hat{\tau}_3\Phi_s}|+\rangle\langle\tilde{+}|e^{i\sigma\hat{\tau}_3\Phi_s}|-\rangle\,\mathcal{A}^{0}_{m\sigma} + e^{-\frac{2a}{\xi}}\,\langle\tilde{+}|e^{i\sigma\hat{\tau}_3\Phi_s}|+\rangle^2\,\mathcal{A}^{+-}_{m\sigma} \\ &\quad - e^{\frac{2a}{\xi}}\,\langle\tilde{+}|e^{i\sigma\hat{\tau}_3\Phi_s}|-\rangle^2\,\mathcal{A}^{-+}_{m\sigma},\end{aligned} \tag{A.19}$$

$$\begin{aligned}\mathcal{B}^{-+}_{m\sigma} &= -2\,\langle\tilde{-}|e^{i\sigma\hat{\tau}_3\Phi_s}|-\rangle\langle\tilde{+}|e^{i\sigma\hat{\tau}_3\Phi_s}|-\rangle\,\mathcal{A}^{0}_{m\sigma} - e^{-\frac{2a}{\xi}}\,\langle\tilde{+}|e^{i\sigma\hat{\tau}_3\Phi_s}|-\rangle^2\,\mathcal{A}^{+-}_{m\sigma} \\ &\quad + e^{\frac{2a}{\xi}}\,\langle\tilde{-}|e^{i\sigma\hat{\tau}_3\Phi_s}|-\rangle^2\,\mathcal{A}^{-+}_{m\sigma},\end{aligned} \tag{A.20}$$

where $\Phi_s = \Phi_L$ when $m \leq 0$ (*i.e.*, in the left side of the junction) and $\Phi_s = \Phi_R$ otherwise. Equations (A.11)–(A.20) provide the quasiclassical GF for the σ spin component of a junction between two antiferromagnetic ACs at any position, x, from which we can directly calculate observables like the local density of states, Eq. (3.42), or the local spin density, Eq. (3.43).

Bibliography

[1] H. K. Onnes, Further experiments with liquid helium. g. on the electrical resistance of pure metals, etc. vi. on the sudden change in the rate at which the resistance of mercury disappears., in *KNAW, Proceedings*, volume 14, pages 818–821, Royal Netherlands Academy of Arts and Sciences (KNAW), 1912.

[2] W. Meissner and R. Ochsenfeld, Die Naturwissenschaften **21**, 787 (1933).

[3] F. London and H. London, Proceedings of the Royal Society of London. Series A-Mathematical and Physical Sciences **149**, 71 (1935).

[4] V. L. Ginzburg and L. D. Landau, Zh. Eksp. Teor. Fiz. **20**, 1064 (1950).

[5] J. Bardeen, L. N. Cooper, and J. R. Schrieffer, Phys. Rev. **108**, 1175 (1957).

[6] L. N. Cooper, Physical Review **104**, 1189–1190 (1956).

[7] E. Maxwell, Phys. Rev. **78**, 477 (1950).

[8] C. A. Reynolds, B. Serin, W. H. Wright, and L. B. Nesbitt, Phys. Rev. **78**, 487 (1950).

[9] H. Fröhlich, Phys. Rev. **79**, 845 (1950).

[10] J. Bardeen, Phys. Rev. **80**, 567 (1950).

[11] J. Bardeen, Phys. Rev. **79**, 167 (1950).

[12] J. Bardeen, Phys. Rev. **82**, 978 (1951).

[13] J. Bardeen, Phys. Rev. **81**, 1070 (1951).

[14] J. Bardeen, Phys. Rev. **81**, 829 (1951).

[15] C. Kittel, *Introduction to Solid State Physics*, Wiley, Hoboken, NJ, 8 edition, 2004.

[16] J. Nagamatsu, N. Nakagawa, T. Muranaka, Y. Zenitani, and J. Akimitsu, Nature **410**, 63 (2001).

[17] R. C. Jaklevic, J. Lambe, A. H. Silver, and J. E. Mercereau, Physical Review Letters **12**, 159 (1964).

[18] G. S. Paraoanu, Journal of Low Temperature Physics **175**, 633 (2014).

[19] J. Q. You and F. Nori, Nature **474**, 589 (2011).

[20] G. Wendin, Reports on Progress in Physics **80**, 106001 (2017).

[21] V. Bouchiat, D. Vion, P. Joyez, D. Esteve, and M. H. Devoret, Physica Scripta **T76**, 165 (1998).

[22] D. Vion et al., Superconducting quantum bit based on the cooper pair box, in *New Directions in Mesoscopic Physics (Towards Nanoscience)*, edited by R. Fazio, V. F. Gantmakher, and Y. Imry, pages 173–195, Dordrecht, 2003, Springer Netherlands.

[23] J. Koch et al., Phys. Rev. A **76**, 042319 (2007).

[24] V. E. Manucharyan, J. Koch, L. I. Glazman, and M. H. Devoret, Science **326**, 113 (2009).

[25] K. D. Irwin, Applied Physics Letters **66**, 1998 (1995).

[26] K. D. Irwin, Scientific American **295**, 86 (2006).

[27] B. S. Karasik and R. Cantor, Applied Physics Letters **98**, 193503 (2011).

[28] A. Monfardini et al., Lumped element kinetic inductance detectors for space applications, in *Millimeter, Submillimeter, and Far-Infrared Detectors and Instrumentation for Astronomy VIII*, edited by W. S. Holland and J. Zmuidzinas, SPIE, 2016.

[29] A. I. Buzdin, Reviews of modern physics **77**, 935 (2005).

[30] F. Bergeret, A. F. Volkov, and K. B. Efetov, Reviews of modern physics **77**, 1321 (2005).

[31] F. S. Bergeret, M. Silaev, P. Virtanen, and T. T. Heikkilä, Rev. Mod. Phys. **90**, 041001 (2018).

[32] T. T. Heikkilä, M. Silaev, P. Virtanen, and F. S. Bergeret, Progress in Surface Science **94**, 100540 (2019).

[33] M. Eschrig, Reports on Progress in Physics **78**, 104501 (2015).

[34] B. Josephson, Physics Letters **1**, 251 (1962).

[35] P. W. Anderson and J. M. Rowell, Phys. Rev. Lett. **10**, 230 (1963).

[36] S. Shapiro, Phys. Rev. Lett. **11**, 80 (1963).

[37] T. Tokuyasu, J. A. Sauls, and D. Rainer, Phys. Rev. B **38**, 8823 (1988).

[38] P. M. Tedrow, J. E. Tkaczyk, and A. Kumar, Phys. Rev. Lett. **56**, 1746 (1986).

[39] X. Hao, J. S. Moodera, and R. Meservey, Phys. Rev. B **42**, 8235 (1990).

[40] R. Meservey and P. Tedrow, Physics Reports **238**, 173 (1994).

[41] R. Meservey, P. M. Tedrow, and P. Fulde, Phys. Rev. Lett. **25**, 1270 (1970).

[42] R. Meservey, P. M. Tedrow, and R. C. Bruno, Phys. Rev. B **11**, 4224 (1975).

[43] M. Tinkham, *Introduction to Superconductivity*, Dover Publications, Mineola, New York, 2 edition, 2004.

[44] P. M. Tedrow and R. Meservey, Phys. Rev. B **7**, 318 (1973).

[45] D. Paraskevopoulos, R. Meservey, and P. M. Tedrow, Phys. Rev. B **16**, 4907 (1977).

[46] R. Meservey, D. Paraskevopoulos, and P. M. Tedrow, Phys. Rev. B **22**, 1331 (1980).

[47] F. Hübler, M. J. Wolf, D. Beckmann, and H. v. Löhneysen, Phys. Rev. Lett. **109**, 207001 (2012).

[48] P. Machon, M. Eschrig, and W. Belzig, Phys. Rev. Lett. **110**, 047002 (2013).

[49] F. Giazotto, T. T. Heikkilä, and F. S. Bergeret, Phys. Rev. Lett. **114**, 067001 (2015).

[50] F. Giazotto, P. Solinas, A. Braggio, and F. S. Bergeret, Phys. Rev. Applied **4**, 044016 (2015).

[51] D. Beckmann, J. Phys.: Condens. Matter **28**, 163001 (2016).

[52] T. T. Heikkilä et al., Physical Review Applied **10**, 034053 (2018).

[53] G. De Simoni, E. Strambini, J. S. Moodera, F. S. Bergeret, and F. Giazotto, Nano letters **18**, 6369 (2018).

[54] A. Ozaeta, P. Virtanen, F. S. Bergeret, and T. T. Heikkilä, Phys. Rev. Lett. **112**, 057001 (2014).

[55] F. Giazotto and F. S. Bergeret, Appl. Phys. Lett. **102**, 132603 (2013).

[56] F. Giazotto, J. W. A. Robinson, J. S. Moodera, and F. S. Bergeret, Appl. Phys. Lett. **105**, 062602 (2014).

[57] M. Rouco, T. T. Heikkilä, and F. S. Bergeret, Phys. Rev. B **97**, 014529 (2018).

[58] S. Chakraborty and T. T. Heikkilä, J. Appl. Phys. **124**, 123902 (2018).

[59] E. I. Rashba, Sov. Phys., Solid State **2**, 1109 (1960).

[60] Y. A. Bychkov and E. I. Rashba, Pis'ma Zh. Eksp. Teor. Fiz. **39**, 66 (1984), [JETP Lett. **39**, 78 (1984)].

[61] F. S. Bergeret and I. V. Tokatly, Phys. Rev. B **89**, 134517 (2014).

[62] F. Konschelle, I. V. Tokatly, and F. S. Bergeret, Physical Review B **92**, 125443 (2015).

[63] F. Bergeret and I. Tokatly, Europhys. Letters **110**, 57005 (2015).

[64] I. V. Tokatly, Physical Review B **96**, 060502(R) (2017).

[65] D. V. Gruznev et al., Scientific Reports **4**, 4742 (2014).

[66] T. Sekihara, R. Masutomi, and T. Okamoto, Phys. Rev. Lett. **111**, 057005 (2013).

[67] G. C. Ménard et al., Nature Communications **8**, 2040 (2017).

[68] D. F. Agterberg and R. P. Kaur, Phys. Rev. B **75**, 064511 (2007).

[69] O. Dimitrova and M. V. Feigel'man, Phys. Rev. B **76**, 014522 (2007).

[70] V. M. Edelstein, Phys. Rev. Lett. **75**, 2004 (1995).

[71] S. K. Yip, Phys. Rev. B **65**, 144508 (2002).

[72] J. Sinova, S. O. Valenzuela, J. Wunderlich, C. H. Back, and T. Jungwirth, Rev. Mod. Phys. **87**, 1213 (2015).

[73] E. G. Mishchenko, A. V. Shytov, and B. I. Halperin, Phys. Rev. Lett. **93**, 226602 (2004).

[74] A. G. Aronov and Y. B. Lyanda-Geller, Pis'ma Zh. Eksp. Teor. Fiz. **50**, 398 (1989), [JETP Lett. **50**, 431 (1989)].

[75] V. Edelstein, Solid State Communications **73**, 233 (1990).

[76] E. L. Ivchenko, Y. B. Lyanda-Geller, and G. E. Pikus, Pis'ma Zh. Eksp. Teor. Fiz. **50**, 156 (1989), [JETP Lett. **50**, 175 (1989)].

[77] E. L. Ivchenko, Y. B. Lyanda-Geller, and G. E. Pikus, Zh. Eksp. Teor. Fiz. **98**, 989 (1990), [Sov. Phys. JETP **71**, 550 (1990)].

[78] L. P. Gor'kov and E. I. Rashba, Phys. Rev. Lett. **87**, 037004 (2001).

[79] M. Sato, Y. Takahashi, and S. Fujimoto, Physical Review Letters **103**, 020401 (2009).

[80] J. D. Sau, R. M. Lutchyn, S. Tewari, and S. D. Sarma, Physical Review Letters **104**, 040502 (2010).

[81] R. M. Lutchyn, J. D. Sau, and S. D. Sarma, Physical Review Letters **105**, 077001 (2010).

[82] J. Alicea, Physical Review B **81**, 125318 (2010).

[83] Y. Oreg, G. Refael, and F. von Oppen, Physical Review Letters **105**, 177002 (2010).

[84] F. S. Bergeret and I. V. Tokatly, Physical Review B **102**, 060506(R) (2020).

[85] C. Sanz-Fernández et al., Applied Physics Letters **117**, 142405 (2020).

[86] E. Strambini et al., Nature Nanotechnology **15**, 656 (2020).

[87] S. Pal and C. Benjamin, EPL (Europhysics Letters) **126**, 57002 (2019).

[88] A. F. Andreev, Zh. Eksp. Teor. Fiz. **46**, 1823 (1964), [Sov. Phys. JETP **19**, 1228 (1964)].

[89] A. F. Andreev, Zh. Eksp. Teor. Fiz. **49**, 655 (1965), [Sov. Phys. JETP **22**, 455 (1966)].

[90] L. Yu, Acta Phys. Sin **21**, 75 (1965).

[91] H. Shiba, Progress of theoretical Physics **40**, 435 (1968).

[92] A. Rusinov, Zh. Eksp. Teor. Fiz. Pisma Red. **9**, 146 (1968), [Sov. Phys. JETP **9**, 85 (1969)].

[93] A. Costa, J. Fabian, and D. Kochan, Phys. Rev. B **98**, 134511 (2018).

[94] M. Rouco, I. V. Tokatly, and F. S. Bergeret, Phys. Rev. B **99**, 094514 (2019).

[95] A. Sakurai, Progress of Theoretical Physics **44**, 1472 (1970).

[96] A. V. Balatsky, I. Vekhter, and J.-X. Zhu, Rev. Mod. Phys. **78**, 373 (2006).

[97] L. N. Bulaevskii, V. V. Kuzii, and A. A. Sobyanin, Pis'ma Zh. Eksp. Teor. Fiz. **25**, 314 (1977), [JETP Lett. **25**, 290 (1977)].

[98] A. I. Buzdin, L. N. Bulaevskii, and S. V. Panyukov, Pis'ma Zh. Eksp. Teor. Fiz. **35**, 147 (1982), [JETP Lett. **35**, 178 (1982)].

[99] L. Lazar et al., Physical Review B **61**, 3711 (2000).

[100] V. V. Ryazanov et al., Physical review letters **86**, 2427 (2001).

[101] N. M. Chtchelkatchev, W. Belzig, Y. V. Nazarov, and C. Bruder, Journal of Experimental and Theoretical Physics Letters **74**, 323 (2001), [Pis'ma v Zh. Eksp. i Teor. Fiz. **74**, 357 (2001)].

[102] S. Nadj-Perge, I. K. Drozdov, B. A. Bernevig, and A. Yazdani, Phys. Rev. B **88**, 020407(R) (2013).

[103] F. Pientka, L. I. Glazman, and F. von Oppen, Phys. Rev. B **88**, 155420 (2013).

[104] A. Heimes, P. Kotetes, and G. Schön, Physical Review B **90**, 060507(R) (2014).

[105] K. Pöyhönen, A. Westström, J. Röntynen, and T. Ojanen, Physical Review B **89**, 115109 (2014).

[106] A. Westström, K. Pöyhönen, and T. Ojanen, Physical Review B **91**, 064502 (2015).

[107] F. Pientka, Y. Peng, L. Glazman, and F. v. Oppen, Physica Scripta **T164**, 014008 (2015).

[108] P. M. R. Brydon, S. Das Sarma, H.-Y. Hui, and J. D. Sau, Physical Review B **91**, 064505 (2015).

[109] M. Schecter, K. Flensberg, M. H. Christensen, B. M. Andersen, and J. Paaske, Phys. Rev. B **93**, 140503(R) (2016).

[110] S. Hoffman, J. Klinovaja, and D. Loss, Phys. Rev. B **93**, 165418 (2016).

[111] M. Rouco, F. S. Bergeret, and I. V. Tokatly, Physical Review B **103**, 064505 (2021).

[112] M. Rouco, F. S. Bergeret, and I. V. Tokatly, Phys. Rev. B **104**, 064506 (2021).

[113] P. W. Anderson, Journal of Physics and Chemistry of Solids **11**, 26 (1959).

[114] F. S. Bergeret and I. V. Tokatly, Physical Review B **94**, 180502 (2016).

[115] N. N. Bogoliubov, V. V. Tolmachov, and D. V. Širkov, Zh. Eksp. Teor. Fiz. **34**, 58 (1958), [Sov. Phys. JETP **34**, 58–79 (1958)].

[116] A. L. Fetter and J. D. Walecka, *Quantum Theory of Many-Particle Systems*, Dover Books on Physics, Dover Publications, Mineola, New York, 2003.

[117] A. A. Abrikosov, *Fundamentals of the Theory of Metals*, Dover Publications, New York, 2017.

[118] P. G. de Gennes, *Superconductivity of Metals and Alloys*, Benjamin, New York, 1966.

[119] N. B. Kopnin, *Theory of Nonequilibrium Superconductivity (International Series of Monographs on Physics)*, International Series of Monographs on Physics, Oxford University Press, New York, 2001.

[120] N. B. Kopnin, Theory of superconductivity, 2006, [Lecture notes available online at http://ltl.tkk.fi/opetus/supertheory/tfy-3.491/TheorySC06.pdf].

[121] L. V. Keldysh, Zh. Eksp. Teor. Fiz. **47**, 1515 (1964), [Sov. Phys. JETP **20**, 1018 (1965)].

[122] D. N. Langenberg and A. I. Larkin, *Nonequilibrium superconductivity*, North-Holland, Amsterdam, 1986.

[123] J. Rammer and H. Smith, Rev. Mod. Phys. **58**, 323 (1986).

[124] A. Larkin and Y. Ovchinnikov, Zh. Eksp. Teor. Fiz. **68**, 1915 (1975), [Sov. Phys. JETP **41**, 469 (1945)].

[125] A. I. Larkin and Y. N. Ovchinnikov, Zh. Eksp. Teor. Fiz. **55**, 2262 (1968), [Sov. Phys. JETP **28** 1200 (1969)].

[126] W. Belzig, F. K. Wilhelm, C. Bruder, G. Schön, and A. D. Zaikin, Superlattices and Microstructures **25**, 1251 (1999).

[127] J. E. Moyal, Mathematical Proceedings of the Cambridge Philosophical Society **45**, 99–124 (1949).

[128] G. Eilenberger, Zeitschrift für Physik A Hadrons and nuclei **214**, 195 (1968).

[129] V. L. Ginzburg, J. Exptl. Theoret. Phys. **31**, 202 (1956), [Sov. Phys. JETP **4**, 153 (1957)].

[130] W. Belzig, C. Bruder, and G. Schön, Phys. Rev. B **54**, 9443 (1996).

[131] A. Anthore, H. Pothier, and D. Esteve, Phys. Rev. Lett. **90**, 127001 (2003).

[132] K. D. Usadel, Phys. Rev. Lett. **25**, 507 (1970).

[133] A. Zaitsev, Zh. Eksp. Teor. Fiz **86**, 1742 (1984).

[134] A. Millis, D. Rainer, and J. A. Sauls, Phys. Rev. B **38**, 4504 (1988).

[135] M. Y. Kuprianov and V. Lukichev, Zh. Eksp. Teor. Fiz **94**, 139 (1988).

[136] A. Cottet, Phys. Rev. B **76**, 224505 (2007).

[137] A. Cottet, D. Huertas-Hernando, W. Belzig, and Y. V. Nazarov, Phys. Rev. B **80**, 184511 (2009).

[138] M. Eschrig, A. Cottet, W. Belzig, and J. Linder, New Journal of Physics **17**, 083037 (2015).

[139] F. S. Bergeret, A. Verso, and A. F. Volkov, Phys. Rev. B **86**, 060506(R) (2012).

[140] F. S. Bergeret, A. Verso, and A. F. Volkov, Phys. Rev. B **86**, 214516 (2012).

[141] T. Matsubara, Progress of Theoretical Physics **14**, 351 (1955).

[142] L. P. Kadanoff and G. Baym, *Quantum statistical mechanics; Green's function methods in equilibrium and nonequilibrium problems*, Frontiers in physics, New York, W.A. Benjamin, 1962.

[143] A. A. Abrikosov, L. P. Gor'kov, and I. E. Dzyaloshinski, *Quantum field theoretical methods in statistical physics*, Dover Books on Physics, Dover Publications, New York, revised edition, 1975.

[144] G. D. Mahan, *Many-particle physics*, Physics of solids and liquids, Kluwer Academic/Plenum Publishers, New York, 3rd ed edition, 2000.

[145] R. C. Dynes, V. Narayanamurti, and J. P. Garno, Phys. Rev. Lett. **41**, 1509 (1978).

[146] R. C. Dynes, J. P. Garno, G. B. Hertel, and T. P. Orlando, Phys. Rev. Lett. **53**, 2437 (1984).

[147] H. Monien, Mathematics of computation **79**, 857 (2010).

[148] M. A. Woolf and F. Reif, Physical Review **137**, A557 (1965).

[149] P. Fulde and K. Maki, Physical Review **141**, 275 (1966).

[150] A. Yazdani, Science **275**, 1767–1770 (1997).

[151] K. J. Franke, G. Schulze, and J. I. Pascual, Science **332**, 940–944 (2011).

[152] T. Meng, J. Klinovaja, S. Hoffman, P. Simon, and D. Loss, Phys. Rev. B **92**, 064503 (2015).

[153] B. W. Heinrich, J. I. Pascual, and K. J. Franke, Progress in Surface Science **93**, 1 (2018).

[154] L. Farinacci et al., Phys. Rev. Lett. **121**, 196803 (2018).

[155] A. Golubov, M. Kupriyanov, and E. Il'ichev, Reviews of Modern Physics **76**, 411 (2004).

[156] F. Konschelle, F. S. Bergeret, and I. V. Tokatly, Physical Review Letters **116**, 237002 (2016).

[157] F. Konschelle, I. V. Tokatly, and F. S. Bergeret, Physical Review B **94**, 014515 (2016).

[158] K. P. Duncan and B. L. Györffy, Annals of Physics **298**, 273 (2002).

[159] D. Beckmann, H. B. Weber, and H. v. Löhneysen, Physical Review Letters **93**, 197003 (2004).

[160] T. S. Khaire, M. A. Khasawneh, W. Pratt Jr, and N. O. Birge, Physical review letters **104**, 137002 (2010).

[161] N. Banerjee et al., Nature communications **5**, 1 (2014).

[162] A. Singh, S. Voltan, K. Lahabi, and J. Aarts, Physical Review X **5**, 021019 (2015).

[163] J. Linder and J. W. Robinson, Nature Physics **11**, 307 (2015).

[164] S. V. Bakurskiy et al., JETP letters **102**, 586 (2015).

[165] M. F. Atiyah, V. K. Patodi, and I. M. Singer, Mathematical Proceedings of the Cambridge Philosophical Society **79**, 71 (1976).

[166] M. F. Atiyah, V. K. Patodi, and I. M. Singer, Mathematical Proceedings of the Cambridge Philosophical Society **78**, 405 (1975).

[167] M. F. Atiyah, V. K. Patodi, and I. M. Singer, Mathematical Proceedings of the Cambridge Philosophical Society **77**, 43–69 (1975).

[168] A. J. Niemi and G. W. Semenoff, Physical Review D **30**, 809 (1984).

[169] R. Blankenbecler and D. Boyanovsky, Physical Review D **31**, 2089 (1985).

[170] A. A. Andrianov, V. A. Andrianov, V. Y. Novozhilov, and Y. V. Novozhilov, Letters in Mathematical Physics **11**, 217–224 (1986).

[171] M. Stone, Physical Review B **31**, 6112 (1985).

[172] G. E. Volovik, *The Universe in a Helium Droplet (The International Series of Monographs on Physics, 117)*, Oxford University Press, New York, 2003.

[173] K. Björnson, A. V. Balatsky, and A. M. Black-Schaffer, Phys. Rev. B **95**, 104521 (2017).

[174] C. W. J. Beenakker, Phys. Rev. Lett. **67**, 3836 (1991).

[175] S.-H. Ji et al., Physical review letters **100**, 226801 (2008).

[176] J.-D. Pillet et al., Nature Physics **6**, 965–969 (2010).

[177] M. Ruby et al., Phys. Rev. Lett. **115**, 087001 (2015).

[178] M. F. Goffman et al., Physical review letters **85**, 170 (2000).

[179] N. Agraıt, A. L. Yeyati, and J. M. Van Ruitenbeek, Physics Reports **377**, 81 (2003).

[180] A. V. Rozhkov and D. P. Arovas, Physical review letters **82**, 2788 (1999).

[181] E. Vecino, A. Martín-Rodero, and A. L. Yeyati, Physical Review B **68**, 035105 (2003).

[182] F. S. Bergeret, A. L. Yeyati, and A. Martín-Rodero, Physical Review B **74**, 132505 (2006).

[183] L. Gor'kov and V. Kresin, Applied Physics Letters **78**, 3657 (2001).

[184] B. M. Andersen and P. Hedegård, Physical Review B **66**, 104515 (2002).

[185] I. V. Bobkova, P. J. Hirschfeld, and Y. S. Barash, Physical Review Letters **94**, 037005 (2005).

[186] B. M. Andersen, I. V. Bobkova, P. J. Hirschfeld, and Y. S. Barash, Physical Review B **72**, 184510 (2005).

[187] R. Jackiw and C. Rebbi, Phys. Rev. D **13**, 3398 (1976).

[188] W. P. Su, J. R. Schrieffer, and A. J. Heeger, Physical Review B **22**, 2099 (1980).

[189] W. P. Su, J. R. Schrieffer, and A. J. Heeger, Physical Review Letters **42**, 1698 (1979).

[190] J. Goldstone and F. Wilczek, Physical Review Letters **47**, 986 (1981).

[191] R. MacKenzie and F. Wilczek, Physical Review D **30**, 2194 (1984).

[192] B. Volkov and O. Pankratov, JETP Lett **42**, 178 (1985).

[193] D. Vanderbilt, *Berry Phases in Electronic Structure Theory*, Cambridge University Press, Cambridge, 2018.

[194] N. Ashcroft and D. Mermin, *Solid state physics*, Cengage Learning, Andover (England), 1976.

[195] X. Zhang, V. Golovach, F. Giazotto, and F. Bergeret, Physical Review B **101**, 180502(R) (2020).

[196] P. M. Tedrow and R. Meservey, Phys. Rev. Lett. **26**, 192 (1971).

[197] J. S. Moodera, X. Hao, G. A. Gibson, and R. Meservey, Phys. Rev. Lett. **61**, 637 (1988).

[198] J. S. Moodera, T. S. Santos, and T. Nagahama, J. Phys.: Condens. Matter **19**, 165202 (2007).

[199] F. Hübler, J. C. Lemyre, D. Beckmann, and H. v. Löhneysen, Phys. Rev. B **81**, 184524 (2010).

[200] M. J. Wolf, C. Sürgers, G. Fischer, and D. Beckmann, Phys. Rev. B **90**, 144509 (2014).

[201] S. Kolenda, M. J. Wolf, and D. Beckmann, Phys. Rev. Lett. **116**, 097001 (2016).

[202] M. Silaev, P. Virtanen, F. S. Bergeret, and T. T. Heikkilä, Phys. Rev. Lett. **114**, 167002 (2015).

[203] A. Schmid and G. Schön, Journal of Low Temperature Physics **20**, 207 (1975).

[204] M. Nahum, T. M. Eiles, and J. M. Martinis, Appl. Phys. Lett. **65**, 3123 (1994).

[205] M. M. Leivo, J. P. Pekola, and D. V. Averin, Appl. Phys. Lett. **68**, 1996 (1996).

[206] J. P. Pekola et al., Phys. Rev. Lett. **92**, 056804 (2004).

[207] A. M. Clark et al., Appl. Phys. Lett. **86**, 173508 (2005).

[208] F. Giazotto, T. T. Heikkilä, A. Luukanen, A. M. Savin, and J. P. Pekola, Rev. Mod. Phys. **78**, 217 (2006).

[209] S. Rajauria et al., Phys. Rev. Lett. **99**, 047004 (2007).

[210] H. Q. Nguyen, M. Meschke, H. Courtois, and J. P. Pekola, Phys. Rev. Applied **2**, 054001 (2014).

[211] J. T. Muhonen, M. Meschke, and J. P. Pekola, Rep. Progr. Phys. **75**, 046501 (2012).

[212] H. Q. Nguyen, M. Meschke, and J. P. Pekola, Appl. Phys. Lett. **106**, 012601 (2015).

[213] A. Hijano et al., Phys. Rev. Research **3**, 023131 (2021).

[214] F. S. Bergeret, A. F. Volkov, and K. B. Efetov, Phys. Rev. Lett. **86**, 4096 (2001).

[215] M. Rouco et al., Phys. Rev. B **100**, 184501 (2019).

[216] E. Strambini et al., Physical Review Materials **1**, 054402 (2017).

[217] X.-P. Zhang, F. S. Bergeret, and V. N. Golovach, Nano Letters **19**, 6330–6337 (2019).

[218] G.-X. Miao and J. S. Moodera, Applied Physics Letters **94**, 182504 (2009).

[219] M. G. Khusainov, Zh. Eksp. Teor. Fiz. **109**, 524 (1996).

[220] Yu. A. Izyumov, Yu. N. Proshin, and M. G. Khusainov, Phys. Usp. **45**, 109 (2002).

[221] K. Maki, Prog. Theor. Phys. **31**, 731 (1964).

[222] R. E. Harris, Physical Review B **10**, 84 (1974).

[223] A. I. Larkin and Y. N. Ovchinnikov, Zh. Eksp. Teor. Fiz. **51**, 1535 (1966), [Sov. Phys. JETP **24** (5), 0.35 (1967)].

[224] A. Barone and G. Paterno, *Physics and applications of the Josephson effect*, Wiley, New York, 1982.

[225] A. Buzdin, Phys. Rev. Lett. **101**, 107005 (2008).

[226] A. Zazunov, R. Egger, T. Jonckheere, and T. Martin, Phys. Rev. Lett. **103**, 147004 (2009).

[227] A. Brunetti, A. Zazunov, A. Kundu, and R. Egger, Phys. Rev. B **88**, 144515 (2013).

[228] A. A. Reynoso, G. Usaj, C. A. Balseiro, D. Feinberg, and M. Avignon, Phys. Rev. Lett. **101**, 107001 (2008).

[229] K. N. Nesterov, M. Houzet, and J. S. Meyer, Phys. Rev. B **93**, 174502 (2016).

[230] I. V. Bobkova, A. M. Bobkov, A. A. Zyuzin, and M. Alidoust, Phys. Rev. B **94**, 134506 (2016).

[231] T. Yokoyama, M. Eto, and Y. V. Nazarov, Phys. Rev. B **89**, 195407 (2014).

[232] M. A. Silaev, Phys. Rev. B **96**, 064519 (2017).

[233] M. A. Silaev, I. V. Tokatly, and F. S. Bergeret, Phys. Rev. B **95**, 184508 (2017).

[234] J.-F. Liu and K. S. Chan, Phys. Rev. B **82**, 125305 (2010).

[235] A. G. Mal'shukov, S. Sadjina, and A. Brataas, Phys. Rev. B **81**, 060502(R) (2010).

[236] Y. Lu and T. T. Heikkilä, Phys. Rev. B **100**, 104514 (2019).

[237] I. Margaris, V. Paltoglou, and N. Flytzanis, Journal of Physics: Condensed Matter **22**, 445701 (2010).

[238] V. Braude and Y. V. Nazarov, Physical review letters **98**, 077003 (2007).

[239] A. Moor, A. F. Volkov, and K. B. Efetov, Phys. Rev. B **92**, 180506(R) (2015).

[240] R. Grein, M. Eschrig, G. Metalidis, and G. Schön, Phys. Rev. Lett. **102**, 227005 (2009).

[241] S. Mironov and A. Buzdin, Phys. Rev. B **92**, 184506 (2015).

[242] V. Ambegaokar and A. Baratoff, Phys. Rev. Lett. **10**, 486 (1963).

[243] P. Tischer, IEEE Trans. Magn. **9**, 9 (1973).

[244] F. Jedema, H. Heersche, A. Filip, J. Baselmans, and B. Van Wees, Nature **416**, 713 (2002).

[245] N. Poli et al., Phys. Rev. Lett. **100**, 136601 (2008).

[246] S. Kawabata, A. Ozaeta, A. S. Vasenko, F. W. Hekking, and F. Sebastián Bergeret, Appl. Phys. Lett. **103**, 032602 (2013).

[247] S. Kolenda, P. Machon, D. Beckmann, and W. Belzig, Beilstein J. Nanotech. **7**, 1579 (2016).

[248] X. Hao, J. S. Moodera, and R. Meservey, Phys. Rev. Lett. **67**, 1342 (1991).

[249] Y. M. Xiong, S. Stadler, P. W. Adams, and G. Catelani, Phys. Rev. Lett. **106**, 247001 (2011).

[250] S. Kolenda, C. Sürgers, G. Fischer, and D. Beckmann, Phys. Rev. B **95**, 224505 (2017).

[251] V. F. Maisi et al., Phys. Rev. Lett. **111**, 147001 (2013).

[252] A. V. Timofeev et al., Phys. Rev. Lett. **102**, 017003 (2009).

[253] F. C. Wellstood, C. Urbina, and J. Clarke, Phys. Rev. B **49**, 5942 (1994).

[254] A. Ozaeta, A. S. Vasenko, F. W. J. Hekking, and F. S. Bergeret, Phys. Rev. B **85**, 174518 (2012).

[255] T. S. Santos and J. S. Moodera, Phys. Rev. B **69**, 241203 (2004).

[256] B. Frank and W. Krech, Physics Letters A **235**, 281 (1997).

[257] K. Maki and A. Griffin, Phys. Rev. Lett. **15**, 921 (1965).

[258] F. Giazotto and M. J. Martínez-Pérez, Nature **492**, 401 (2012).

[259] F. S. Bergeret and F. Giazotto, Phys. Rev. B **88**, 014515 (2013).

[260] P. P. J. Haazen et al., Nature Materials **12**, 299 (2013).